



Wireless Communication for Custom Hearing Instruments

Kammersgaard, Nikolaj Peter Brunvoll

Publication date:
2018

Document Version
Publisher's PDF, also known as Version of record

[Link back to DTU Orbit](#)

Citation (APA):
Kammersgaard, N. P. B. (2018). Wireless Communication for Custom Hearing Instruments. Technical University of Denmark.

General rights

Copyright and moral rights for the publications made accessible in the public portal are retained by the authors and/or other copyright owners and it is a condition of accessing publications that users recognise and abide by the legal requirements associated with these rights.

- Users may download and print one copy of any publication from the public portal for the purpose of private study or research.
- You may not further distribute the material or use it for any profit-making activity or commercial gain
- You may freely distribute the URL identifying the publication in the public portal

If you believe that this document breaches copyright please contact us providing details, and we will remove access to the work immediately and investigate your claim.

WIRELESS COMMUNICATION FOR CUSTOM HEARING INSTRUMENTS

Ph.D. Thesis
Nikolaj Peter Brunvoll Kammersgaard
January 2018

The present work was carried out at DTU Elektro and GN Hearing A/S in partial fulfillment of the requirements for the Ph.D. degree from the Technical University of Denmark.

Supervisors:

Kaj Bjarne Jakobsen, Ph.D.
Electromagnetic Systems, DTU Elektro, Technical University of Denmark.

Jesper Thaysen, Ph.D.
GN Hearing A/S.

Søren Helstrup Kvist, Ph.D.
GN Hearing A/S.

I will not boast in anything,
No gifts, no power, no wisdom;
But I will boast in Jesus Christ,
His death and resurrection.
Why should I gain from His reward?
I cannot give an answer;
But this I know with all my heart -
His wounds have paid my ransom.

Stuart Townend

Abstract

Wireless communication for custom hearing instruments has been studied. The main focus has been propagation and antennas for ear-to-ear communication at 2.45 GHz. Custom hearing instruments are specially made for the individual user's ear canal. Thus the devices are placed in the ear at various depths and orientations.

A new geometrical theory of diffraction formulation for the on-body creeping-wave propagation has been developed. It is the first attempt of a general formulation for all opaque, convex, and lossy dielectric objects. The formulation has been validated against an eigenfunction solution on a cylindrical geometry. It is valid for geometries down to a size $\frac{\kappa}{\kappa^2 + \tau^2} > \lambda/2$ and up to a torsion limit of $\tau/\kappa < 2$ as long as the geometries are opaque and convex.

The ear-to-ear on-body channel between hearing instruments on opposite sides of the head has been characterized by a new ear-to-ear propagation model. The model is based on the new developed geometrical theory of diffraction formulation. It is the first to find the geodesic lines that connect the ears. The model shows a clear path behind the head and a clear path over the top of the head. In front of the head multiple geodesic paths exist. The main one is the one over the chin. For an omni-directional antenna, the front paths would provide the main contribution to the ear-to-ear path gain. The model has been validated against simulations. It has been shown that the model predicts the interference between the different paths correctly. This has been shown with frequency sweeps and by a rotation of the antenna in the ear.

Multiple new antenna designs has been presented. The antennas are the first in a realistic in-the-ear position to achieve a path gain better than -80 dB. The antennas are matched for the entire 2.45 GHz industrial, scientific, and medical band. The antenna designs confirmed that a polarization perpendicular to the surface of the head is best to optimize the radiation efficiency. For two similarly sized and placed antennas, the efficiency improved by 5 dB. The magnitude and phase of the radiation pattern can change the contributing geodesic paths and thus their interference. The effect from the radiation pattern is seen to be more than 10 dB for the ear-to-ear path gain. Rotation and change of the placement in depth is shown to have significant effect. The effect from rotation is not intuitively predicted, but can be more than 10 dB. If the device is moved further into the ear canal the radiation efficiency drops with one to two decibels per millimeter.

In summary, the work gives a theoretical explanation to the creeping waves observed as well as a propagation model to estimate and analyze the ear-to-ear path gain. Finally, suitable antenna designs with guidelines for future designs for custom hearing instruments are given.

Resumé

Trådløs kommunikation til brugertilpassede høreapparater er blevet undersøgt. Hovedfokus har været udbredelse af radiobølger og antenner til øre-til-øre kommunikation ved 2,45 GHz. Brugertilpassede høreapparater er special-lavet til den enkelte brugers ørekanal. Derfor er apparaterne placeret i øret i forskellig dybde og orientering.

En ny formulering af geometrisk diffraktionsteori til ”på-kroppen” udbredelse af krybende bølger er blevet foreslået. Dette er det første forsøg på en generel formulering til alle uigennemtrængelige, konvekse og tabsholdige dielektriske objekter. Formuleringen er blevet valideret gennem sammenligning med en egenfunktionsløsning på en cylindrisk geometri. Den er gyldig for geometrier ned til en størrelse på $\frac{\kappa}{\kappa^2 + \tau^2} > \lambda/2$ og op til en torsionsgrænse på $\tau/\kappa < 2$ sålænge geometrien er uigennemtrængelig og konveks.

Øre-til-øre ”på-kroppen” radiokanalen mellem høreapparaterne på hver sin side af hovedet er blevet karakteriseret gennem en ny øre-til-øre udbredelsesmodel. Modellen er baseret på den nyudviklede formulering af geometrisk diffraktionsteori. Det er den første til at finde de geodætiske linjer, der forbinder ørerne. Modellen viser en tydelig sti bagom hovedet og en tydelig sti over toppen over hovedet. Rundt om forsiden af hovedet er der flere geodætiske stier. Den dominerende går via hagen. For en rund-strålende antenne er stierne rundt om forsiden af hovedet de dominerende for øre-til-øre strækningstab. Modellen er blevet valideret gennem sammenligninger med simuleringer. Det er blevet vist, at modellen forudsiger interferensen mellem de forskellige stier korrekt. Det blev vist gennem frekvensgennemløb og rotation af antennen i øret.

Adskillige nye antennedesign er blevet præsenteret. Antennerne er de første, der med en realistisk i-øret position, opnår et strækningstab bedre end 80 dB. Antennerne er tilpasset i hele 2,45 GHz frekvensbåndet til industriel, videnskabelig og medicinsk brug. Antennedesignene bekræfter at en polarisering vinkelret på overfalden af hovedet er bedst for at optimere udstrålingseffektiviteten. For to antenner med samme størrelse og placering er effektiviteten således forbedret med 5 dB. Styrken og fasen af udstrålingsdiagrammet kan ændre de bidragende geodætiske stier og dermed deres interferens. Påvirkningen fra udstrålingsdiagrammet er observeret til at være mere end 10 dB for øre-til-øre strækningstab. Rotation og ændring af placeringsdybden har også en betydelig effekt. Påvirkningen fra rotation er ikke til at forudsige intuitivt, men kan være mere end 10 dB. Hvis et apparat rykkes dybere ind i ørekanalen falder udstrålingseffektivitet med en til to decibel per millimeter.

Sammenfattende bringer arbejdet en teoretisk forklaring af de krybende bølger samtidig med en udbredelsesmodel, der estimerer og analyserer øre-til-øre strækningstab. Slutteligt bringer arbejdet brugbare antennedesign med retningslinjer til fremtidige antennedesign til brugertilpassede høreapparater.

PREFACE

The work presented in this thesis has been carried out in the R&D Radio Systems Group at GN Hearing A/S (GN) and in the Electromagnetic Systems Group of the Department of Electrical Engineering, Technical University of Denmark (DTU). The study was initiated in October 2014 and ended December 2017. Four months leave from August to December 2016 was spent in the Antenna Design team at Apple Inc. in Cupertino, California. Although not officially part of the PhD, it served as the company equivalent to a university exchange. The study has been funded by GN and Innovation Fund Denmark (Innovationsfonden).

I want to sincerely thank my friends and colleagues of the Radio Systems Group at GN and the Electromagnetic Systems Group at DTU for their interest in my work. They have been ready to assist with help, feedback and good ideas at any time. A special thanks to Søren Helstrup Kvist. Although officially just a co-supervisor at GN, he has been my everyday main supervisor at the neighboring desk. Furthermore, his thesis has formed the foundation of all the work in this thesis. Thanks to my supervisor at GN, Jesper Thaysen, for clearing any organizational, administrative, and economical hinder on the way. Your input ensured a link to real-world problems experienced by the hearing instrument users. Finally, I am truly grateful for the best university supervisor a PhD-candidate could wish for. Kaj Bjarne Jakobsen's door is always open and when he is busy, he still finds time. With feedback on papers delivered faster than auto-reply, any conference deadline can be made. Thanks for your openness to talk about more than theoretical wave-theory!

Romans 11:36

Copenhagen, January 2018.

Nikolaj Peter Brunvoll Kammergaard.

LIST OF PUBLICATIONS

The following publications have been prepared during the study. The papers [P1–P10] are included at the end of the thesis, on pages 47–124.

- [P1] N. P. B. Kammersgaard, S. H. Kvist, J. Thaysen, and K. B. Jakobsen, “Ear-to-ear propagation model based on geometrical theory of diffraction”, *Submitted to IEEE Transactions on Antennas and Propagation*, Jan. 2018.
- [P2] —, “Geometrical theory of diffraction formulation for on body propagation”, *Submitted to IEEE Transactions on Antennas and Propagation*, Jan. 2018.
- [P3] —, “In-the-ear circular-shaped balanced inverted-a antenna for hearing instruments”, *IEEE Antennas and Wireless Propagation Letters*, vol. 15, pp. 1839–1843, 2016.
- [P4] N. P. I. Kammersgaard, S. H. Kvist, S. Özden, J. Thaysen, and K. B. Jakobsen, “Body-worn antennas for body-centric wireless communications”, in *Proceedings of 2014 Loughborough Antennas and Propagation Conference*, IEEE, 2014, pp. 2–6.
- [P5] N. P. B. Kammersgaard, S. H. Kvist, J. Thaysen, and K. B. Jakobsen, “Off-body transmission range improvement for hearing instruments by the use of ear-to-ear communication”, in *Proceedings of 2015 Loughborough Antennas & Propagation Conference*, IEEE, 2015.
- [P6] —, “Validity of PEC approximation for on-body propagation”, in *Proceedings of Eucap 2016*, EurAPP, 2016.
- [P7] —, “Electromagnetic fields at the surface of human-body cylinders”, in *Proceedings of the 2016 International Workshop on Antenna Technology*, IEEE, 2016, pp. 170–173.
- [P8] N. P. I. Kammersgaard, S. H. Kvist, J. Thaysen, and K. B. Jakobsen, “Body-worn spiral monopole antenna for body-centric communications”, in *Proceedings of the 2015 International Workshop on Antenna Technology*, IEEE, 2015, pp. 107–110.
- [P9] N. P. B. Kammersgaard, S. H. Kvist, J. Thaysen, and K. B. Jakobsen, “Impact of placement of in-the-ear antenna on ear-to-ear path gain”, in *Proceedings of 2015 Loughborough Antennas & Propagation Conference*, IEEE, 2015.
- [P10] N. P. I. Kammersgaard, S. H. Kvist, J. Thaysen, and K. B. Jakobsen, “Vertically polarized omnidirectional printed slot loop antenna”, in *Proceedings of Eucap 2015*, EurAAP, 2015.

CONTENTS

1	Introduction	1
2	Geometrical Theory of Diffraction for On-Body Propagation	5
2.1	Survey	5
2.2	Canonical Problem 1: Plane Wave Incident on Infinite Cylinder	6
2.3	Canonical Problem 2: Point Source on Infinite Cylinder	10
2.4	Numerical Validation	12
2.5	Generalized Expressions for all Convex Geometries	15
2.6	Summary	17
3	Ear-to-Ear Propagation Model	19
3.1	Survey	19
3.2	Propagation Model	20
3.3	Simulation and Numerical Implementation	21
3.4	Validation	25
3.5	Propagation Gain by Path	28
3.6	Summary	29
4	Antennas for Custom Hearing Instruments	31
4.1	Survey	31
4.2	Antennas	32
4.3	Placement	38
4.4	Summary	40
5	Conclusions	41
	Bibliography	43
	Paper 1: “Ear-to-Ear Propagation Model Based on Geometrical Theory of . . .	49
	Paper 2: “Geometrical Theory of Diffraction Formulation for On Body Propa- . . .	59
	Paper 3: “In-the-Ear Circular-Shaped Balanced Inverted-A Antenna for Hear- . . .	71
	Paper 4: “Body-Worn Antennas for Body-Centric Wireless Communications”	79

Paper 5: “Off-Body Transmission Range Improvement for Hearing Instruments . . .	87
Paper 6: “Validity of PEC Approximation for On-Body Propagation”	93
Paper 7: “Electromagnetic Fields at the Surface of Human-Body Cylinders”	99
Paper 8: “Body-Worn Spiral Monopole Antenna for Body-Centric Communica- . . .	105
Paper 9: “Impact of Placement of In-the-Ear Antenna on Ear-to-Ear Path Gain”	113
Paper 10: “Vertically Polarized Omnidirectional Printed Slot Loop Antenna”	119

INTRODUCTION

The area of wearable devices has exploded in recent years. Extensive research has been conducted within the area. It has also become a major focus of the electronics industry and a significant market as well. In May 2017 Apple's CEO, Tim Cook, claimed, that Apple's wearable division in itself would be a Fortune 500 company. One of the key enabling factors is the wireless connectivity of these body-worn devices. The area includes everything from smart watches through 'truly' wireless headsets to Hearing Instruments (HIs). The focus of this work will be on the wireless communication for HIs, specifically the antennas and propagation involved.

HIs are used by millions of people world-wide. Since hearing loss is common among elderly, the extended life expectancy increases the use of HIs. Likewise does the growing economical resources amongst the world's population. The expectations of the HI-users are rising simultaneously with the general technological development. Due to different user preferences and audiological needs, several categories of HIs exist. The three main categories are seen in Figure 1.1. The behind-the-ear (BTE) devices are situated behind the ear, and a small tube carries the sound generated in the device into the ear (Figure 1.1a). The receiver-in-the-ear (RIE or RITE) devices are primarily situated behind the ear, but the loudspeaker is placed in the ear canal (Figure 1.1b). The loudspeaker in a HI is referred to as the receiver, since it is the receiver of the amplified electrical signals generated in the HI. The placement of the receiver in the ear allows for a more compact and less visible device behind the ear. The devices and receiver are connected with small wires usually inside a thin plastic tube. The in-the-ear (ITE) devices are situated in the ear (Figure 1.1c). The category of ITE devices is subdivided depending on the placement in the ear. ITE refers to the largest version, with the smaller versions given more or less defined and self-explanatory names; In-the-canal (ITC), completely-in-the-canal (CIC), and invisible-in-the-canal (IIC). In contrast to BTE and RIE devices, the ITE devices usually need to be custom made to fit into the specific user's ear canal. Therefore, the category is also referred to as custom HIs. The process is typically as follows. An impression of the user's ear canal is taken by an audiologist. The impression is used to manufacture a shell that fits the user. The electronics are put into the shell, which is closed with a so-called faceplate situated furthest out of the ear. On the faceplate, the battery hatch, a button or a volume control can be placed. The focus of this work is the custom HIs.

Modern HIs have transformed from a simple analog amplifier to an intelligent digital device. One of the new features is the wireless connectivity. Through the

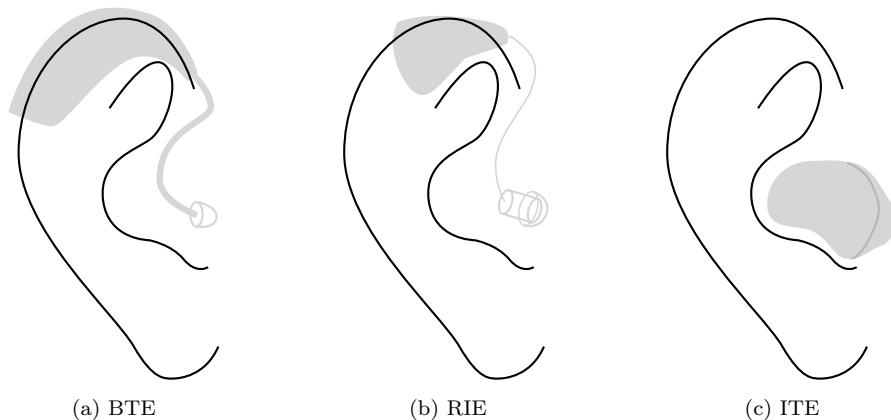


Figure 1.1. The hearing instrument categories (a) behind-the-ear (BTE), (b) receiver-in-the-ear (RIE), and (c) in-the-ear (ITE) are illustrated behind or in the ear.

wireless connection the HIs can connect with smart phones and other accessories. The HIs are virtually transformed into a headset. The HI-user can use this to talk on the phone without creating a self-amplifying loop that causes the familiar ringing of the HIs. The sound from the TV can be streamed directly to the HIs to overcome different volume preferences. Furthermore, a smart phone or an accessory may be used as a remote microphone to increase speech intelligibility in a noisy environment, such as a restaurant, or at far distances, for example at a lecture. The connection may also be used to remotely update the software and settings of the devices without having to visit an audiologist.

Communication between the HIs on opposite ears can improve the performance of the acoustic algorithms on the HIs. It is often referred to as ear-to-ear (E2E) communication. The HIs can share the input from the microphones and coordinate their settings. The two HIs' microphones can work in a similar manner as an antenna array to create directional application of the sound. This increases speech intelligibility by for example focusing on the sound from sources in front of the user. The communication between the devices may also be used to increase the range of the connection with accessories. This is explained and proven in [P5].

When the HIs first started to be fitted with wireless systems, the solutions varied. Some used near-field magnetic induction (NFMI) below 15MHz since it was easy to use for the E2E connection. NFMI has challenges connecting with off-body accessory or smart phones because of the short range of the near-fields. The solutions require a third device to bridge the NFMI to a different system with longer range. Different radio bands have been used, such as frequency modulation (FM) systems around 200 MHz or the 900 MHz industrial, scientific and medical (ISM) band. Now the industry is converging towards the 2.45 GHz ISM band, often using the Bluetooth[®] protocol. This is a world-wide license free band and offers connectivity with most wireless electronics. The 2.45 GHz ISM band will be the focus of this work.

The wireless connectivity is already widespread in BTE and RIE devices. This is in large part due to the work presented in [1]. The general understanding of the

propagation in proximity of the body already exists. A presentation of the progress within wireless communication for HIs done prior to this work is seen in [P4].

The custom devices are the most challenging devices from a wireless connectivity point of view. There are strict requirements to the size since they have to fit in the ear. The customization of the devices creates variation that is not seen in the BTE and RIE devices. Finally, the sometimes deep placement in the ear canal constitutes a difficult environment in which to design an efficient antenna. It is the hope that this work will help close some of the holes in the knowledge of body-centric propagation and antennas for custom HIs. The purpose of this work will be three-fold. Firstly, to improve the theoretical understanding of on-body propagation. Secondly, to increase the knowledge of the propagation mechanisms involved for E2E communication for custom HIs. Thirdly, to suggest suitable antenna concepts and guidelines for the design of antennas for custom HIs.

A theoretical study of the on-body propagation is done. A new geometrical theory of diffraction specifically for on-body propagation is derived. This is presented in Chapter 2. The theoretical results are used to construct a new ear-to-ear propagation model. The model is compared with and validated through simulations. The model is presented in Chapter 3. Different antennas and the impact of their placement in the ear is presented in Chapter 4. The study includes simulations and measurements of the antennas presented. The results are also compared with the modeled results to further validate the model. The conclusions are presented in Chapter 5.

The intent with this thesis is to provide an overview of the research done. The details of the different topics can be found in the papers [P1–P10], which are included at the end.

GEOMETRICAL THEORY OF DIFFRACTION FOR ON-BODY PROPAGATION

A theoretical study of the on-body propagation is performed in this chapter. First a short survey of the approximations of the human-body presented in the literature is done. The validity of the often used perfect electric conductor (PEC) approximation is discussed. A new geometrical theory of diffraction (GTD) formulation for on-body propagation is presented. This is done by the development of asymptotic solutions to two canonical problems from the eigenfunction solutions of those problems. The asymptotic (GTD) solution is numerically validated against the eigenfunction solution. Finally, the expression derived for the canonical problems is generalized to any convex lossy dielectric object. The chapter is based on the work done in [P2, P6, P7].

2.1 Survey

With the use of the terminology in [2] on-body communication and propagation refers to the link between two or more antennas on the body. This is in contrast to in-body propagation with an antenna inside the human body. Or off-body propagation, which is communication between an antenna on the body and an antenna off the body of that person, for example an antenna worn by another person or a base station. On-body and off-body communication can happen in a Line-of-Sight (LOS) or Non-Line-of-Sight (NLOS) condition. The E2E on-body communication between the HIs will always be NLOS. Likewise, the off-body communication from the HIs to an off-body accessory will often be with a NLOS condition for one of the HIs.

For NLOS on-body or off-body, the consensus is that at 2.45 GHz the energy does not propagate through the body because of the high dielectric loss. From the values specified as the standard for the human body at 2.45 GHz in [3], one can calculate the skin depth to be 2.4 mm. This demonstrates the high loss through the human body, for example the head. Instead, the most significant contribution comes from energy that creeps around the body [4–6]. Numerous models and approximations for the on-body propagation has been presented in the literature [7–18]. Several models have applied creeping wave theory, often GTD or uniform GTD (UTD), to the problem with significant success [7–9, 11, 12, 18]. Often the models are applied with an assumption that the applied GTD or UTD is a good approximation, without a detailed study of canonical problems that could justify the approximation.

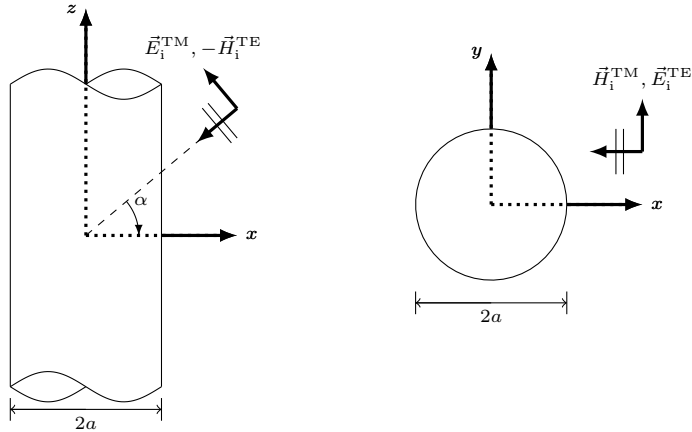


Figure 2.1. Side and top view of the geometry of the infinitely long dielectric cylinder model with an incident plane wave.

2.1.1 Validity of PEC Approximation

In many of the mentioned models an approximation of the human body as PEC is used [7, 9–13]. The papers listed often directly or indirectly justify the approximation based on the results from [13]. But since [13] addresses the disturbance of the channel between two antennas by a human passing through the LOS at 10 GHz, it is not valid for a general on-body approximation. Especially at 2.45 GHz where the human body has significantly different constitutive parameters. In the papers [P6, P7] the validity of the approximation was investigated and discussed. Based on the solution to the canonical problem of a plane wave incident on an infinitely long cylinder, the field around such a cylinder was found. The fields for a PEC cylinder and a human body cylinder were compared. It was found that the PEC approximation does model the general trends of the fields correctly, but the error for cylinders with radius comparable to the human torso or head can easily exceed 5 dB (This is also confirmed in Figure 2.3). Furthermore, the PEC approximation degrades significantly when the plane wave is obliquely incident compared to normal incidence. Therefore, it is necessary to avoid this approximation if a precise model is desired.

2.2 Canonical Problem 1: Plane Wave Incident on Infinite Cylinder

To develop a new and precise propagation model for the fields on the body, two canonical problems are solved. First the exact eigenfunction solution is found. The asymptotic solution is developed from the exact solution. The two canonical problems are finally generalized to any convex geometry. The first canonical problem is that of a plane wave incident on an infinite cylinder. In Figure 2.1 the geometry is shown. The focus is on the fields on the surface of the cylinder in NLOS. This geometry could correspond to off-body communication between a HI and an accessory.

2.2.1 Eigenfunction Solution

The eigenfunction solution was presented for the general case in [19]. The solution was also found in [20]. The approach of [20] with the use of potentials will be followed here. The solution for an infinite cylinder with an Impedance Boundary Condition (IBC) is given in [21] and a similar notation will be used here. The asymptotic solution for the IBC cylinder was found in [21] as well.

The definitions of the magnetic and electric vector potentials, \vec{A} and \vec{F} , from [22] are used. It can be shown that the potentials only have a z -component and furthermore that they satisfy the same wave equation as the fields:

$$(\nabla^2 + k_0^2) \begin{bmatrix} \vec{A} \\ \vec{F} \end{bmatrix} = (\nabla^2 + k_0^2) \begin{bmatrix} A_z \hat{z} \\ F_z \hat{z} \end{bmatrix} = 0 \quad (2.1)$$

where k_0 is the free space wavenumber.

The geometry and plane wave incidence enables the isolation of the z variation in the term $e^{jk_z z}$, where $k_z = k_0 \sin \alpha$ and α is the angle of incidence. The incident plane wave is written with the expansion of the $e^{j\rho \cos \phi \sin \alpha}$ term by the use of first order Bessel functions. This gives the following equations for the fields outside the cylinder:

$$\begin{bmatrix} A_z \\ F_z \end{bmatrix} = e^{jk_z z} \sum_{n=-\infty}^{\infty} j^n e^{-jn\phi} \begin{bmatrix} \tilde{A}_z \\ \tilde{F}_z \end{bmatrix} \quad (2.2)$$

where ϕ and z are the coordinates for the observation point. \tilde{A}_z and \tilde{F}_z is given by:

$$\begin{bmatrix} \tilde{A}_z^{\text{TM}} \\ \tilde{F}_z^{\text{TE}} \end{bmatrix} = \begin{bmatrix} C_0^{\text{m}} \\ C_0^{\text{e}} \end{bmatrix} \left(J_n(k_{t0}\rho) - \begin{bmatrix} A_n^{\text{m}} \\ A_n^{\text{e}} \end{bmatrix} H_n^{(2)}(k_{t0}\rho) \right) \quad (2.3a)$$

$$\begin{bmatrix} \tilde{F}_z^{\text{TM}} \\ \tilde{A}_z^{\text{TE}} \end{bmatrix} = \begin{bmatrix} -C_0^{\text{e}} \\ C_0^{\text{m}} \end{bmatrix} A_n^{\text{c}} H_n^{(2)}(k_{t0}\rho) \quad (2.3b)$$

where ρ is the coordinate of the observation point, $k_{t0} = \sqrt{k_0^2 - k_z^2} = k_0 \cos \alpha$ and η_0 is the intrinsic impedance of free space and:

$$C_0^{\text{m}} = E_0 \frac{j}{\eta_0 k_{t0}} \quad (2.4a)$$

$$C_0^{\text{e}} = E_0 \frac{1}{j k_{t0}} \quad (2.4b)$$

The expressions for the fields inside the cylinder can be found in [19, 20]. The tangential fields inside and outside the cylinder is equated at the surface of the cylinder to satisfy the boundary conditions for each term of the summation. Thereby, one finds the following expressions for the constants:

$$\begin{bmatrix} A_n^{\text{m}} \\ A_n^{\text{e}} \end{bmatrix} = \frac{J_n(k_{t0}a) \left(\begin{bmatrix} F_n N_n \\ G_n M_n \end{bmatrix} - q_c^2 \right)}{H_n^{(2)}(k_{t0}a) (F_n G_n - q_c^2)} \quad (2.5a)$$

$$A_n^{\text{c}} = \frac{2q_c}{\pi(k_{t0}a) \left(H_n^{(2)}(k_{t0}a) \right)^2 (F_n G_n - q_c^2)} \quad (2.5b)$$

with

$$\begin{bmatrix} F_n \\ G_n \end{bmatrix} = \frac{H_n^{(2)'}(k_{t0}a)}{H_n^{(2)}(k_{t0}a)} - \begin{bmatrix} q_e \\ q_m \end{bmatrix} \frac{J_n'(k_{t1}a)}{J_n(k_{t1}a)} \quad (2.6a)$$

$$\begin{bmatrix} M_n \\ N_n \end{bmatrix} = \frac{J_n'(k_{t0}a)}{J_n(k_{t0}a)} - \begin{bmatrix} q_e \\ q_m \end{bmatrix} \frac{J_n'(k_{t1}a)}{J_n(k_{t1}a)} \quad (2.6b)$$

where $k_{t1} = \sqrt{k_1^2 - k_z^2}$ and k_1 is the wavenumber of the lossy dielectric. And finally,

$$q_m = \frac{\epsilon_1 k_{t0}}{\epsilon_0 k_{t1}} \quad (2.7a)$$

$$q_e = \frac{\mu_1 k_{t0}}{\mu_0 k_{t1}} \quad (2.7b)$$

$$q_c = \frac{nk_z}{k_{t0}k_0a} \left(1 - \left(\frac{k_{t0}}{k_{t1}} \right)^2 \right) \quad (2.7c)$$

where ϵ_1 and μ_1 are the permittivity and permeability of the lossy dielectric, respectively.

2.2.2 Asymptotic Solution

To enable the calculation of the asymptotic solution of (2.3) an assumption is made to simplify the fractions $\frac{J_n'(k_{t1}a)}{J_n(k_{t1}a)}$. The Debye representation of the Bessel function given in [23] can be used to rewrite the fractions:

$$\begin{aligned} \frac{J_n'(k_{t1}a)}{J_n(k_{t1}a)} &\approx \sqrt{1 - \left(\frac{n}{k_{t1}a} \right)^2} \tan \left(a \sqrt{1 - \left(\frac{n}{k_{t1}a} \right)^2} - jn \operatorname{acosh} \left(\frac{n}{k_{t1}a} \right) + \frac{\pi}{4} \right) \\ &\approx j \sqrt{1 - \left(\frac{n}{k_{t1}a} \right)^2} \end{aligned} \quad (2.8)$$

The first approximation is valid for n and $k_{t1}a$ large, but as long as just k_{t1} is large the approximation is good. The second approximation is valid when the argument of the tangent function is large. When the cylinder is opaque, $k_{t1}a$ has a large imaginary part and therefore the approximation will be valid.

When this simplification has been done, it is possible to perform the Watson transformation on the sum in (2.3) [24]. Thereby, n is replaced by a continuous variable v and the sum is transformed into a line integral. Furthermore, the following Fock transformation is performed [25]:

$$v = k_{t0}a + m_t \tau \quad (2.9)$$

with $m_t = (k_{t0}a/2)^{1/3}$. This enables the use of the approximation of the Hankel function $H_v^{(1,2)}(k_{t0}a)$ by the Fock-Airy functions $W_{1,2}(\tau)$ when $v \sim k_{t0}a$. By changing the integration path, from encircling the real axes to encircling the upper half of the

complex plane, the integral can be evaluated by the Cauchy residue theorem. The asymptotic solution becomes:

$$\begin{bmatrix} A_z^{\text{TM}} \\ F_z^{\text{TE}} \end{bmatrix}^{\pm} \sim \sum_{p=1}^{\infty} \begin{bmatrix} C_0^{\text{m}} \\ C_0^{\text{e}} \end{bmatrix} \begin{bmatrix} D_p^{\text{m}} \\ D_p^{\text{e}} \end{bmatrix} \sqrt{\frac{k_0\pi}{2j}} \cos \alpha H_v^{(2)}(k_{t0}\rho) e^{-jk_0t \cos^2 \alpha - \alpha_p t} \quad (2.10a)$$

$$\begin{bmatrix} F_z^{\text{TM}} \\ A_z^{\text{TE}} \end{bmatrix}^{\pm} \sim \sum_{p=1}^{\infty} \begin{bmatrix} -C_0^{\text{e}} \\ C_0^{\text{m}} \end{bmatrix} D_p^{\text{c}} \sqrt{\frac{k_0\pi}{2j}} \cos \alpha H_v^{(2)}(k_{t0}\rho) e^{-jk_0t \cos^2 \alpha - \alpha_p t} \quad (2.10b)$$

where t is the distance the rays travel on the surface of the cylinder along the helical geodesic paths. The \pm refers to the direction of travel. The '+' corresponds to counter-clockwise travel where $t = \frac{(\phi - \pi/2)a}{\cos \alpha}$. The '-' corresponds to clockwise travel where $t = \frac{(3\pi/2 - \phi)a}{\cos \alpha}$. Multiple encirclements can be included by dividing with $1 - e^{-jk_{t0}2\pi a - \alpha_p 2\pi a / \cos \alpha}$ which for all relevant situations is equivalent to 1. The diffraction constants are given by:

$$D_p^{m,e} = \frac{2\pi m_t^2 \left(\frac{-W_2'(\tau)}{m_t W_2(\tau)} - jq_{e,m} \sqrt{1 - \left(\frac{k_{t0}a + m_t \tau_p}{k_{t1}a} \right)^2} \right)}{\sqrt{\frac{k_0\pi}{2j}} \cos \alpha D_w'(\tau_p)} \quad (2.11a)$$

$$D_p^{\text{c}} = \pm \frac{2j\pi m_t^2 q_c(\tau_p)}{\sqrt{\frac{k_0\pi}{2j}} \cos \alpha D_w'(\tau_p)} = \pm \sqrt{-D_p^{\text{m}} D_p^{\text{e}}} \quad (2.11b)$$

where τ_p is the p 'th singularity of A_n^{m} , A_n^{e} , and A_n^{c} in the upper half of the complex plane given by the p 'th zero of

$$\begin{aligned} D_w(\tau) = & \left(W_2'(\tau) + jm_t q_e \sqrt{1 - \left(\frac{k_{t0}a + m_t \tau}{k_{t1}a} \right)^2} W_2(\tau) \right) \\ & \cdot \left(W_2'(\tau) + jm_t q_m \sqrt{1 - \left(\frac{k_{t0}a + m_t \tau}{k_{t1}a} \right)^2} W_2(\tau) \right) - [m_t q_c(\tau) W_2(\tau)]^2 \end{aligned} \quad (2.12)$$

and $D_w'(\tau)$ is the derivative of $D_w(\tau)$ with respect to τ . In Equation 2.11b the correct branch of the square root has to be used so that the equal sign is correct. By substitution of n with v and then with $k_{t0}a + m_t \tau$ the expressions for $q_c(\tau)$ and $q_c'(\tau)$ can be found:

$$q_c(\tau) = \left(1 + \frac{\tau}{2m_t^2} \right) \frac{k_z}{k_0} \left(1 - \left(\frac{k_{t0}}{k_{t1}} \right)^2 \right) \quad (2.13a)$$

$$q_c'(\tau) = \frac{1}{2m_t^2} \frac{k_z}{k_0} \left(1 - \left(\frac{k_{t0}}{k_{t1}} \right)^2 \right) \quad (2.13b)$$

The attenuation factor is given by

$$\alpha_p = j \frac{m_t \cos \alpha}{a} \tau_p \quad (2.14)$$

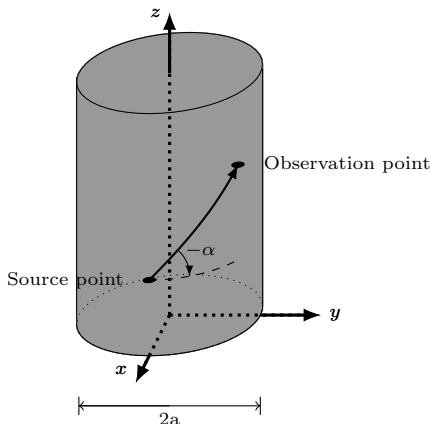


Figure 2.2. The geometry of the infinitely long dielectric cylinder model with a source and observation point. The source and observation points are connected by the shortest path between them.

The τ_p 's are found to be approximately along the line which originates in origo and makes an angle of -60° with the real axis in the complex plane. Therefore, the α_p 's will have an imaginary part which will effectively increase the wave number. The wavelength along the cylinder is therefore shorter than the free space wavelength.

2.3 Canonical Problem 2: Point Source on Infinite Cylinder

The second canonical problem is that of a point source located on the surface of an infinitely long cylinder. The geometry is shown in Figure 2.2. The eigenfunction solution has been found for a PEC and IBC cylinder in [26–28] and [29–31], respectively. The generalized eigenfunction solution for a dielectric cylinder with the source at an arbitrary location inside or outside the cylinder is found in [32]. However [32] does not provide the final closed-form expressions, but sets of equations to be solved and combined numerically. The asymptotic solution for PEC and IBC cylinders are found in [26–28] and [29–31], respectively.

2.3.1 Eigenfunction Solution

For simplicity and without loss of generality, the source point is assumed to be at $(x = a, y = 0, z = 0)$. The magnetic and electric vector potentials are used again. The following Fourier transform pair is used [22]:

$$A_z = \frac{1}{2\pi} \sum_{n=-\infty}^{\infty} e^{jn\phi} \int_{-\infty}^{\infty} \tilde{A}_z e^{jk_z z} dk_z \quad (2.15a)$$

$$F_z = \frac{1}{2\pi} \sum_{n=-\infty}^{\infty} e^{jn\phi} \int_{-\infty}^{\infty} \tilde{F}_z e^{jk_z z} dk_z \quad (2.15b)$$

where ϕ and z are the coordinates of the observation point. The potentials from z - and ϕ -oriented sources can be found by the use of the boundary conditions on the surface of the cylinder. From these potentials and the use of reciprocity, the potential from ρ -oriented sources can be found. The potentials from the electric ρ -oriented sources become:

$$\tilde{A}_z = \frac{H_n^{(2)}(k_{t0}\rho)}{2\pi a k_{t0} (F_n G_n - q_c^2) H_n^{(2)}(k_{t0}a)} \left(\frac{jnk_0}{k_{t0}^2 a} q_c - \frac{jk_z H_n^{(2)'}(k_{t0}a)}{k_{t0} H_n^{(2)}(k_{t0}a)} F_n \right) J_\rho \quad (2.16a)$$

$$\tilde{F}_z = \frac{H_n^{(2)}(k_{t0}\rho)}{2\pi a k_{t0} (F_n G_n - q_c^2) H_n^{(2)}(k_{t0}a)} \left(\frac{nk_0 \eta_0}{k_{t0}^2 a} G_n - \frac{k_z \eta_0 H_n^{(2)'}(k_{t0}a)}{k_{t0} H_n^{(2)}(k_{t0}a)} q_c \right) J_\rho \quad (2.16b)$$

where J_ρ is the ρ -oriented electric source. The constants are the same as for the plane wave incidence except for k_z , which is a variable here. This change affects the other constants as well, but their definitions stay the same.

2.3.2 Asymptotic Solution

As with the case of plane wave incidence the expressions for the potentials are simplified by the use of Equation 2.8. The Watson transformation performed and the Fock substitution from Equation 2.9 is used. The integral over k_z is evaluated by the use of the steepest decent method where only the first order approximation in the asymptotic expansion is used. The details of this process are well outlined in [33]. The result for the potentials caused by a ρ -oriented electric source are given by:

$$A_z = J_\rho \sqrt{\frac{k_0 \pi}{2j}} \cos \alpha \sqrt{\frac{\pi}{2jk_0 t}} \frac{jk_0}{4\pi} H_v^{(2)}(k_{t0}\rho) e^{-jk_0 t - \alpha_p t} \cdot \left(\frac{ju}{k_{t0}a} D_p^e H_v^{(2)}(k_{t0}a) + \sin(\alpha) D_p^m H_v^{(2)'}(k_{t0}a) \right) \quad (2.17a)$$

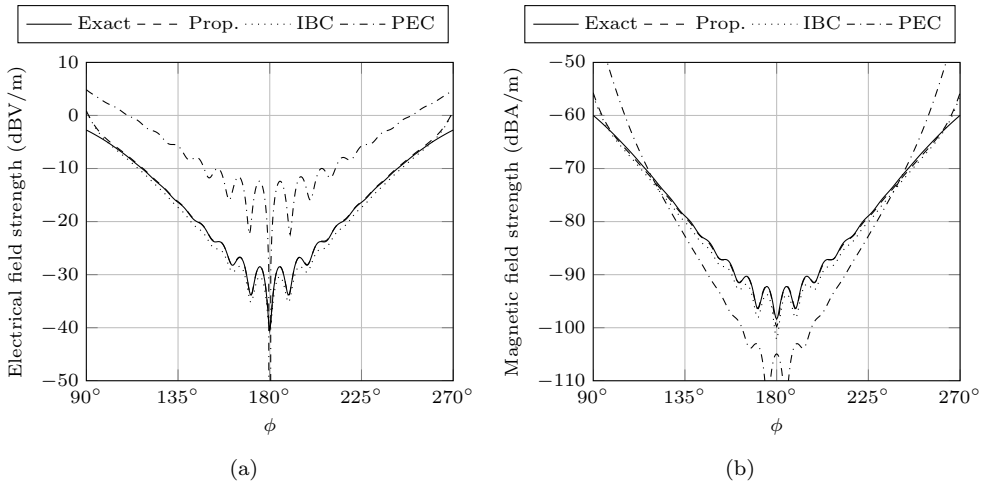
$$F_z = J_\rho \sqrt{\frac{k_0 \pi}{2j}} \cos \alpha \sqrt{\frac{\pi}{2jk_0 t}} \frac{jk_0 \eta_0}{4\pi} H_v^{(2)}(k_{t0}\rho) e^{-jk_0 t - \alpha_p t} \cdot \left(\frac{ju}{k_{t0}a} D_p^e H_v^{(2)}(k_{t0}a) - \sin(\alpha) D_p^c H_v^{(2)'}(k_{t0}a) \right) \quad (2.17b)$$

From the potentials the ρ -oriented electric field from a ρ -oriented electric source is calculated resulting in:

$$E_\rho = J_\rho \frac{k_0 \pi}{2j} \cos^2 \alpha \frac{jk_0 \eta_0}{4\pi} \frac{e^{-jk_0 t - \alpha_p t}}{\sqrt{t}} \left[H_v^{(2)}(k_{t0}\rho) \left(\frac{v^2}{k_{t0}^2 a \rho} D_p^e H_v^{(2)}(k_{t0}a) + \frac{ju \sin \alpha}{k_{t0} \rho} D_p^c H_v^{(2)'}(k_{t0}a) \right) + H_v^{(2)'}(k_{t0}\rho) \left(\frac{ju \sin \alpha}{k_{t0} a} D_p^e H_v^{(2)}(k_{t0}a) + \sin^2 \alpha D_p^m H_v^{(2)'}(k_{t0}a) \right) \right] \quad (2.18)$$

Table 2.1. Constitutive parameters of different tissues

Tissue	2.45 GHz		5.8 GHz	
	σ (S/m)	ϵ_r	σ (S/m)	ϵ_r
Muscle [36]	1.74	52.7	4.96	48.5
Skin [36]	1.46	38.0	3.72	35.1
Fat [36]	0.105	5.28	0.293	4.95
Standard [3]	1.8	39.2	5.27	35.3

**Figure 2.3.** Field plots for a 'fat' cylinder with $a = 160$ mm and $\alpha = 30^\circ$ at 5.8 GHz. Electric field strength in the TE case (a) and magnetic field strength in the TM case (b).

2.4 Numerical Validation

To verify that the asymptotic expression can be used, numerical comparison between the exact eigenfunction solution and the asymptotic solution was done for the plane wave incidence case. A study of the constitutive parameters for different kinds of human tissue is found in [34–36]. In [36] the different tissues were modeled so the constitutive parameters can be estimated for a wide frequency range. In [3] human tissue average parameters to be used for testing is given. The values at 2.45 GHz and 5.8 GHz is seen in Table 2.1.

First, the proposed asymptotic solution is compared with the exact eigenfunction solution, the IBC asymptotic solution [21] and the PEC asymptotic solution. The comparizon is done for a cylinder with radius $a = 160$ mm and with the constitutive parameters of fat at 5.8 GHz. This could for example correspond to approximately the radius of the human torso. The plane wave is incident at an angle $\alpha = 30^\circ$. The results are seen for the electric fields on the surface in the case of a TE incident plane wave in Figure 2.3a. For the TM incident plane wave the magnetic fields are seen in Figure 2.3b. The magnetic fields are used since the electric fields in the TM case with the PEC approximation is zero. Thereby, the PEC approximation of the fields

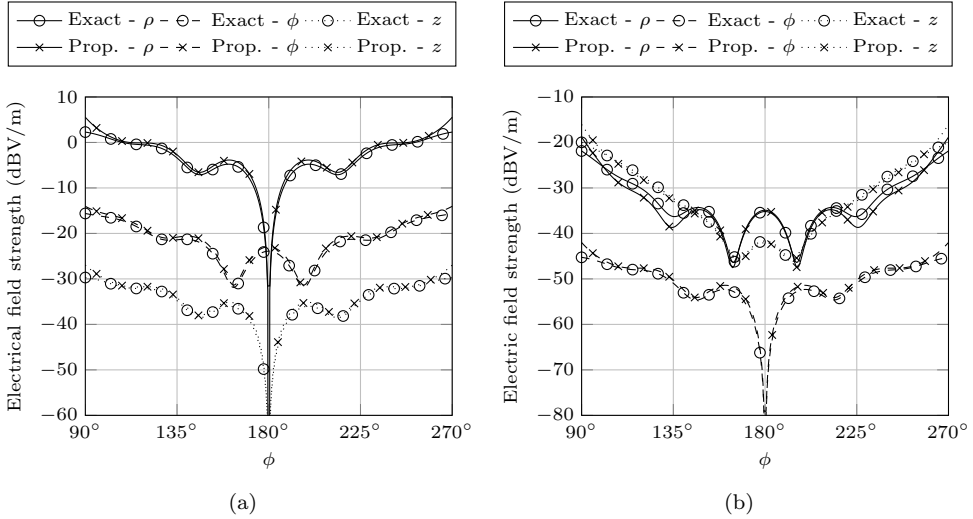


Figure 2.4. Field plots for a 'human standard' cylinder with $a = 80$ mm and $\alpha = 10^\circ$ at 2.45 GHz. Electric field strength for each polarization in TE (a) and TM (b) case.

over the surface can be still be compared with the other approximations. It is seen that the PEC approximation is more than 10 dB away from the exact solution in both cases. In the TM case the locations of the constructive and destructive interference are also wrong for the PEC approximation. This is due to the fact that the coupling mode from the TM to TE mode, with the constant A_n^c , is dominant in the deep shadow for the TM incident field. The IBC approximation is seen to be within 1-2 dB of the exact solution in almost the entire shadow region. This approximation would for most purposes be accurate enough. Still, it is seen that the proposed dielectric approximation is more accurate. The proposed approximation is hard to distinguish from the exact solution for the entire shadow region, besides from the transition region close to the lit region at $\sim 90^\circ$ and $\sim 270^\circ$.

From Table 2.1, it is seen that for muscle and skin the parameters are close to that of the human average specified in the standard. Therefore, to investigate the accuracy of the proposed approximation, for a geometry with the size of the human head, the fields on the surface of a cylinder, with radius $a = 80$ mm and with human average constitutive parameters as given in [3], are found at 2.45 GHz. The plane wave is incident at an angle $\alpha = 10^\circ$. The field with a TE and TM incident plane wave for each of the polarizations are shown in Figure 2.4. It is seen that the model is capable of approximating each of the polarizations to within a few dB. Since $k_0 a = 4.1$, this demonstrates that the model is valid even for cases where the assumption of $k_0 a \gg 1$ is not fully valid.

The relative root-mean-square error of the electric field vector was calculated for a sweep of the geometrical parameters of a cylinder with human average constitutive parameters. The fields in the deep shadow region for $135^\circ < \phi < 225^\circ$ is included. This was done to find the area of validity for the approximation. The sweep was done for the geometry given by the electrical length of the radius of the cylinder together with the angle of incidence, but also for the geometry given by the electrical

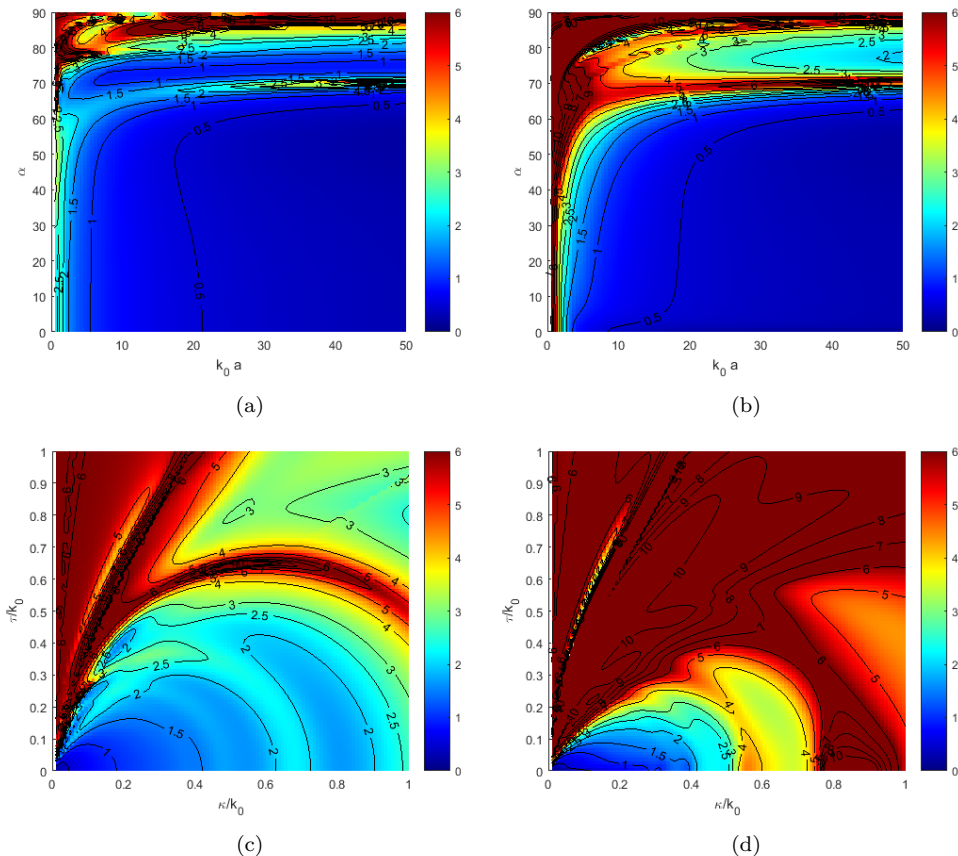


Figure 2.5. Root-mean-square of the relative error in the electric field in the deep shadow for different cylinders in decibels. As function of the electrical length of the cylinder $k_0 a$ and the angle of incidence α for the TE (a) and TM (b) cases. As function of the electrical curvature $\frac{\kappa}{k_0}$ and the electrical torsion $\frac{\tau}{k_0}$ of the cylinder for the TE (c) and TM (d) cases.

curvature and torsion of the geodesic helix path the waves will follow. The root-mean-square error given in dB is seen in Figure 2.5. It is seen that for larger geometries the approximation is more precise, which is in alignment with the conditions for the approximation. The approximation breaks down at high angles of incidence. This is caused by the fact that k_{t0} becomes small. This demonstrates that the approximation is valid for opaque geometries down to a size $a > \lambda/2$ or $\frac{\kappa}{\kappa^2 + \tau^2} > \lambda/2$ and up to a limited torsion of $\alpha < 60^\circ$ or $\tau/\kappa < 2$.

2.5 Generalized Expressions for all Convex Geometries

The diffracted field \vec{E}^d in the deep shadow away from the cylinder caused by an incident plane wave \vec{E}^i can be described as:

$$\vec{E}^d \sim \vec{E}^i \cdot \bar{\bar{T}} \frac{e^{-jk_0 s}}{\sqrt{s}} e^{-jk_0 t - \alpha_p t} \quad (2.19)$$

where

$$\bar{\bar{T}} \sim \sum_{p=1}^{\infty} \left(\hat{b}' \hat{b} D_p^m + \hat{b}' \hat{n} D_p^c - \hat{n}' \hat{b} D_p^c + \hat{n}' \hat{n} D_p^e \right) \quad (2.20)$$

where $(\hat{t}', \hat{n}', \hat{b}')$ are the unit vectors at the source or ingoing grazing point and $(\hat{t}, \hat{n}, \hat{b})$ are the unit vectors at the observation or outgoing grazing point. The shift in sign of D_p^c is explained by the shift of direction of \hat{b} dependent on the way of travel. The equation can be rewritten to:

$$\bar{\bar{T}} \sim \sum_{p=1}^{\infty} \left(\hat{b}' D_{p,i}^m + \hat{n}' D_{p,i}^e \right) \left(\hat{b} D_{p,o}^m + \hat{n} D_{p,o}^e \right) \quad (2.21)$$

where the 'i' and 'o' subscript refers to incoming or outgoing waves with respect to the cylinder. The magnitudes of the constants are given by:

$$|D_{p,i}^m| = |D_{p,o}^m| = \left| \sqrt{D_p^m} \right| \quad (2.22a)$$

$$|D_{p,i}^e| = |D_{p,o}^e| = \left| \sqrt{D_p^e} \right| \quad (2.22b)$$

where phases are chosen in such a way that:

$$D_{p,i}^m D_{p,o}^m = D_p^m \quad (2.23a)$$

$$D_{p,i}^m D_{p,o}^e = D_p^c \quad (2.23b)$$

$$D_{p,i}^e D_{p,o}^m = -D_p^c \quad (2.23c)$$

$$D_{p,o}^e D_{p,i}^e = D_p^e \quad (2.23d)$$

The fields on the cylinder from an incident plane wave can be described as well. In the deep shadow on the cylinder the diffracted fields \vec{E}^d from an incident plane wave \vec{E}^i will be given by:

$$\vec{E}^d \sim \vec{E}^i \cdot \bar{\bar{S}} e^{-jk_0 t - \alpha_p t} \quad (2.24)$$

where

$$\bar{\bar{S}} \sim \sum_{p=1}^{\infty} \left(\hat{b}' D_{p,i}^m + \hat{n}' D_{p,i}^e \right) \left(\hat{t} A_{p,t}^e + \hat{b} A_{p,b}^e + \hat{n} A_{p,n}^e \right) \quad (2.25)$$

with the attachment coefficient given by: (The argument, $k_{t0}a$, of the Hankel functions has been suppressed)

$$\begin{aligned}
A_{p,n}^e &= \sqrt{\frac{k_0\pi}{2j}} \cos \alpha \left(\frac{v}{k_{t0}a} D_{p,o}^e H_v^{(2)} - j \sin \alpha D_{p,o}^m H_v^{(2)'} \right) \\
A_{p,b}^e &= \sqrt{\frac{k_0\pi}{2j}} \cos \alpha \left[j \sin \alpha D_{p,o}^e H_v^{(2)'} + \left(1 + \frac{m_t \tau_p \sin^2 \alpha}{k_{t0}a} \right) D_{p,o}^m H_v^{(2)} \right] \\
A_{p,t}^e &= \sqrt{\frac{k_0\pi}{2j}} \cos \alpha \left[-j \cos \alpha D_{p,o}^e H_v^{(2)'} - \left(\frac{m_t \tau_p \cos \alpha \sin \alpha}{k_{t0}a} \right) D_{p,o}^m H_v^{(2)} \right] \quad (2.26)
\end{aligned}$$

Equivalently the diffracted fields \vec{E}^d in the shadow part of the far-field from a point source \vec{J}_i on the surface can be found by reciprocity to be:

$$\vec{E}^d \sim \frac{jk_0\eta_0}{4\pi} \vec{J}_i \cdot \bar{\bar{U}} \frac{e^{-jk_0t - \alpha_p t}}{\sqrt{t+s}} \frac{e^{-jk_0s}}{\sqrt{s}} \quad (2.27)$$

where

$$\bar{\bar{U}} \sim \sum_{p=1}^{\infty} \left(\hat{t}' L_{p,t}^e + \hat{b}' L_{p,b}^e + \hat{n}' L_{p,n}^e \right) \left(\hat{b} D_{p,o}^m + \hat{n} D_{p,o}^e \right) \quad (2.28)$$

The launching coefficients are given by:

$$\begin{aligned}
L_{p,n}^e &= \sqrt{\frac{k_0\pi}{2j}} \cos \alpha \left(\frac{v}{k_{t0}a} D_{p,i}^e H_v^{(2)} + j \sin \alpha D_{p,i}^m H_v^{(2)'} \right) \\
L_{p,b}^e &= \sqrt{\frac{k_0\pi}{2j}} \cos \alpha \left[j \sin \alpha D_{p,i}^e H_v^{(2)'} - \left(1 + \frac{m_t \tau_p \sin^2 \alpha}{k_{t0}a} \right) D_{p,i}^m H_v^{(2)} \right] \\
L_{p,t}^e &= \sqrt{\frac{k_0\pi}{2j}} \cos \alpha \left[-j \cos \alpha D_{p,i}^e H_v^{(2)'} + \left(\frac{m_t \tau_p \cos \alpha \sin \alpha}{k_{t0}a} \right) D_{p,i}^m H_v^{(2)} \right] \quad (2.29)
\end{aligned}$$

By the use of the launching and attachment coefficients the field on the cylinder caused by a source \vec{J}_i on the cylinder can be found as:

$$\vec{E}^d \sim \frac{jk_0\eta_0}{4\pi} \vec{J}_i \cdot \bar{\bar{V}} \frac{e^{-jk_0t - \alpha_p t}}{\sqrt{t}} \quad (2.30)$$

where

$$\bar{\bar{V}} \sim \sum_{p=1}^{\infty} \left(\hat{t}' L_{p,t}^e + \hat{b}' L_{p,b}^e + \hat{n}' L_{p,n}^e \right) \left(\hat{t} A_{p,t}^e + \hat{b} A_{p,b}^e + \hat{n} A_{p,n}^e \right) \quad (2.31)$$

The coefficients first determined from the plane wave incidence case matches with the ones from the infinitesimal dipole source case.

The behavior of the creeping wave on the body has been described by the use of the unit vectors which are defined by the geodesic paths. The only thing that remains

is to replace a , $\cos \alpha$ and $\sin \alpha$ with expressions not specific to the cylinder. This can be done by the use of:

$$a = \frac{\kappa}{\kappa^2 + \tau^2} \quad (2.32a)$$

$$\cos \alpha = \frac{\kappa}{\sqrt{\kappa^2 + \tau^2}} \quad (2.32b)$$

$$\sin \alpha = \frac{-\tau}{\sqrt{\kappa^2 + \tau^2}} \quad (2.32c)$$

where κ and τ are the surface ray curvature and torsion, respectively. Furthermore, when the term $\frac{1}{\sqrt{t}}$ or $\frac{1}{\sqrt{t+s}}$ appears one should replace it with:

$$\frac{1}{\sqrt{t}} \sqrt{\frac{d\chi_0}{d\chi}} = \sqrt{\frac{d\psi_0}{d\chi}} \quad (2.33)$$

where $d\chi$ and $d\chi_0$ are the distance between adjacent rays at the observation and source point, respectively. $d\psi_0 = d\chi_0/t$ is the angle between adjacent rays at the source. Finally the attenuation will be variable over the surface since the curvature and torsion along a geodesic may change for a general geometry in contrast to a cylinder. Therefore, the term $\alpha_p t$ should be replaced by $\int_0^t \alpha_p(t') dt'$. From these equations, the fields in the proximity of the human body or any opaque lossy dielectric object, and in the deep shadow region can be determined for any convex geometry.

2.6 Summary

In this chapter a new geometrical theory of diffraction for lossy dielectric materials has been developed and presented. First, the necessity of such a model was investigated and justified through a survey of the existing models and discussion of the often used perfect electric conductor approximation of the human body. The geometrical theory of diffraction was developed by finding the eigenfunction solution for two canonical problems and then transforming these into the asymptotic solution. The asymptotic solution was verified through numerical comparisons for one of the canonical problems. Finally, the asymptotic geometrical theory of diffraction solutions were generalized to all convex geometries. The new formulation is an original expansion to geometrical theory of diffraction, which has not been presented previously in the literature.

EAR-TO-EAR PROPAGATION MODEL

A study of the ear-to-ear (E2E) propagation between antennas on opposite ears is done in this chapter. A short survey of the existing E2E models is performed. Thereafter, a new ear-to-ear propagation model is presented. The model is based on the geometrical theory of diffraction for on-body propagation presented in Chapter 2. The challenges in the numerical implementation of the model is discussed. The model is validated against simulation results. Finally, the path gain in different directions around the head is compared. The chapter is based on the work done in [P1].

3.1 Survey

As mentioned in Section 2.1, numerous propagation models for on-body communication are found in the literature [7–18]. For NLOS conditions at 2.45 GHz, the models, including the model in Chapter 2, conclude that the propagation occurs through creeping waves above the surface of the body. This is also the case for the E2E communication. A few models specifically relating to the E2E connection have been presented [7, 9, 18].

In [18] the head is modeled as an infinitely long cylinder, and creeping wave attenuation over a lossy ground is used to calculate the field strength on the surface of the head. The results are validated against measurements. The main behavior is confirmed by the measurements, but the exact constructive and destructive interference in the deep shadow is not confirmed. It should be noted that these kinds of measurements are notoriously hard to perform. This is caused by the very low signal levels and high sensitivity to placement and reflections.

In [7] the E2E propagation is modeled by an infinitely long PEC cylinder with an elliptical cross-section. The theoretical expressions are based on GTD. The model is validated against simulations, but measurements that confirm the level of the simulations are also included. The ear pinna is modeled as a dielectric slab with human parameters.

The E2E propagation was investigated in [37, 38]. Based on these investigations, an E2E model was proposed [9]. The model is an extension of the model in [7]. Instead of two elliptic paths, the model uses N elliptical paths. The number of paths are increased until convergence. Each of these elliptical paths are fitted to the head. Instead of trying to model the effect of the pinna, the model uses an on-body gain that includes the effect of the pinna, and is obtained from simulations.

All these models have one deficit in common. They fail to address what paths around the head the propagation will happen along. Furthermore, they model the head as a canonical shape instead of its true shape. Finally, the head is modeled by PEC instead of lossy dielectric in [7, 9]. The model presented here attempts to address these matters.

A study of the behavior of the E2E channel in a multi-scattering environment is found in [39]. Possibilities of using diversity is discussed in [40, 41]. Issues with interference and a possible software channel selection algorithm is presented in [42]. The area of the E2E channel in a non-anechoic environment will not be discussed further here.

3.2 Propagation Model

In Chapter 2 it was shown how to calculate the diffracted fields from a point source on any given lossy dielectric convex opaque structure. These results are used in the following to obtain a specific model for the head. For now we ignore the few concave areas of the head. The diffracted fields from an electric point source \vec{J}_1 on the surface of the head along a given geodesic line are given by:

$$\vec{E}^d \sim \frac{jk_0\eta_0}{4\pi} \vec{J}_1 \cdot \bar{\bar{V}} e^{-jk_0t} \sqrt{\frac{d\psi_0}{d\chi}} \quad (3.1)$$

where $\eta_0 = \sqrt{\frac{\mu_0}{\epsilon_0}}$ is the intrinsic impedance of free space. $k_0 = \omega\sqrt{\epsilon_0\mu_0}$ is the wavenumber of free space and ω the radial frequency. t is the distance from the source along the geodesic. $d\chi$ is the distance between adjacent rays at the observation point. $d\psi_0$ is the angle between adjacent rays at the source. And where:

$$\bar{\bar{V}} \sim \sum_{p=1}^{\infty} \left(\hat{t}' L_{p,t}^e + \hat{b}' L_{p,b}^e + \hat{n}' L_{p,n}^e \right) \left(\hat{t} A_{p,t}^e + \hat{b} A_{p,b}^e + \hat{n} A_{p,n}^e \right) e^{-\int_0^t \alpha_p dt} \quad (3.2)$$

where $(\hat{t}', \hat{n}', \hat{b}')$ are the tangential, normal, and binormal unit vectors, respectively, at the source point and similarly $(\hat{t}, \hat{n}, \hat{b})$ are the unit vectors at the observation point. The $L_{p,i}^e$ and $A_{p,i}^e$ are launching and attachment coefficients for electrical points source of specific polarizations. And α_p is the attenuation of the creeping wave. The expressions are found in Equations (2.14), (2.26) and (2.29). The subscript p refers to different modes, but in the deep shadow the first mode is all dominant and the summation over p will not be done here. Instead, only the first mode will be used. Furthermore, the tangential and binormal contribution will be ignored. This is done because the magnitude of the launching and attachment coefficients for the first mode on the human body are more than 20dB higher for the normal component than the tangential and binormal components.

The electric field transmitted by an antenna in the polarization normal to the surface of the body of interest, $E_T^{\hat{n}}$, can be expressed through the gain, G_T , and the transmit power, P_T , as:

$$E_T^{\hat{n}} = \sqrt{\frac{2\eta_0 P_T G_T^{\hat{n}}}{4\pi}} e^{j\angle E_T^{\hat{n}}} \frac{e^{-jk_0r}}{r} \quad (3.3)$$

where r is the distance away from the antenna. Note that the angle of the electric field transmitted by an antenna, $\angle E_{\text{T}}^{\hat{n}}$ is only meaningful when the polarization is given. The transmitted electric field multiplied by $r e^{jk_0 r}$ will take the place of the term $\frac{jk_0 \eta_0}{4\pi}$ in Equation 3.1. This makes sense since the term $\frac{jk_0 \eta_0}{4\pi}$ is exactly the magnitude of the electric fields radiation from a unit strength electric dipole source. For convenience the reference to the normal component, \hat{n} , will be suppressed.

The received electric field normal to the surface, E_{R} , can then be calculated for a geodesic path:

$$E_{\text{R}} = \sqrt{\frac{2\eta_0 P_{\text{T}} G_{\text{T}}}{4\pi}} e^{j\angle E_{\text{T}}} L A e^{-jk_0 t - \int_0^t \alpha dt} \sqrt{\frac{d\psi_0}{d\chi}} \quad (3.4)$$

By adding all of the contributions from each of the geodesic paths that connect the transmitting and receiving antenna, the total open circuit voltage at the terminals of the receiving antenna can be found:

$$V_{\text{OC}} = \sum_{i=1}^N E_{\text{R},i} \ell_{e,i} \quad (3.5)$$

where N is the total number of geodesic paths that connect the transmitting and receiving antenna and ℓ_e is the electrical length of the receiving antenna assuming perfect match given by:

$$\ell_e = \sqrt{\frac{G_{\text{R}} \lambda_0^2 R_{\text{ant}}}{\pi \eta_0}} e^{j\angle E_{\text{R}}} \quad (3.6)$$

where λ_0 is the free space wave length and R_{ant} is the resistive part of the antenna impedance. The received power can be calculated as:

$$P_{\text{R}} = \frac{|V_{\text{OC}}|^2}{8R_{\text{ant}}} \quad (3.7)$$

By combining Equations 3.4, 3.5 and 3.7 the E2E path gain can be found:

$$\frac{P_{\text{R}}}{P_{\text{T}}} = \left(\frac{\lambda_0}{4\pi}\right)^2 \left| \sum_{i=1}^N \sqrt{G_{\text{R},i} G_{\text{T},i}} \frac{d\psi_{0,i}}{d\chi_i} L_i A_i e^{j(\angle E_{\text{R},i} + \angle E_{\text{T},i}) - jk_0 t_i - \int_0^{t_i} \alpha_i dt} \right|^2 \quad (3.8)$$

This result is valid for any on-body connection as long as the contribution going through the body is negligible and the path of each of the geodesic paths is convex.

3.3 Simulation and Numerical Implementation

The model was applied to the modified Specific Anthropomorphic Mannequin (SAM) head which is available in Ansys HFSS. The ears have been added. They originate from real ear impressions made within the company originally for acoustic purposes. The SAM head and the added ears are seen in Figure 3.1. The antenna seen in the ear is presented in Chapter 4. The antenna is used here for the validation. The head was ascribed homogeneous constitutive parameters of $\epsilon_r = 39.2$ and $\sigma = 1.8 \text{ S/m}$ as given in Table 2.1. Reference simulations were run in Ansys HFSS 18.2 with extremely

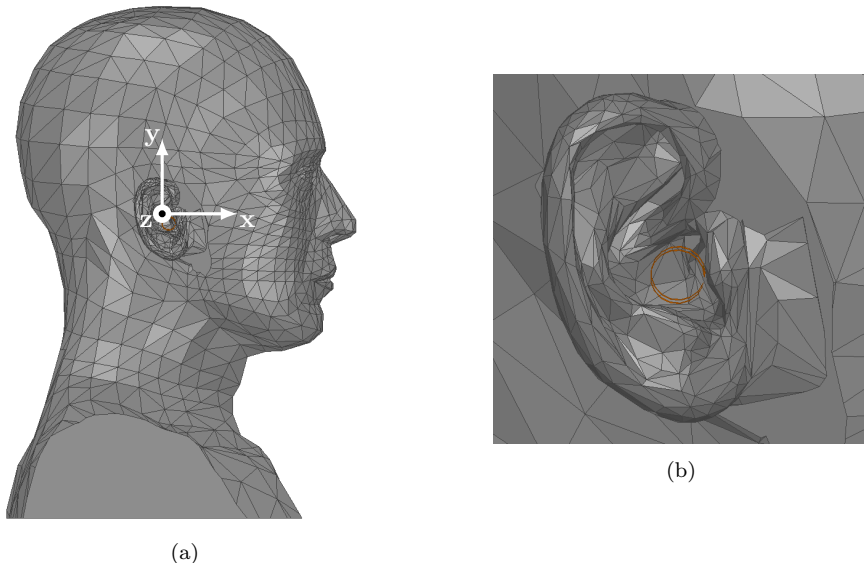


Figure 3.1. The SAM phantom head (a) with the coordinate system used and a close up of the realistic ear (b) where the antenna can be seen.

strict convergence criteria of 0.1 dB change of the maximum achievable path gain (MAPG). This is equivalent to a 2.27% change. The MAPG $|S_{21}^{\max}|$ is obtained when both antennas are perfectly matched. It can be calculated using [43]. Since the path gain $|S_{21}|$ is very low, the antenna matching on one side has a negligible impact on the antenna impedance on the other side. Therefore, the MAPG $|S_{21}^{\max}|$ can be approximated by Eq. 3.9, i.e.,

$$|S_{21}^{\max}| \approx \frac{|S_{21}|^2}{(1 - |S_{11}|^2)(1 - |S_{22}|^2)}. \quad (3.9)$$

Furthermore, a convergence criterion of absolute change of 0.02 on the reflection coefficients is also applied.

To ensure that no unforeseen paths contribute to the path gain, the neck and top of the shoulders have been included. Otherwise, energy creeping around the bottom of the head could be a significant contribution. The importance of the inclusion of the neck and the pinna is investigated in [44]. Furthermore, a simulation was run with absorbers around the entire head to see the path gain contribution through the head. This contribution is clearly ignored in the model. The simulation show a $|S_{21}^{\max}|$ of -103.6 dB which is well below the -78.3 dB of the equivalent simulation without absorbers. Depending on the phase, the energy through the head will add or subtract to the total path gain. This will result in a variation of ± 0.5 dB.

The faceted version of the SAM head is used since it simplifies the mesh for the simulations. At the same time it makes it relatively easy to find the geodesic paths between the ears. The ears were removed since the effect of the pinna is included in the simulated gain that were used for the model. On the facets the geodesics are just straight lines. In the transition from one facet to the next, the angle with the

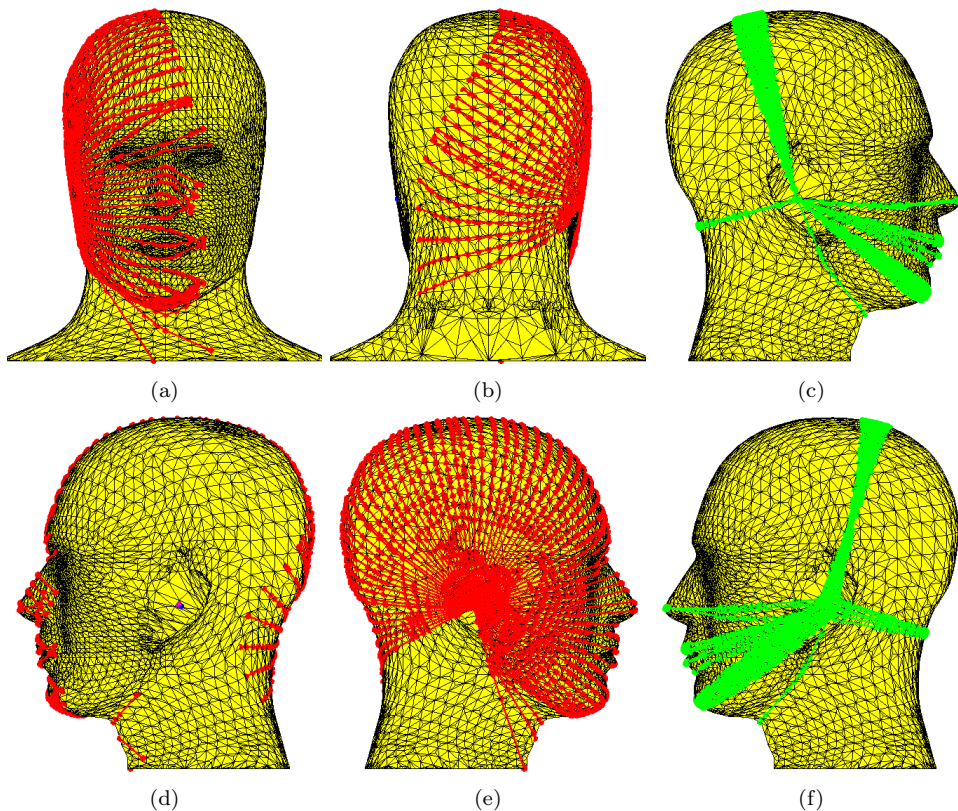


Figure 3.2. The SAM phantom head with the geodesic path originating from the position of the right ear are seen in red (a, b, d, e). The lines end after 200 mm. The SAM phantom head geodesic lines that are emitted from the right ear and reaches the left ear are seen in green (c, f). The lines that comes within 10 mm of the left antenna position are shown.

edge that is crossed needs to stay constant. Due to the facets, the geodesic lines may not distribute as they otherwise would. Therefore, the head used to find the geodesic lines has been up-sampled. The head with the geodesics is seen in Figure 3.2. It is clearly seen that the geodesics form a wavefront. Around the back of the head it is completely uniform. Around the front the different features of the face make it less uniform, but the wavefront is still clear. The electric fields on the surface of the head obtained from the simulation is seen in Figure 3.3. Here the same wavefronts are clearly visible. This confirms the fundamental approach of the model. The green lines in Figure 3.2c and Figure 3.2f show which geodesic lines that reach the opposite ear. There is a clear single path around the back and over the top of the head. Around the front there are four paths, with the main one around the chin and minor ones around the nose, mouth and the transition from the neck to the head.

As mentioned, a few areas of the head are concave. The concave areas are found in the front of the head, especially at the nose. In the implementation the geodesic lines are found as straight lines across these concave areas. Diffraction and free space propagation could be used for these areas, but to reduce the complexity, and

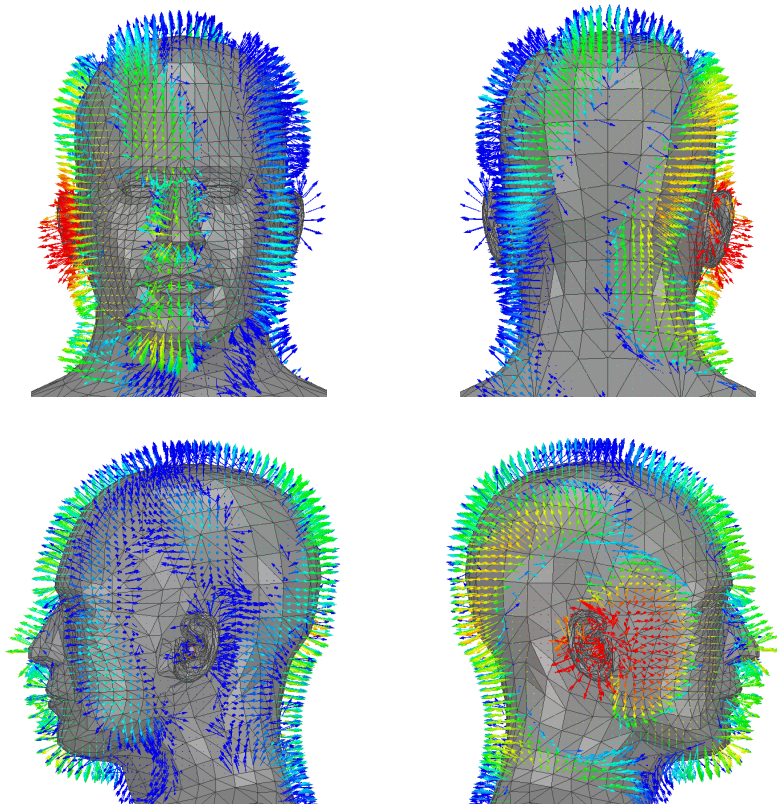


Figure 3.3. The SAM phantom head with the electric field right above the surface plotted as vectors. The color scale ranges from 50 V/m (red) to 0.5 V/m (blue).

assuming low impact on the total path gain, this was not done. Instead, the straight lines were simply included in the geodesic paths, and the propagation calculated as if the propagation was on the surface of the head.

The geodesic paths are each approximated by 100 points uniformly distributed along the path. The torsion and curvature is calculated from a smoothed version of the lines to avoid the non-differentiable nature of the paths over the facets. The attenuation given by (2.14) is calculated for each of the 100 points. The total attenuation along the path is found through integration of the 100 points by the use of the trapezoidal method.

Finally, the derivative, $\frac{d\psi_0}{d\chi}$, from (2.33) has to be found. The faceting of the head makes the derivative hard to find. Therefore, the derivative for each of the six paths have been approximated as:

$$\frac{d\psi_0}{d\chi} = \sqrt{\frac{\Delta\psi_0 n_{\text{lim}}}{2\chi_{\text{lim}}}} \quad (3.10)$$

where $\Delta\psi_0 = 0.25^\circ$ is the discrete angle between adjacent lines at the source and n_{lim} is the number of lines for a given path that get within a certain distance, $\chi_{\text{lim}} = 10$ mm

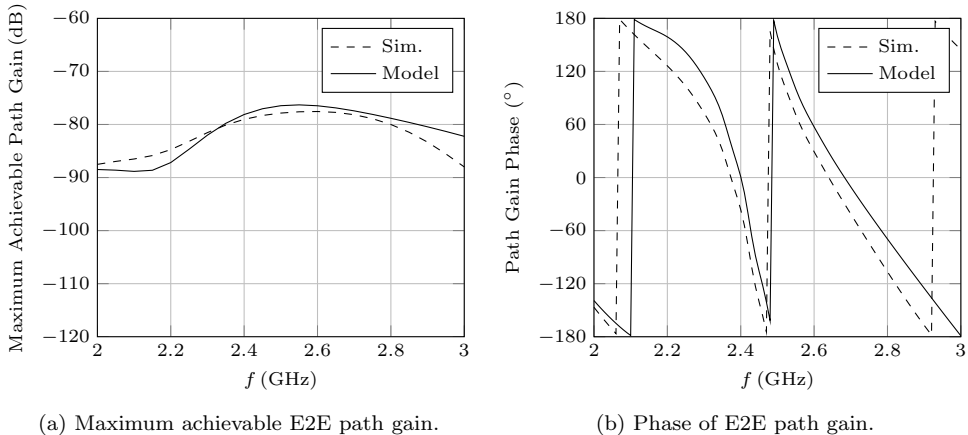


Figure 3.4. Simulated (dashed line) and modeled (solid line) maximum achievable E2E path gain (a) and phase of E2E path gain (b).

of the observation point.

3.4 Validation

To validate the model, several different simulations have been performed to compare with the model. The simulation model is validated against measurements around 2.45 GHz in Chapter 4. To compare the path gains without the windowing effect of the reflection, the MAPG is used. To further compare the path gains without the windowing effect of the radiation efficiency of the antennas, a propagation gain is introduced. The propagation gain is given as the maximum achievable path gain divided by the efficiency twice. A frequency sweep around the 2.45 GHz ISM band is performed. Thereafter the antenna is rotated in the ear. A frequency sweep around the 5.8 GHz ISM band is also done. Finally, a comparison is done between the use of a small ear cut-out and the entire head as input for the gain in the model.

3.4.1 Frequency Sweep at 2.45 GHz

The simulated and modeled results for the MAPG and the phase of the E2E path gain are seen in Figure 3.4. The overall trend of the frequency response is the same for the MAPG as well as the phase. The model is within a few dBs for most of the simulation's frequency range. It is noted that at the edges of the simulation's frequency range, the path gain is significantly below -100 dB. Even though the convergence criteria are very strict, the levels are so low that the simulation results might be a bit less accurate at these levels. In Figure 3.5 the propagation gain is shown. It is seen that even with the windowing effect of the radiation efficiency removed, the simulation and model are in agreement. The propagation gain is decreasing with respect to the frequency, but clearly some interference between different paths happens at different frequencies. The propagation gain at some frequencies drops quickly and at others it even increases. The trend of this is correct in the model. Therefore, to investigate

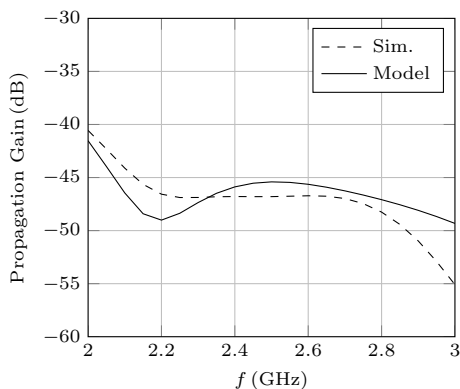


Figure 3.5. Simulated (dashed line) and modeled (solid line) E2E propagation gain.

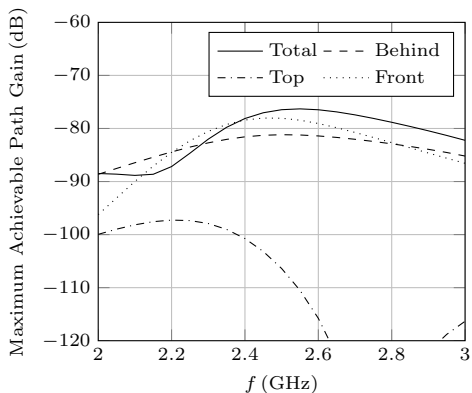
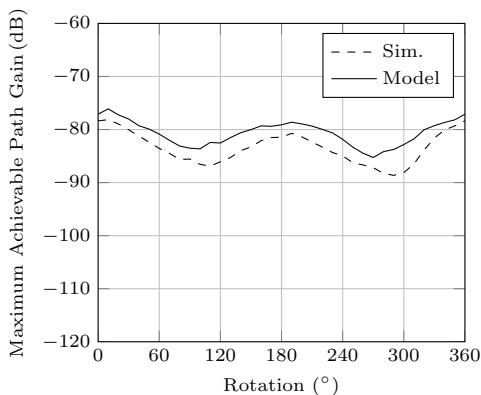
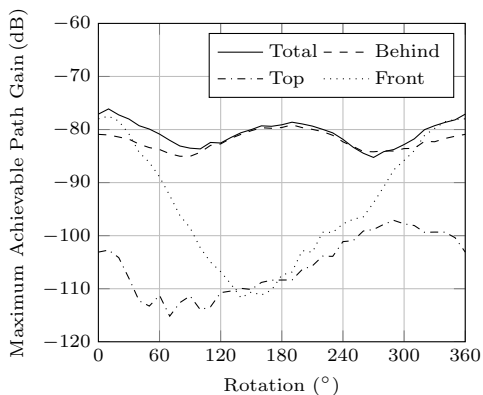


Figure 3.6. Modeled E2E maximum achievable path gain divided into different paths. Total (solid), behind the head (dashed), over the top of the head (dash-dotted), and around the front of the head (dotted).



(a) Simulated (dashed line) and modeled (solid line).



(b) Modeled MAPG divided into different paths. Total (solid), behind the head (dashed), over the top of the head (dash-dotted), and around the front of the head (dotted).

Figure 3.7. E2E maximum achievable path gain for different angles of rotation of the antenna. Simulated and modeled in (a). By path in (b).

what interference that is going on, the MAPG is shown for the three main paths (behind, top, and front) in Figure 3.6. It is seen that the top path is insignificant. The path behind and in front of the head are of similar magnitude, but it is seen that at different frequencies they add or subtract. At 2.2 GHz it is seen that the back and front path's MAPGs are both larger than the total MAPG. At 2.8 GHz they are both more than 3 dB lower than the total MAPG. This confirms the model's ability to predict the magnitude and phase of the individual paths, precise enough for the sum to give the correct total path gain.

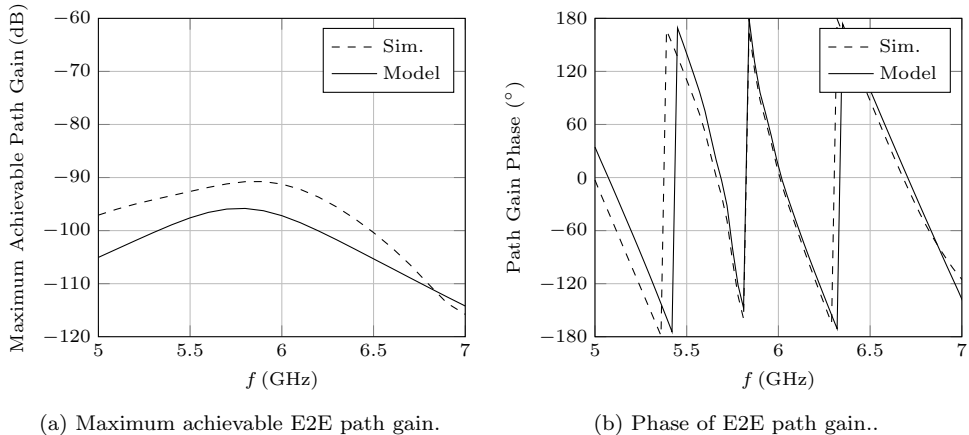


Figure 3.8. Simulated (dashed line) and modeled (solid line) maximum achievable E2E path gain (a) and phase of E2E path gain (b).

3.4.2 Rotation of Antenna

The antenna was rotated in the ear in steps of 10° . The experiment is described in detail and with measurement results in Section 4.3.1 and illustrated in Figure 4.8. The simulated and modeled MAPG is seen in Figure 3.7a. It is seen that the simulated and modeled results show similar trends although the model seems to be a few dBs higher for all positions. In Figure 3.7b the modeled MAPG has been divided into the different paths. Again the contribution from the top path is insignificant for all positions. The front path is seen to be dominant for positions close to 0° . At positions around 180° the front path is insignificant. The dominant path for these positions is the path behind the head. This demonstrates that the model captures effect from transitioning between different dominant paths.

3.4.3 Frequency Sweep at 5.8 GHz

The antenna was scaled by the ratio of 2.45 GHz and 5.8 GHz to make it resonant at 5.8 GHz. The constitutive parameters of the head was changed to the values for 5.8 GHz. A frequency sweep between 5 GHz and 7 GHz was simulated and modeled. No measurements on prototypes have been performed at these frequencies and the simulations are therefore not as trusted as those for the 2.45 GHz range. Still the results are included to show the model is also valid at other frequencies. In Figure 3.8 the simulated and modeled results are shown. It is seen that the MAPG is much lower for this frequency range, which would make it harder to implement. The model is seen to predict the trend correctly at this frequency range as well. However, the error in the magnitude of the MAPG is a bit higher. The phase is seen to be modeled correctly as well. This also shows the validity of the model at other frequencies. It is important to remember that the head still needs to be opaque and large with respect to the wavelength. At 2.45 GHz this is valid, but on the limit. At higher frequencies the requirements are fulfilled, but at lower frequencies the model will break down.

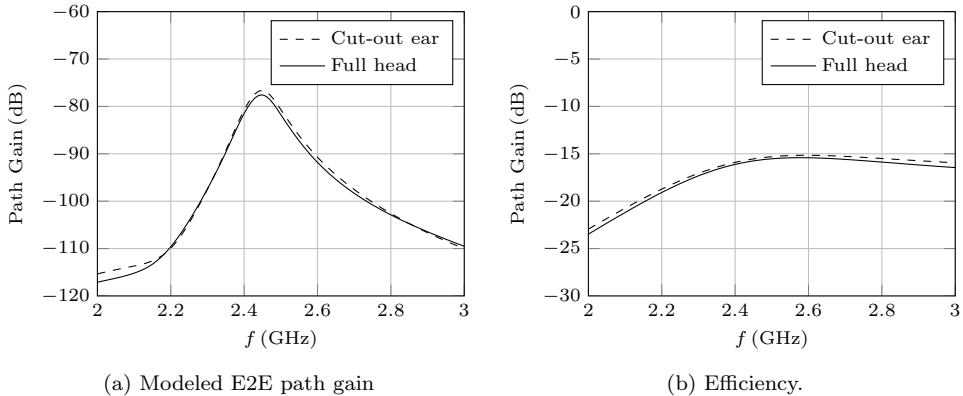


Figure 3.9. E2E path gain (a) and efficiency (b) based on simulation of cut-out ear block (dashed line) and full head (solid line).

3.4.4 Ear Cut-out Comparison

The full head simulation is heavy to run. If for example two full HIs are put into the ears, the simulation will be almost impossible to run with readily available computer software and hardware. To apply the model, the only data needed is the antenna gain in the XY-plane in the coordinate system shown in Figure 3.1. The gain is mainly affected by the human tissue close to the antenna. Therefore, a small square box cut-out only containing the ear and a small part of the head was made. The size corresponds to the part visible in Figure 3.1b. A simulation with a frequency sweep between 2 GHz and 3 GHz was done to compare it with the full head simulation. A study of the effect of the pinna on the radiation pattern is found in [45]. The modeled path gain when using the cut-out ear box and the full head simulation is shown in Figure 3.9a. The path gains are within 1 dB of each other for the entire band except at around 2 GHz where the difference is up to 2 dB. The efficiencies in the two cases are compared in Figure 3.9b. It is seen that it is the same curve displaced with less than 0.5 dB. These simulations demonstrate that the cut-out box is possible to use instead of the full head simulation. This makes it possible to achieve a significantly faster simulation, and by use of the model still obtain the E2E path gain.

3.5 Propagation Gain by Path

To compare the different paths around the head independent of the antenna gain, the E2E propagation gain by path of a unity gain antenna was calculated. The results are shown in Figure 3.10. It is seen that the path around the front of the head is the strongest one, but not much different from the path behind the head. The top path is the weakest, as also seen when the antenna radiation pattern is included. If one had the possibility of using a directive antenna, the direction to prefer would be the front. This is seen to be the opposite conclusion than that for behind-the-ear devices found in [1, 9]. This is most likely caused by the in-the-ear placement that makes the path length longer around the back and shorter around the front compared to the behind-

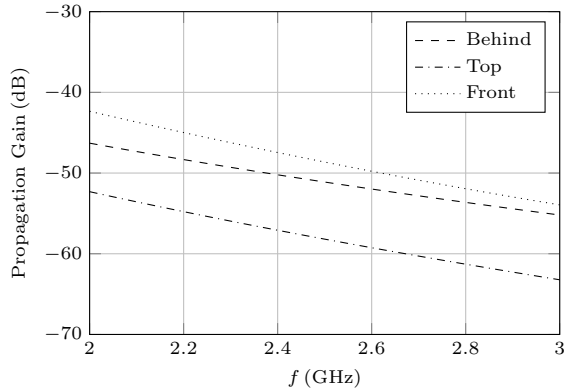


Figure 3.10. Modeled E2E propagation gain divided into different paths. Behind the head (dashed), over the top of the head (dash-dotted), and around the front of the head (dotted).

the-ear placement. The level of approximately -50 dB at 2.45 GHz is similar to BTE devices. It is noted that one could potentially obtain an even better propagation gain by transmitting energy through multiple paths around the head and ensuring that the energy interferes constructively at the opposite site of the head. This solution would of course be very sensitive to head size variations. In general, there is a high risk of interference between the front and back path due to their similar path gains. A study of the variation is found in [46]. Here it is also confirmed that the path gain for ITE devices is harder to predict than for the BTE devices due to the stronger front path.

3.6 Summary

In this chapter a new E2E propagation model has been presented. The model is the first to use geometrical theory of diffraction expression for dielectric materials. It is also the first model to investigate and use the geodesic paths around the head. The model uses the far-field radiation pattern of the antenna in the ear to approximate the energy in each of the geodesic paths. It was found that the model is capable of predicting variations of the path gain over frequency and rotation of the antennas. It was proven that the model can be used with antenna radiation patterns from a small ear cut-out box with only one device instead of the full head simulation with two devices. In this way the model can be used to speed up simulations significantly and enable simulations on complex hearing instruments. Finally, it was found that the path gain is highest around the front of the head, a little less behind the head and low around the top. This shows that depending on the in-ear radiation pattern, there could be a risk of interference between different paths.

ANTENNAS FOR CUSTOM HEARING INSTRUMENTS

A study of antennas for custom HIs is done in this chapter. First, a short survey of the existing antennas is done. Thereafter, a series of antennas are presented. The two antennas that are mostly in focus have been simulated and measured. The model from Chapter 3 is also applied. The simulated, modeled and measured results are compared. Finally, the effect of the placement in the ear is investigated. The chapter is based on the work presented in [P3, P8–P10]. It should be noted that the antenna in [P8] was presented briefly in [47] and unfinished work on the antenna in [P3] was presented as part of [48].

4.1 Survey

In the literature there is only a limited number of publications on antennas for the 2.45 GHz band to be worn at the ears. The most significant work is found in [1], specifically in [49, 50]. This work is focused on the behind-the-ear (BTE) placement. It was shown that the polarization of the antenna should be perpendicular to the surface of the head to optimize the on-body efficiency, as well as the E2E path gain. This can be realized intuitively if the rough approximation of the human body as PEC is assumed. The parallel electric fields will be "short-circuited" whereas the perpendicular electric fields will creep around the head. This corresponds with what was shown in Chapter 2. In [49] a BTE antenna with an E2E path gain of -52 dB was presented.

In [51] two antennas are presented for placement in the ear. One antenna is placed at an outer position. Further simulations on this antenna are presented in [44]. Antennas with similar outer position placement are presented in [52–54]. All these antennas are placed so the outer part of the antenna is at least 10 mm above the surface of the head. At this position the path gains achieved range between -63 dB and -75 dB. This outer positioning of the antenna is not desirable for the aesthetics of modern custom HIs.

The second antenna in [51] and the antenna in [55] are placed at a desirable deeper position. None of these antennas achieve more than -89 dB in E2E path gain. The antennas presented here will be placed at an approximately similar position. Furthermore, the antennas will be constructed in a way that allows them to be incorporated in a HI. The consequences of the placement of the remaining HI electronics will not be analyzed or investigated here. A study of this and the EMC issues with small

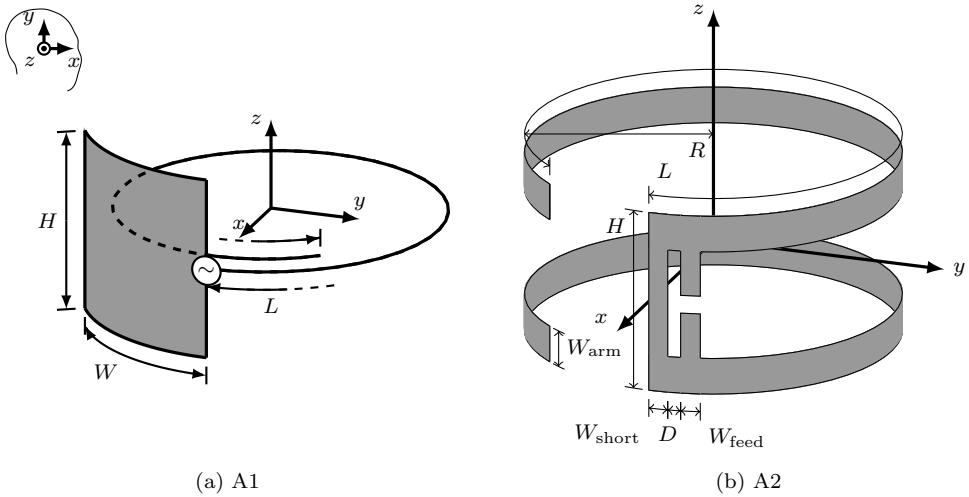


Figure 4.1. The antennas A1 and A2 are shown in (a) and (b), respectively. The orientation of the antenna coordinate system with respect to the head is indicated in the figure.

electronic devices are presented in [56]. Specifically, the impact of the battery is investigated in [57].

4.2 Antennas

The two main antennas presented here are seen in Figure 4.1. These two antennas are presented in full detail in [P3, P8]. The antennas are both of a size so they can fit within a cylinder with a radius of 5 mm and height of 5 mm. They are placed in the ear in such a way that the antenna extends 2.5 mm above and below the surface of the head. Therefore, the xy -plane in Figure 4.1 coincides with the surface of the head. The orientation is indicated by the coordinate system in Figure 4.1 and Figure 3.1. The antennas have been simulated with the same simulation model as in Chapter 3. It is noted that this is a slightly updated version of the simulation model compared to the one used in [P3, P8]. The model from Chapter 3 has been applied to the simulated radiation pattern as well. The antennas have been measured in the ears of a real person. This is done due to the uncertainties from phantom heads described in [58]. The measurements presented here are the median of four measurements, i.e. the third highest path gain of the four. To characterize the antenna fully would require measurements and simulations of a representative part of the world population. This has not been done for this work, but the head used for simulations (SAM) and the head used for the measurements are in top end regarding size. This should give a pessimistic rather than optimistic result. Whether these specific heads have constructive or destructive interference is hard to know. The antennas were fed through coaxial cables connected to a vector network analyzer to measure the E2E path gain. The cables were fitted with quarter wave sleeve baluns to minimize the effect of the cables on the measurements.

The antenna A1 is seen in Figure 4.1a. It is a simple quarter wave monopole with a

ground plane of a similar size of that present in a HI. In free space, the polarization of the antenna is completely parallel to the head. The antenna A2 is seen in Figure 4.1b. It can be seen as a dipole antenna with the arms bent towards each other and with a short circuit attached for tuning purposes. In free space, the polarization of the antenna is completely perpendicular to the surface of the head. Therefore, these two antennas can also help answer whether the polarization affects the efficiency of the antenna and thereby the E2E path gain in a similar way as for BTE devices [50]. The reflection coefficient, E2E path gain, and magnitude and phase of the θ -component of the on-body radiation in the XY-plane are shown for antenna A1 and A2 in Figure 4.2 and Figure 4.3, respectively. It is seen that both antennas are well matched within the entire 2.45 GHz ISM band. The simulated and measured reflection coefficient is similar, with a slightly larger bandwidth for the measurements. The simulated, measured, and modeled E2E path gains for both antennas are seen to agree. The E2E path gain at 2.45 GHz for antenna A1 is -82.9 dB and -82.1 dB simulated and measured, respectively. For antenna A2 it is -78.8 dB and -73.2 dB simulated and measured, respectively. The perpendicular antenna A2 is, as expected from BTE devices, better than the parallel polarized antenna A1. Still, the difference is not as significant as for the BTE devices. The radiation efficiency at 2.45 GHz is -20.8 dB and -15.8 dB for antenna A1 and A2, respectively. This difference is seen to be much more significant than the difference in path gain.

In order to investigate why the path gain difference is not as significant as the radiation efficiency difference, the propagation gain and efficiency over frequency for antenna A1 and A2 are shown in Figure 4.4. It is seen that the propagation gain of antenna A1 is significantly higher than for antenna A2. Furthermore, the propagation gain of A1 is less fluctuating than for A2. This is a sign that there is less interference between the different paths around the head. From the radiation patterns in Figure 4.2c and Figure 4.3c, it is evident that A1 is dominated by a main lobe towards the chin whereas A2 has two almost equally strong lobes. This explains the higher propagation gain of A1 since the radiation pattern indicates less interference and use of the best path as found in Section 3.5. It should be noted that this will probably not be the case for all heads and pinna. In fact it could very well be opposite in some cases.

4.2.1 Modified Monopole

Inspired by the clear efficiency advantage of a perpendicular polarization, a small modification of antenna A1 was made. The new antenna A3 is seen in Figure 4.5. The only difference from A1 is that the spiral monopole arm has been moved from the middle of the ground plane to the top corner. In that way the currents on the ground plane will be diagonal and the antenna will be partially perpendicularly polarized. No prototype has been made, but simulated and modeled results have been found. In Figure 4.6a the simulated and modeled E2E path gains are compared. The improvement in path gain at 2.45 GHz is 5.9 dB and 5.7 dB simulated and modeled, respectively. In Figure 4.6b the radiation efficiencies are compared. The radiation efficiency of A3 at 2.45 GHz is -17.5 dB. This is 3.3 dB better than A1. This corresponds to approximately half the improvement in path gain which shows that the propagation gain and thereby the radiation pattern remains the same. Antenna A3

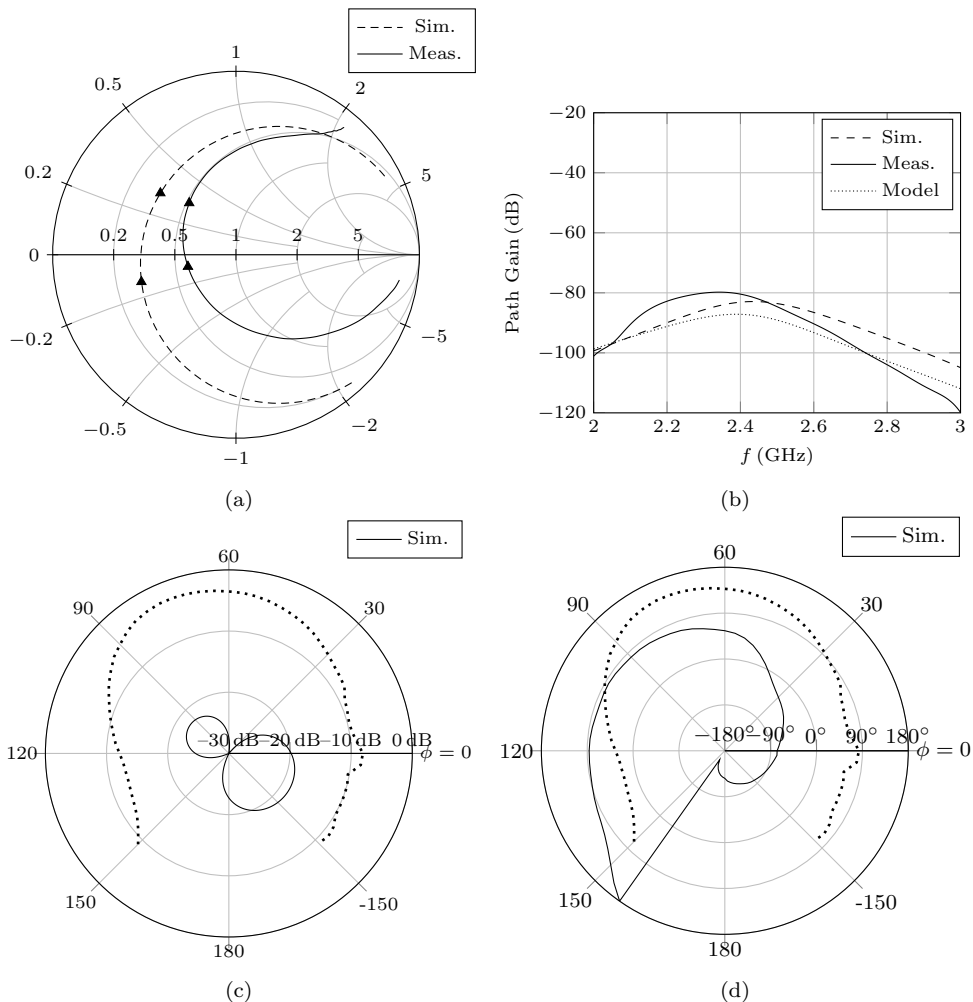


Figure 4.2. Measured and simulated results for A1. The input impedance from 2–3 GHz is shown in (a) with the ISM band marked with triangles, and the ear-to-ear path gain is shown in (b). The simulated gain and phase of the θ -component of the on-body radiation pattern in the XY-plane at 2.45 GHz is displayed in (c) and (d), respectively. The orientation of the SAM head is indicated in the dotted outline. The simulated radiation efficiency is -20.8 dB at 2.45 GHz.

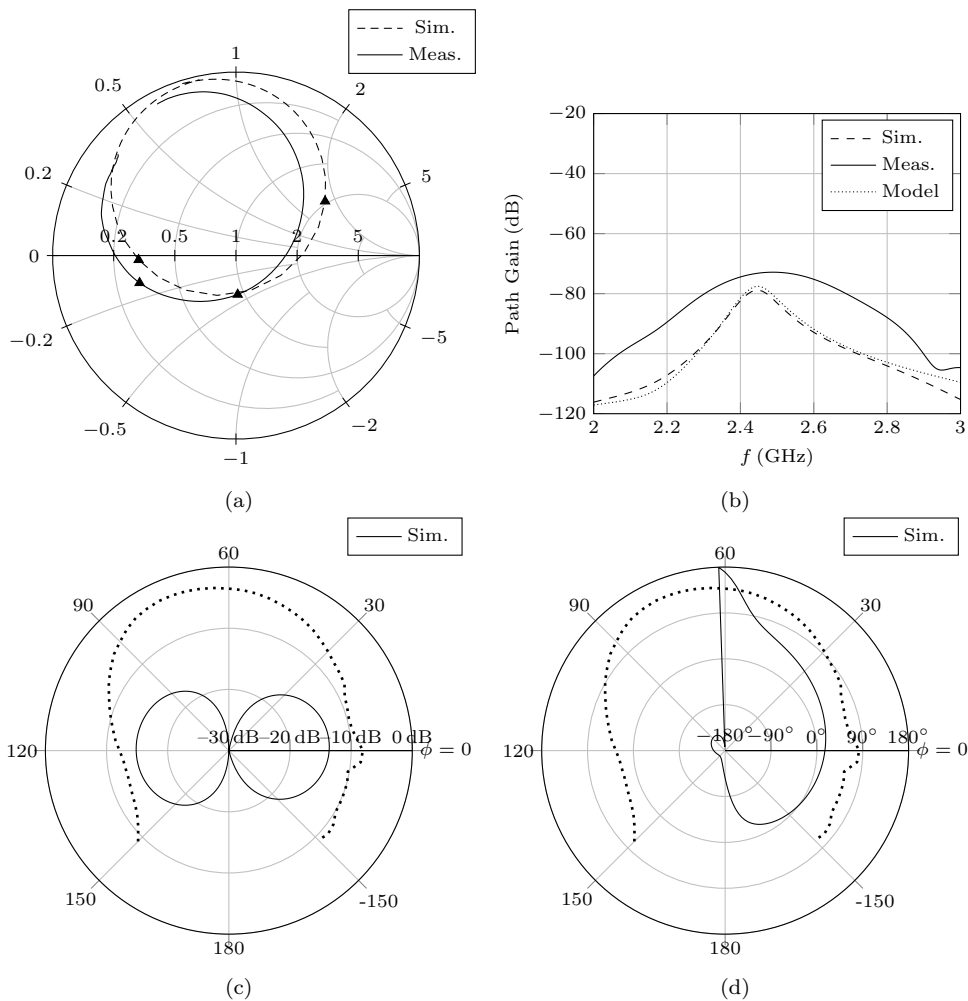
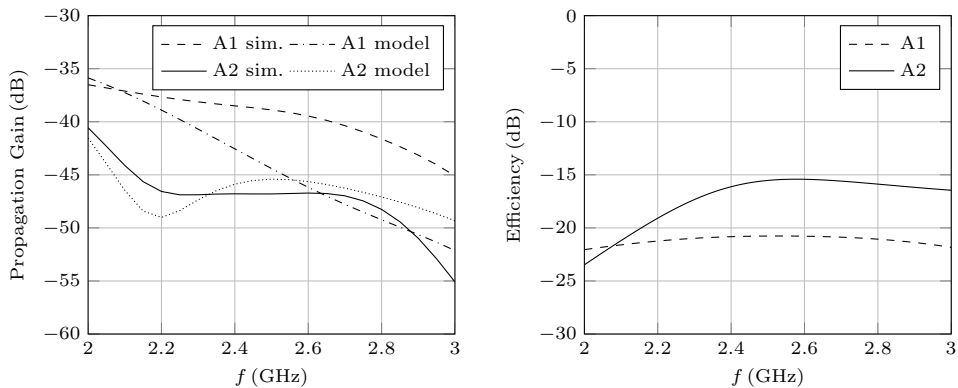


Figure 4.3. Measured and simulated results for A2. The input impedance from 2–3 GHz is shown in (a) with the ISM band marked with triangles, and the ear-to-ear path gain is shown in (b). The simulated gain and phase of the θ -component of the on-body radiation pattern in the XY-plane at 2.45 GHz is displayed in (c) and (d), respectively. The orientation of the SAM head is indicated in the dotted outline. The simulated radiation efficiency is -15.8 dB at 2.45 GHz.



(a) Simulated and modeled E2E propagation gain for antenna A1 and A2. (b) Simulated efficiency for antenna A1 (dashed line) and A2 (solid line).

Figure 4.4. Simulated and modeled results from antenna A1 and A2.

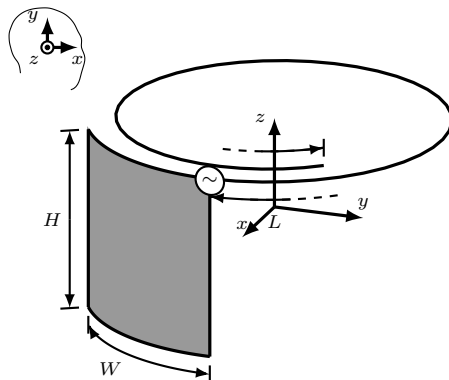


Figure 4.5. Antenna A3. It is a modified version of A1 with the spiral monopole arm moved to the top corner of the ground plane.

is seen to have a slightly higher E2E path gain than A2 even though the efficiency is a little lower. This small modification shows that the importance of the polarization in the ITE position is similar to the BTE position.

4.2.2 Vertically Polarized Slot Antenna

A small experiment with a low profile antenna with a perpendicular polarization has been attempted in [P10]. The design is based on the work in [59] where an electric loop PCB antenna with a uniform current distribution was presented. The uniform current distribution was desired to keep the radiation pattern of a short loop antenna. The current was kept uniform by small capacitive gaps in the loop. Based on Babinet's principle with Booker's extension as found in [60] the antenna was transformed into a magnetic loop antenna. This was done by interchanging the areas with copper and without copper. The antenna, now a slot loop, is seen in Figure 4.7. The radiation

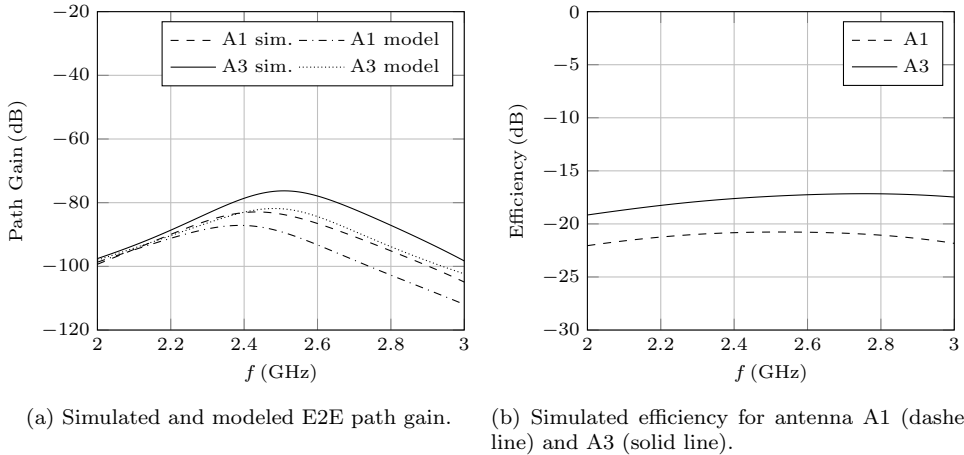


Figure 4.6. Simulated and modeled results from antenna A1 and the modified version A3.

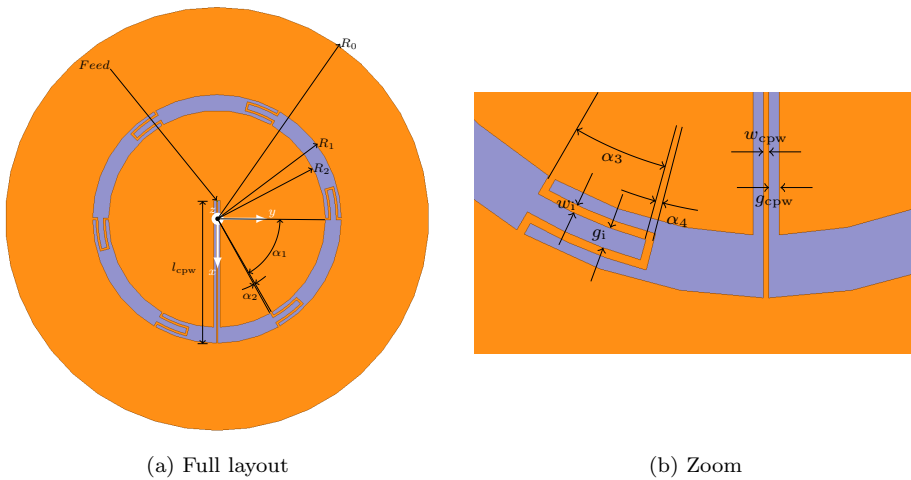


Figure 4.7. Layout of the vertically polarized slot antenna presented in [P10].

pattern achieved was that of a magnetic loop with a uniform current distribution. The dual of that is a short electric dipole perpendicular to it. In this way, the desired polarization perpendicular to the surface of the head was achieved with a low profile antenna. However, the truncation of the ground plane causes a null in the plane of the antenna. A prototype was built that confirmed the performance. The antenna had a radius of 40 mm, which is not feasible for use in a HI. Simulation attempts to reduce the size and maintain the same effect was achieved, but the Q becomes extremely high as well as the dielectric losses in the substrate due to high electric fields in the slot. This makes the antenna useless due to high Q even though it has very low efficiency. The high Q is well explained in [61–63]. The very low extent of the antenna in the direction of polarization is the cause. Basically, it is hard to get

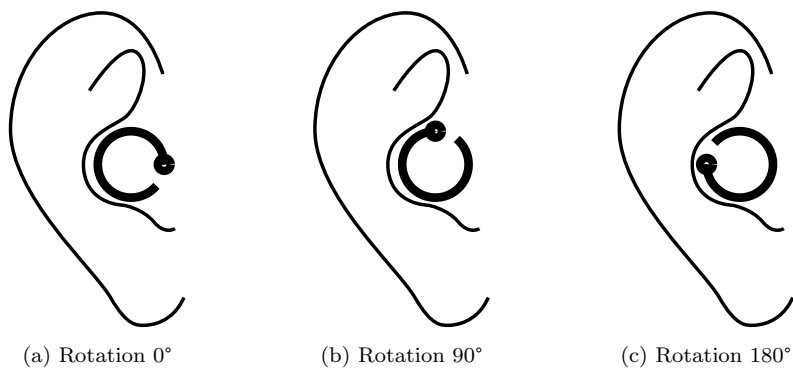


Figure 4.8. The antenna A2 in the concha is rotated counter clockwise in steps of 10° and 30° in the simulation and measurement, respectively.

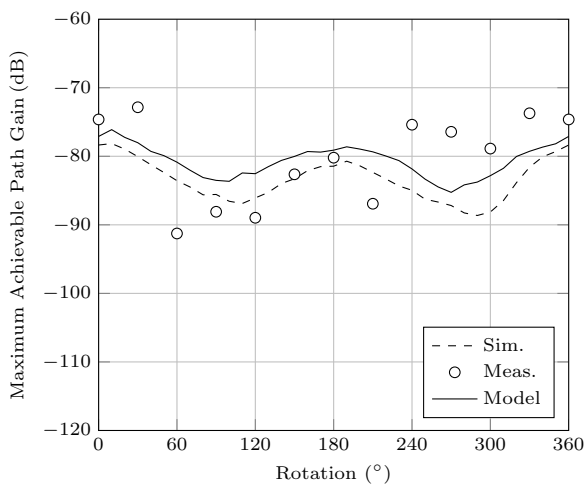


Figure 4.9. Simulated (dashed line), measured (dotted) and modeled (solid line) E2E maximum achievable path gain for different angles of rotation of the antenna A2 at 2.45 GHz.

any separation of electric charge in the direction of the polarization. This proves the necessity of an antenna with an extent in the direction perpendicular to the head.

4.3 Placement

The effect of the placement in the ear of the antenna has been investigated. The experiments have been done on the antenna A2. The antenna was rotated in the ear and the antenna was moved further in and out of the ear.

4.3.1 Rotation

The antenna A2 was rotated in steps of 10° in simulations and in steps of 30° in measurements. All of this was done at 2.45 GHz. The rotation is illustrated in Figure 4.8.

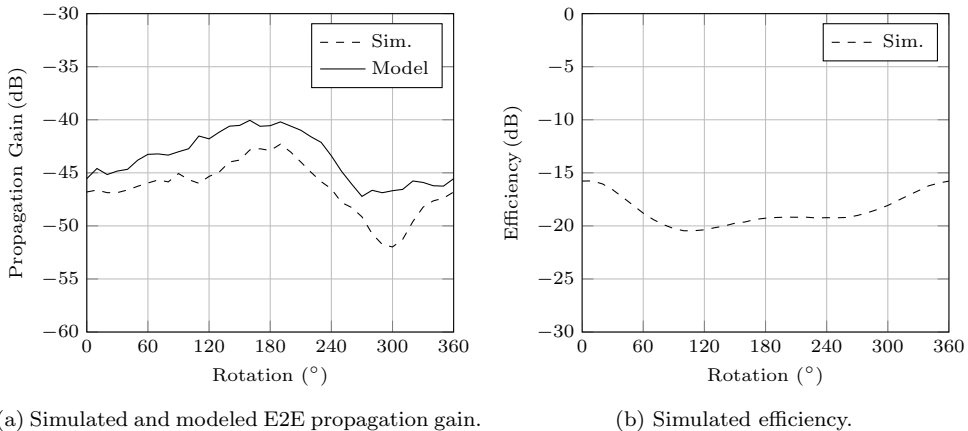


Figure 4.10. Simulated and modeled results from rotation of antenna A2 in the ear at 2.45 GHz.

The results are based on the work done in [P9], but with updated simulations based on the simulation method presented in Section 3.3. Modeled results were added as well. The maximum achievable path gain (MAPG) is seen in Figure 4.9. The simulation, measurement and model all predict 10 dB or more variation as a consequence of the rotation. The simulation and model are similar with a small absolute difference. The measurements are a bit different, which can be expected since the measurements and simulation are not utilizing the same pinna or head.

To investigate the cause of the variation, the MAPG is divided into the propagation gain and the efficiency, as shown in Figure 4.10. It is seen that the propagation gain varies with a little less than the MAPG, but still close to 10 dB. The high and low propagation gain is even so not at the same rotation as the MAPG. A split into different paths around the head is seen in Figure 3.7b. It is clear that different paths are used for different rotational positions, and that interference between the paths occur as well. The efficiency is varying with around 5 dB dependent on the rotation. This corresponds to a 10 dB change in MAPG. The change as a function of rotation is similar to that of the MAPG, but the total effect is not seen without including the propagation gain. The change in efficiency is most likely explained by the positioning of the open end of the antenna. At the open end, the electric fields are highest. The low efficiency at approximately 100° and 250° corresponds to the open end close to the tragus and anti-tragus, respectively. The close proximity of the tragus or anti-tragus at the point of high electric fields causes high dielectric near-field losses in the human tissue. The conclusion is that the rotation affects the efficiency as well as the propagation gain. The exact consequences of rotation is hard to predict and in an actual product the full impact can not be analyzed without simulation and measurements on several individuals.

4.3.2 Depth in Ear

The effect of the placement depth in the ear was investigated by moving the antenna A2 in steps of 1 mm from a position 1 mm deeper than the reference position to 3 mm

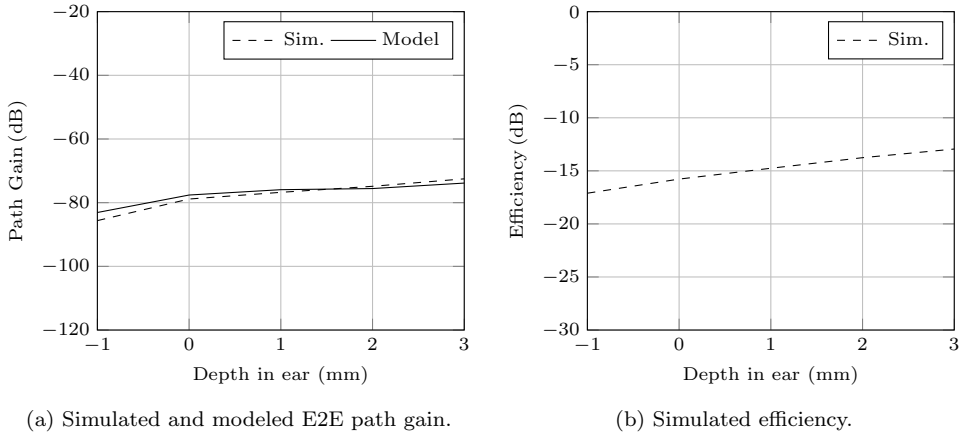


Figure 4.11. Simulated and modeled results for different placements of antenna A2. The antenna was moved from 1 mm deeper to 3 mm further out than the reference position in steps of 1 mm.

further out. The simulated and modeled E2E path gain is seen in Figure 4.11a. The simulated efficiency is shown in Figure 4.11b. It is clear that even a small move in the perpendicular direction has major impact on the E2E path gain. The effect by a 4 mm move is more than 10 dB. The change in efficiency is a little more than 5 dB and explains the change in path gain. This demonstrates that the change by a move in the depth in the ear canal is more easily understood and mostly caused by efficiency change. As a rule of thumb the efficiency will drop with one to two decibels per millimeter the antenna is moved into the ear canal. The change in E2E path gain will be twice of that. This demonstrates the challenges in designing well working small deep in the ear HI with a stable connection at 2.45 GHz.

4.4 Summary

In this chapter multiple different ITE antennas for HIs were presented. The antennas are the first to demonstrate an E2E path gain above -80 dB for antennas placed in a realistic position for use in small ITE HIs. A modification of one of the antennas demonstrated the importance of polarization perpendicular to the surface of the head. An antenna designed with the correct polarization, but with almost no extent in the direction perpendicular to the head, demonstrated that this can be achieved, but not with feasible efficiency and Q. Finally, the impact of the placement of the antenna was investigated. It was shown that a rotation of the antenna changes the radiation efficiency as well as the radiation pattern. These two factors change the E2E path gain in a way that is not easy to predict. But design care should be taken to minimize the electric fields close to the human skin, for example the tragus and anti-tragus. The impact of the placement depth in the ear was investigated as well. It was found that the depth primarily changes the radiation efficiency and thus affects the E2E path gain through this change. A rule of thumb is that the efficiency is reduced by 1-2 dB per millimeter the antenna is moved into the ear. The impact on the E2E path gain is approximately double of that.

CONCLUSIONS

Wireless communication for custom hearing instruments has been studied. The theoretical understanding of on-body propagation has been increased. The ear-to-ear (E2E) propagation channel has been investigated and a model proposed. Several antenna concepts for custom HIs have been suggested. Based on these concepts, different learnings for future antenna designs have been drawn.

First, the theoretical models for on-body propagation were investigated. The models in the literature agree that at 2.45 GHz the on-body propagation happens around and not through the body. Many models are seen to use the geometrical theory of diffraction (GTD) or uniform GTD (UTD). It was found that many of the models are based on the assumption that the human body can be modeled as a perfect electric conductor. This was proven to be an invalid assumption, especially in cases where the geodesic paths, that the energy follows, are not torsionless. In order to enable the use of GTD in the modeling of the on-body propagation without the use of this assumption, a new GTD formulation was found. The new GTD formulation thus models the human body as a lossy dielectric. The GTD formulation was developed through two canonical problems. The eigenfunction solutions for these were found and asymptotically expanded to yield the GTD solution. This was generalized to all convex geometries. The model was validated by comparison with the eigenfunction solution. It was found to be valid for opaque geometries down to a size $\frac{\kappa}{\kappa^2 + \tau^2} > \lambda/2$ and up to a limited torsion of $\tau/\kappa < 2$.

Secondly, the specific E2E propagation was studied. The existing models were investigated. The models often use the the PEC GTD approximation to simplified geometries such as an elliptical cylinder. By the use of the new GTD formulation, a new E2E propagation model was found. The model is the first to find the geodesic paths around the head. Thereby, it is the first to answer the essential question of which paths connect the ears on opposite sides of the head. Three paths exist; behind the head, over the top, and around the front of the head. The model was applied to a specific head, which was also simulated. The results were compared to validate the model, which was found to be capable of predicting both magnitude and phase of the E2E path gain. Even with the windowing effect of the matching and efficiency of the antenna, the model predicts the same trends over frequency and placement as the simulations. Excluding the effect of the antenna and the pinna it was found that, for a placement in the ear, the path around the front of the head has the lowest loss.

Thirdly, a number of antennas for custom HIs were presented. Based on a literature study it was found that there is a need for antennas for small size cosmetically

appealing custom HIs. From research on behind-the-ear (BTE) devices it was decided to investigate the impact of polarization. From two similarly sized antennas with opposite polarization, it was found that a perpendicular polarization with respect to the surface of the human head results in a significantly more efficient antenna. An E2E path gain of more than -80 dB for the entire 2.45 GHz ISM band was achieved. With the use of the developed E2E propagation model, it was observed and analyzed how the radiation pattern of the antenna affects the E2E path gain almost as significantly as the efficiency. It was also shown how a minor change of the parallel polarized antenna could improve the efficiency significantly. The option of an antenna placed in the same plane as the surface of the head, with a perpendicular polarization, was investigated. It was seen to be possible, but not feasible due to high Q and high losses. The antenna needs to have an extent in the direction perpendicular to the head. Finally, the placement of the antenna was investigated. It was seen that rotation changes the radiation efficiency significantly due to different near-field loss. The radiation pattern is impacted, as well which results in equally significant changes in the E2E path gain. In total, a change of more than 10 dB was observed due to rotation. The placement depth in the ear was investigated. It was seen that the radiation efficiency reduces with one to two decibels per millimeter the antenna is moved deeper into the ear. This demonstrates the importance of the antenna placement.

Future work could include studies of different heads and ears on the E2E path gain. The impact from different ears on the radiation efficiency and from different heads on the propagation gain would be relevant to categorize. Such a study using a large population would help predict the performance of different antennas across the full group of users. A possibility would be to use 3D scans of actual people to put into simulations and the model. A study of the propagation channel between the front or back pocket to the ear would be relevant. The requirements for this pocket-to-ear (P2E) channel are strict, since full audio signals are to be transmitted. The model presented here could also be applied to the P2E channel. Studies of possibly directional antennas could be relevant. For the 2.45 GHz ISM band the only option is probably a Huygens source, as also suggested elsewhere. If higher frequency bands were to be used, for example the 5.8 GHz ISM band, the possible impact of directional antennas to compensate for higher creeping loss could be investigated.

Finally, it is the hope that this work can be a help to antenna design for in-the-ear hearing instruments and devices in general. Hopefully, it can serve as an inspiration for future studies in different aspects of the wireless communication for custom hearing instruments.

BIBLIOGRAPHY

- [1] S. H. Kvist, “Antennas and propagation for body-centric wireless communications”, PhD thesis, Technical University of Denmark (DTU), Kgs. Lyngby, Denmark, 2013.
- [2] P. S. Hall and Y. Hao, Eds., *Antennas and Propagation for Body-Centric Wireless Communications*. Norwood, MA, USA: Artech House, 2006.
- [3] *IEEE recommended practice for determining the peak spatial-average specific absorption rate (SAR) in the human head from wireless communications devices: Measurement techniques*, 2013.
- [4] J. Ryckaert, P. De Doncker, R. Meys, A. de Le Hoye, and S. Donnay, “Channel Model for Wireless Communication Around Human Body”, *Electronics Letters*, vol. 40, no. 9, pp. 543–544, Apr. 2004.
- [5] G. A. Conway and W. G. Scanlon, “Antennas for Over-Body-Surface Communication at 2.45 GHz”, *IEEE Trans. Antennas Propagat.*, vol. 57, no. 4, Part 1, pp. 844–855, Apr. 2009.
- [6] P. S. Hall, Y. Hao, Y. I. Nechayev, *et al.*, “Antennas and Propagation for On-Body Communication Systems”, *IEEE Antennas Propag. Mag.*, vol. 49, no. 3, pp. 41–58, Jun. 2007.
- [7] R. Chandra and A. J. Johansson, “A link loss model for the on-body propagation channel for binaural hearing aids”, *IEEE Trans. Antennas Propagat.*, vol. 61, no. 12, pp. 6180–6190, 2013.
- [8] E. Plouhinec, B. Uguen, M. Mhedhbi, and S. Avrillon, “3D UTD modeling of a measured antenna disturbed by a dielectric circular cylinder in WBAN context”, in *2014 IEEE 79th Vehicular Technology Conference (VTC Spring)*, May 2014, pp. 1–5.
- [9] S. H. Kvist, J. Thaysen, and K. B. Jakobsen, “Ear-to-Ear On-Body Channel Model for Hearing Aid Applications”, *IEEE Transactions on Antennas and Propagation*, vol. 63, no. 1, pp. 344–352, Jan. 2015.
- [10] Y. Hao, A. Alomainy, Y. Zhao, *et al.*, “Statistical and Deterministic Modelling of Radio Propagation Channels in WBAN at 2.45GHz”, in *Antennas and Propagation Society International Symposium 2006, IEEE*, Jul. 2006, pp. 2169–2172.
- [11] Y. Zhao, Y. Hao, A. Alomainy, and C. G. Parini, “UWB On-Body Radio Channel Modeling Using Ray Theory and Subband FDTD Method”, *IEEE Trans. Microwave Theory Tech.*, vol. 54, no. 4, pp. 1827–1835, Apr. 2006.

- [12] R. Chandra and A. J. Johansson, "An Analytical Link-Loss Model for On-Body Propagation Around the Body Based on Elliptical Approximation of the Torso With Arms' Influence Included", *IEEE Antennas Wirel. Propag. Lett.*, vol. 12, pp. 528–531, Apr. 2013.
- [13] M. Ghaddar, L. Talbi, and T. A. Denidni, "Human Body Modelling for Prediction of Effect of People on Indoor Propagation Channel", *Electronics Letters*, vol. 40, no. 25, pp. 1592–1594, Dec. 2004.
- [14] C. Oliveira and L. M. Correia, "A Statistical Model to Characterize User Influence in Body Area Networks", in *Vehicular Technology Conference Fall (VTC 2010-Fall)*, 2010 *IEEE 72nd*, Sep. 2010.
- [15] A. R. Guraliuc, A. A. Serra, P. Nepa, and G. Manara, "Path Gain Models for on-Body Communication Systems at 2.4 and 5.8 GHz", *Annals of Telecommunications*, vol. 66, no. 3-4, pp. 205–212, 2011.
- [16] G. R. Crusats, A. Fort, C. Craeye, and C. Oestges, "Analytical Propagation Models for Body Area Networks", in *Antennas and Propagation for Body-Centric Wireless Communications, 2007 IET Seminar on*, Apr. 2007, pp. 90–96.
- [17] A. Fort, F. Keshmiri, G. R. Crusats, C. Craeye, and C. Oestges, "A Body Area Propagation Model Derived From Fundamental Principles: Analytical Analysis and Comparison With Measurements", *IEEE Trans. Antennas Propagat.*, vol. 58, no. 2, pp. 503–514, Feb. 2010.
- [18] T. Alves, B. Poussot, and J.-M. Laheurte, "Analytical Propagation Modeling of BAN Channels Based on the Creeping-Wave Theory", *IEEE Trans. Antennas Propagat.*, vol. 59, no. 4, pp. 1269–1274, Apr. 2011.
- [19] J. R. Wait, "Scattering of a plane wave from a circular dielectric cylinder at oblique incidence", *Canadian Journal of Physics*, vol. 33, no. 5, pp. 189–195, 1955.
- [20] B. R. Levy and J. B. Keller, "Diffraction by a Smooth Object", *Communications on Pure and Applied Mathematics*, vol. 12, no. 1, pp. 159–209, 1959.
- [21] A. G. Aguilar, P. H. Pathak, and M. Sierra-Perez, "A canonical utd solution for electromagnetic scattering by an electrically large impedance circular cylinder illuminated by an obliquely incident plane wave", *IEEE Transactions on Antennas and Propagation*, vol. 61, no. 10, pp. 5144–5154, 2013.
- [22] R. F. Harrington, *Time-Harmonic Electromagnetic Fields*, 2nd ed. John Wiley & Sons, 2001.
- [23] R. Paknys, "Evaluation of hankel functions with complex argument and complex-order", *IEEE Transactions on Antennas and Propagation*, vol. 40, no. 5, pp. 569–578, 1992.
- [24] G. Watson, "The diffraction of electric waves by the earth", *Proceedings of the Royal Society of London Series A-containing Papers of a Mathematical and Physical Character*, vol. 95, no. 666, pp. 83–99, 1918.
- [25] V. Fock, "Diffraction of radio waves around the earths surface", *Zhurnal Eksperimentalnoi I Teoreticheskoi Fiziki*, vol. 15, no. 9, pp. 479–496, 1945.

- [26] P. H. Pathak and R. G. Kouyoumjian, "An analysis of the radiation from apertures in curved surfaces by the geometrical theory of diffraction", *Proceedings of the IEEE*, vol. 62, no. 11, pp. 1438–47, 1438–1447, 1974.
- [27] P. H. Pathak, N. Wang, W. D. Burnside, and R. G. Kouyoumjian, "A uniform gtd solution for the radiation from sources on a convex surface", *IEEE Transactions on Antennas and Propagation*, vol. AP-29, no. 4, pp. 609–22, 609–622, 1981.
- [28] P. H. Pathak and N. Wang, "Ray analysis of mutual coupling between antennas on a convex surface", *IEEE Transactions on Antennas and Propagation*, vol. 29, no. 6, pp. 911–922, 1981.
- [29] C. Tokgoz and R. J. Marhefka, "A UTD based asymptotic solution for the surface magnetic field on a source excited circular cylinder with an impedance boundary condition", *IEEE Transactions on Antennas and Propagation*, vol. 54, no. 6, pp. 1750–1757, 2006.
- [30] A. G. Aguilar, Z. Sipus, and M. Sierra-Perez, "An asymptotic solution for surface fields on a dielectric-coated circular cylinder with an effective impedance boundary condition", *IEEE Transactions on Antennas and Propagation*, vol. 61, no. 10, pp. 5175–5183, 2013.
- [31] B. Alisan, V. B. Erturk, and A. Altintas, "Efficient computation of nonparaxial surface fields excited on an electrically large circular cylinder with an impedance boundary condition", *IEEE Transactions on Antennas and Propagation*, vol. 54, no. 9, pp. 2559–2567, 2006.
- [32] A. Fort, F. Keshmiri, G. R. Crusats, C. Craeye, and C. Oestges, "A body area propagation model derived from fundamental principles: Analytical analysis and comparison with measurements", *IEEE Transactions on Antennas and Propagation*, vol. 58, no. 2, pp. 503–514, 2010.
- [33] P. H. Pathak and N. Wang, "An analysis of the mutual coupling between antennas on a smooth convex surface", *Final Report 784583-7*, The Ohio State University ElectroScience Lab., Dep. Elec. Eng. 1978.
- [34] C. Gabriel, S. Gabriel, and E. Corthout, "The Dielectric Properties of Biological Tissues: I. Literature Survey", *Physics in Medicine and Biology*, vol. 41, no. 11, pp. 2231–2249, Nov. 1996.
- [35] S. Gabriel, R. W. Lau, and C. Gabriel, "The Dielectric Properties of Biological Tissues: II. Measurements in the Frequency Range 10 Hz to 20 GHz", *Physics in Medicine and Biology*, vol. 41, no. 11, pp. 2251–2269, Nov. 1996.
- [36] —, "The Dielectric Properties of Biological Tissues: III. Parametric Models for the Dielectric Spectrum of Tissues", *Physics in Medicine and Biology*, Nov. 1996.
- [37] S. H. Kvist, J. Thaysen, and K. B. Jakobsen, "The Effect of the Head Size on the Ear-to-Ear Radio-Propagation Channel for Body-Centric Wireless Networks", in *2010 Loughborough Antennas and Propagation Conference (LAPC)*, Loughborough, UK, Nov. 2010, pp. 345–348.

- [38] —, “Investigation of the Ear-to-Ear Radio Propagation Channel”, in *5th European Conference on Antennas and Propagation (EuCAP)*, Rome, Italy, Apr. 2011, pp. 3640–3644.
- [39] —, “Ear-to-Ear On-Body Channel Fading in the ISM-Band for Tangentially-Polarized Antennas”, in *2011 Loughborough Antennas and Propagation Conference (LAPC)*, Loughborough, UK, Oct. 2011.
- [40] S. H. Kvist, P. F. Medina, J. Thaysen, and K. B. Jakobsen, “On-Body and Off-Body 2.45 GHz MIMO Communications for Hearing Instrument Applications”, in *7th European Conference on Antennas and Propagation (EuCAP)*, Gothenburg, Sweden, Apr. 2013, pp. 2595–2599.
- [41] P. F. Medina, S. H. Kvist, J. Thaysen, and K. B. Jakobsen, “Transmit and Receive Diversity in Body-Centric Wireless Communications”, in *34th Annual Antenna Measurement Techniques Association Symposium (AMTA 2012)*, Seattle, WA, USA, Oct. 2012, pp. 38–42.
- [42] H. Liu and J. L. Nielsen, “An efficient interference mitigation method for wireless hearing instruments network”, in *IEEE International Symposium on Personal, Indoor and Mobile Radio Communications, PIMRC*, IEEE, 2012, pp. 620–624.
- [43] J. Vidkjaer, “Linear Active Two-Ports”, in *Class Notes, 31415 RF-Communication Circuits*, <http://rftoolbox.dtu.dk/book/Ch3.pdf>, 2013, ch. 3.
- [44] R. Chandra and A. J. Johansson, “Influence on the ear-to-ear link loss from heterogeneous head phantom variations”, in *Proceedings of the 5th European Conference on Antennas and Propagation, Eucap 2011*, EurAAP, 2011, pp. 1612–1615.
- [45] N. P. I. Kammersgaard, S. H. Kvist, J. Thaysen, and K. B. Jakobsen, “Pinna model for hearing instrument applications”, in *Proceedings of 2014 Loughborough Antennas and Propagation Conference*, IEEE, 2014, pp. 141–143.
- [46] S. Pehrson, S. H. Kvist, J. Thaysen, and K. B. Jakobsen, “Morphological Investigation of the Differences on the Ear-to-Ear Path Gain and the Packet Loss at 2.45 GHz”, in *34th Annual Antenna Measurement Techniques Association Symposium (AMTA 2012)*, Seattle, WA, USA, Oct. 2012, pp. 43–48.
- [47] N. P. I. Kammersgaard, S. H. Kvist, J. Thaysen, and K. B. Jakobsen, “In-the-ear spiral monopole antenna for hearing instruments”, *Electronics Letters*, vol. 50, no. 21, pp. 1509–1511, 2014.
- [48] N. P. I. Kammersgaard, “Electrically Small In-the-Ear Antenna”, Master’s thesis, Technical University of Denmark (DTU), Kgs. Lyngby, Denmark, 2014.
- [49] S. H. Kvist, S. Özden, J. Thaysen, and K. B. Jakobsen, “Improvement of the Ear-to-Ear Path Gain at 2.45 GHz Using Parasitic Antenna Element”, in *6th European Conference on Antennas and Propagation (EuCAP)*, Prague, Czech Republic, Apr. 2012, pp. 944–947.
- [50] S. H. Kvist, J. Thaysen, and K. B. Jakobsen, “Polarization of Unbalanced Antennas for Ear-to-Ear On-Body Communications at 2.45 GHz”, in *2011 Loughborough Antennas and Propagation Conference (LAPC)*, Loughborough, UK, Oct. 2011.

- [51] R. Chandra and A. J. Johansson, "Miniaturized Antennas For Link Between Binaural Hearing Aids", in *32nd Annual International Conference of the IEEE Engineering in Medicine and Biology Society*, Buenos Aires, Argentina, Aug. 2010, pp. 688–691.
- [52] W. H. Yatman, L. K. Larsen, S. H. Kvist, J. Thaysen, and K. B. Jakobsen, "In-the-Ear Hearing-Instrument Antenna for ISM-Band Body-Centric Ear-to-Ear Communications", in *2012 Loughborough Antennas and Propagation Conference (LAPC)*, Loughborough, UK, Nov. 2012.
- [53] A. Ruaro, J. Thaysen, and K. B. Jakobsen, "Cavity-backed on-body antenna for customised hearing instrument applications", *Electronics Letters*, vol. 51, no. 16, pp. 1235–1236, 2015.
- [54] —, "Wearable shell antenna for 2.4 ghz hearing instruments", *IEEE Transactions on Antennas and Propagation*, vol. 64, no. 6, pp. 2127–2135, 2016.
- [55] L. Huitema, S. Sufyar, C. Delaveaud, and R. D'Errico, "Miniature Antenna Effect on the Ear-to-Ear Radio Channel Characteristics", in *6th European Conference on Antennas and Propagation (EuCAP)*, Prague, Czech Republic, Apr. 2012, pp. 3402–3406.
- [56] A. Ruaro, "EMC, RF, and Antenna Systems in Miniature Electronic Devices", PhD thesis, Technical University of Denmark (DTU), Kgs. Lyngby, Denmark, 2016.
- [57] A. Ruaro, J. Thaysen, and K. B. Jakobsen, "Battery coupling impact on the antenna efficiency in a small wearable device", in *2015 Loughborough Antennas and Propagation Conference (LAPC)*, IEEE, 2015.
- [58] R. Chandra and A. J. Johansson, "Analytical model, measurements, and effect of outer lossless shell of phantoms for on-body propagation channel around the body for body area networks", in *2015 9th European Conference on Antennas and Propagation, EuCAP 2015*, EurAAP, 2015.
- [59] K. Wei, Z. Zhang, and Z. Feng, "Design of a Wideband Horizontally Polarized Omnidirectional Printed Loop Antenna", *IEEE Antennas Wirel. Propag. Lett.*, vol. 11, pp. 49–52, 2012.
- [60] H. G. Booker, "Slot Aerials and Their Relation to Complementary Wire Aerials (Babinet's Principle)", *Journal of the Institution of Electrical Engineers*, vol. 93, no. 4, pp. 620–626, 1946.
- [61] M. Gustafsson, C. Sohl, and G. Kristensson, "Physical limitations on antennas of arbitrary shape", *Proceedings of the Royal Society A - mathematical Physical and Engineering Sciences*, vol. 463, no. 2086, pp. 2589–2607, 2007.
- [62] —, "Illustrations of new physical bounds on linearly polarized antennas", *IEEE Transactions on Antennas and Propagation*, vol. 57, no. 5, pp. 1319–1327, 2009.
- [63] M. Gustafsson, "Physical Bounds on Antennas of Arbitrary Shape", in *2011 Loughborough Antennas and Propagation Conference (LAPC)*, Loughborough, UK, Oct. 2011.

PAPER 1

“EAR-TO-EAR PROPAGATION MODEL BASED ON GEOMETRICAL THEORY OF DIFFRACTION”

N. P. B. Kammersgaard, S. H. Kvist, J. Thaysen, and K. B. Jakobsen

Submitted: Jan. 2018

[P1] N. P. B. Kammersgaard, S. H. Kvist, J. Thaysen, and K. B. Jakobsen, “Ear-to-ear propagation model based on geometrical theory of diffraction”, *Submitted to IEEE Transactions on Antennas and Propagation*, Jan. 2018.

Ear-to-Ear Propagation Model based on Geometrical Theory of Diffraction

Nikolaj P. B. Kammergaard, Søren H. Kvist, Jesper Thaysen, and Kaj B. Jakobsen

Abstract—An ear-to-ear propagation model based on geometrical theory of diffraction is presented. The model uses the creeping wave loss along the geodesic paths that connect the ears. It is the first model to investigate which geodesic paths that link the ears. The model uses geometrical theory of diffraction expressions for a lossy dielectric material, which is a much better approximation of the human body than the perfect electric conductor approximation often used. The model is validated for the industrial, scientific and medical band at 2.45 GHz. The model is valid at any frequency range as long as the propagation loss through the head is significantly higher than the propagation loss around the head. Likewise, the model could be used for other areas of the body. The comparison with simulations show strong correlation. The antenna orientation and frequency sweeps were performed to further investigate the model. The sweeps change the radiation pattern of the antenna to utilize different paths around the head, but the model still correlates with the simulation. This validates the models division of the ear-to-ear propagation into different geodesic paths around the head.

Index Terms—Geometrical Theory of Diffraction, On-Body, Off-Body, WBAN, Ear-to-Ear, Hearing Instruments, Creeping Wave.

I. INTRODUCTION

BODY-worn antennas and the area of on-body propagation have been a major research area in recent years. The continuous decrease in size and power consumption in modern electronics, together with improved receiver sensitivity, has enabled the implementation of wireless communication in more and more body-worn devices. Wireless communication is now a key part of for example smart watches, hearing instruments (HIs) and so-called ‘truly’ wireless headsets. In modern HIs, connectivity to off-body accessories and smart phones is becoming a must-have feature. The connectivity enables the HI user to receive phone calls, listen to music, or watch TV seamlessly. In most cases the Industrial, Scientific and Medical (ISM) band at 2.45 GHz is used for several reasons. It is available world wide and license free. Also, the Bluetooth® protocol is located in this band and is implemented in virtually all smart phones.

Besides connectivity with off-body devices it is desirable to archive ear-to-ear (E2E) connectivity between the HIs on either side of the head. The E2E communication between the HIs enables acoustic algorithms that improve the directionality of the sound amplification. It also improves the HIs’ ability

to coordinate and adjust the acoustic settings to the current acoustic environment. Furthermore, the E2E communication can be used to improve the range of the off-body communication [1].

In the recently emerged headset category of ‘truly’ wireless headsets, the E2E communication is also very important. The ‘truly’ refers to the fact that the headset consists of two separate devices in each ear that can only communicate with each other wirelessly. The E2E communication is crucial to the synchronization of the devices. Furthermore, in the current Bluetooth® protocol, streaming can only be done to one device. Therefore, the master of the two ear pieces needs to relay the received audio signal to the other device.

The many applications of the E2E channel illustrate the importance of a good understanding and modeling of the E2E propagation. Furthermore, the principles of the E2E channel are the same for other on-body propagation channels such as the pocket-to-ear channel between an audio streaming device in the pocket and a headset or HI in the ear. General on-body propagation models are numerous, for example [2]–[8]. Only a few models specific to the head exist [9], [10]. Many of these models use a perfect electric conductor (PEC) approximation of the human body [5]–[10], which is a rather crude model of the human body at 2.45 GHz, as discussed in [11]. Especially models of the head, but also many of the general models, do not clearly investigate or explain which paths the on-body propagation follows. In [10] two paths around the head are included, one around the front and one around the back. In [9] infinitely many paths are included. Many of the presented propagation models use geometrical theory of diffraction (GTD) as the approximation. It will also be applied here. In GTD it is well known that the propagation follows the geodesic lines on the surface of the object.

The purpose of this paper is to investigate the geodesic paths around the head that the on-body propagation follows. Combined with more exact approximations of the on-body propagation by a lossy dielectric GTD approximation [12], the on-body paths will be used to create a new E2E propagation model. The model will be the first to determine and make use of the geodesic lines on the head. At the same time it will be the first E2E model to use a lossy dielectric GTD approximation of the head instead of a PEC approximation.

In Section II the theoretical parts of the model will be presented. In Section III the simulation setup used to validate the model is described. The numerical challenges of implementing the model is discussed in Section IV. The results of the model as well as the simulations are presented and discussed in Section V. Finally, the conclusion is found in Section VI.

N. P. B. Kammergaard and K. B. Jakobsen are with the Electromagnetic Systems Group, Department of Electrical Engineering, Technical University of Denmark, Kgs. Lyngby, 2800 Denmark (e-mail: npivka@elektro.dtu.dk).

N. P. B. Kammergaard, S. H. Kvist and J. Thaysen are with GN Hearing A/S, Ballerup, 2750 Denmark.

Manuscript submitted January, 2018.

II. EAR-TO-EAR ON-BODY PROPAGATION MODEL

In [12] it was shown how to calculate the diffracted fields from a point source on any given lossy dielectric convex opaque structure. The diffracted fields from an electric point source \vec{J}_i on the surface of the structure along a given geodesic line are given by:

$$\vec{E}^d \sim \frac{j k_0 \eta_0}{4\pi} \vec{J}_i \cdot \vec{V} e^{-j k_0 t} \sqrt{\frac{d\psi_0}{d\chi}} \quad (1)$$

where $\eta_0 = \sqrt{\frac{\mu_0}{\epsilon_0}}$ is the intrinsic impedance of free space, μ_0 and ϵ_0 are the permeability and permittivity of free space, respectively, $k_0 = \omega \sqrt{\epsilon_0 \mu_0}$ is the wavenumber of free space and ω the angular frequency, t is the distance from the source along the geodesic line, $d\chi$ is the distance between adjacent rays at the observation point, $d\psi_0$ is the angle between adjacent rays at the source, and

$$\vec{V} \sim \sum_{p=1}^{\infty} \left(\hat{t}' L_{p,t}^e + \hat{b}' L_{p,b}^e + \hat{n}' L_{p,n}^e \right) \left(\hat{t} A_{p,t}^e + \hat{b} A_{p,b}^e + \hat{n} A_{p,n}^e \right) e^{-\int_0^t \alpha_p dt} \quad (2)$$

where $(\hat{t}', \hat{n}', \hat{b}')$ are the tangential, normal, and binormal unit vectors at the source point, respectively, and equivalently $(\hat{t}, \hat{n}, \hat{b})$ are the unit vectors at the observation point. The $L_{p,i}^e$ and $A_{p,i}^e$ are launching and attachment coefficients for electric point sources of specific polarizations, and α_p is the attenuation of the creeping wave. Exact expressions are found in [12], but the coefficients depend on frequency, constitutive parameters, and geometric factors. The subscript p refers to different modes, but in the deep shadow the first mode is all dominant and the summation over p will not be done in the remainder of the paper. Instead only the first mode will be used. Furthermore, the tangential and binormal contribution will be ignored since the magnitude of the launching and attachment coefficients for the first mode on the human body are more than 20 dB lower than the normal.

The electric field transmitted by an antenna in the polarization normal to the surface of the body of interest, $E_T^{\hat{n}}$, can be expressed through the gain, G_T , and the transmit power, P_T , as:

$$E_T^{\hat{n}} = \sqrt{\frac{2\eta_0 P_T G_T^{\hat{n}}}{4\pi}} e^{j\angle E_T^{\hat{n}}} \frac{e^{-jk_0 r}}{r} \quad (3)$$

where r is the distance from the antenna. Note that the angle of the electric field transmitted by an antenna, $\angle E_T^{\hat{n}}$ is only meaningful when the polarization is given. The transmitted electric field multiplied by $r e^{jk_0 r}$ will take the place of the term $\frac{j k_0 \eta_0}{4\pi}$ in Equation 1. This makes sense since the term $\frac{j k_0 \eta_0}{4\pi}$ is exactly the magnitude of the electric fields radiated from a unit strength electric dipole source. For convenience, the reference to the normal component, \hat{n} , will be suppressed throughout the rest of the paper, e.g., E_T and E_R .

The received electric field normal to the surface, E_R , can then be calculated for a geodesic path:

$$E_R = \sqrt{\frac{2\eta_0 P_T G_T}{4\pi}} e^{j\angle E_T} L A e^{-jk_0 t - \int_0^t \alpha dt} \sqrt{\frac{d\psi_0}{d\chi}} \quad (4)$$

By adding all the contributions from each of the geodesic paths that connect the transmitting and receiving antennas, the total open-circuit voltage at the terminals of the receiving antenna can be found:

$$V_{OC} = \sum_{i=1}^N E_{R,i} \ell_{e,i} \quad (5)$$

where N is the total number of geodesic paths that connect the transmitting and receiving antennas and ℓ_e is the electrical length of the receiving antenna assuming perfect match given by:

$$\ell_e = \sqrt{\frac{G_R \lambda_0^2 R_{ant}}{\pi \eta_0}} e^{j\angle E_{R,i}} \quad (6)$$

where λ_0 is the free space wave length and R_{ant} is the resistive part of the antenna impedance.

The received power can be calculated as:

$$P_R = \frac{|V_{OC}|^2}{8R_{ant}} \quad (7)$$

By combining Equations 4, 5 and 7 the E2E path gain can be expressed as:

$$\frac{P_R}{P_T} = \left(\frac{\lambda_0}{4\pi} \right)^2 \left| \sum_{i=1}^N \sqrt{G_{R,i} G_{T,i}} \frac{d\psi_{0,i}}{d\chi_i} L_i A_i e^{j(\angle E_{R,i} + \angle E_{T,i}) - j k_0 t_i - \int_0^{t_i} \alpha_i dt} \right|^2 \quad (8)$$

III. SIMULATION SETUP

The model was validated by the use of Ansys HFSS 18.2 simulations. The on-body radiation patterns were exported from the simulations for use in the model. The simulations were run with extremely strict convergence criteria to ensure correct results. The main convergence criterion was that the maximum achievable path gain (MAPG) should not change more than 0.1 dB, equivalent to a change of 2.27%. The MAPG $|S_{21}^{\max}|$ is used to avoid the impact of the impedance match. It is the path gain $|S_{21}|$ obtained when both antennas are perfectly matched and can be calculated using [13]. Since the path gain $|S_{21}|$ is very low, the antenna matching on one side does not impact the antenna impedance on the other side in practice. Therefore, the MAPG $|S_{21}^{\max}|$ can be approximated by:

$$|S_{21}^{\max}| \approx \frac{|S_{21}|^2}{(1 - |S_{11}|^2)(1 - |S_{22}|^2)} \quad (9)$$

For the reflection coefficient the convergence criterion was an absolute change of 0.02. Four consecutive converged passes were required before the simulation was considered converged.

The simulations were done on an Ansys HFSS version (faceted) of the Specific Anthropomorphic Mannequin (SAM), which had been modified with realistic ears, neck and shoulders. The neck and shoulders were included to ensure that no energy could creep around the bottom of the head. The simulation model is seen in Fig. 1. The antenna simulated has been presented in detail in [14], where the simulation results were also validated against measurements. The antenna

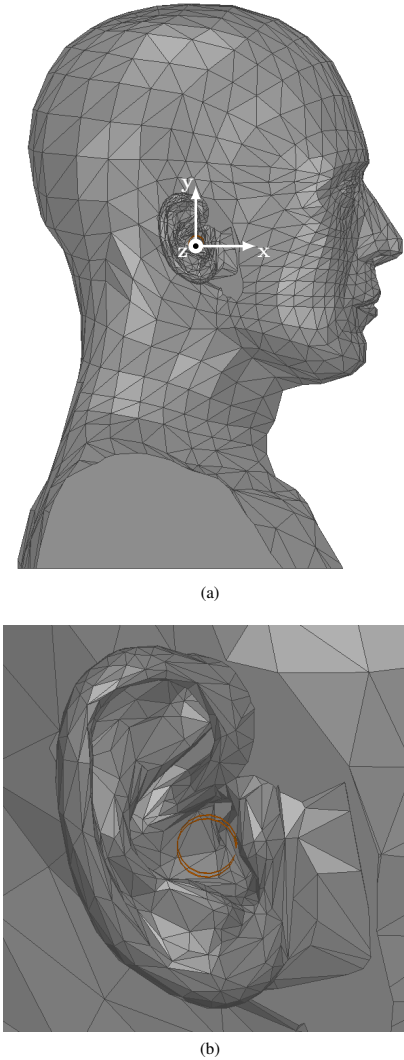


Fig. 1. The SAM phantom head (a) with the coordinate system used and a close up of the realistic ear (b) where the antenna can be seen (in red).

is visible in Fig. 1b. The simulations were all done at 2.45 GHz or for a frequency range with 2.45 GHz in the middle of the band. Therefore, the constitutive parameters used to model the human body were $\epsilon_r = 39.2$ and $\sigma = 1.8 \text{ S/m}$ as specified in [15] as standard parameters for the human body.

To investigate if the energy propagating through the head has significant importance for the results, a simulation with absorbers all around the head was run. It was found that the MAPG becomes -103.6 dB which is well below the -78.3 dB of the equivalent simulation without absorbers. However, the level is enough to cause a variation of up to $\pm 0.5 \text{ dB}$ dependent on the phase.

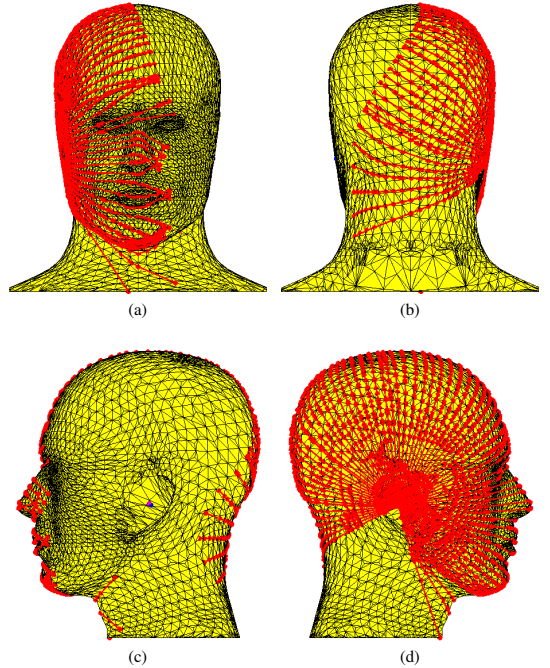


Fig. 2. The SAM phantom head with the geodesic path originating from the position of the right ear seen from the front (a), back (b), left (c), and right (d) side of the head. The geodesic paths shown end at 200 mm.

IV. MODEL IMPLEMENTATION

The main challenging part of implementing the proposed model is finding the geodesic lines on the given object, in this case the head. The geodesic lines are sometimes referred to as the shortest paths, although this can be a bit misleading. It is the generalization of straight lines to the surface of 3D objects. On a sphere the geodesic lines are the great circles, and on a cylinder they are helices. The formal definition is, that geodesic lines are lines on the surface that in their unit-speed parametrization only have acceleration perpendicular to the surface [16].

Here the geodesic lines were found on the head used for the simulations. The head is faceted to reduce the mesh complexity in Ansys HFSS. Therefore, the computation of the geodesic lines is very simple. On a facet, the geodesic line is naturally a straight line. When a geodesic line crosses from one facet to the next, the angle between the geodesic line and the edge separating the facets needs to stay constant. If one imagines that the two facets are flattened so they were in the same plane, the geodesic line would simply be a straight line.

When the geodesic lines were found on the original head seen in Fig. 1 the lines had a tendency to group together. There was a large gap between the lines that exit a facet on one or the other edge. This was caused by the large facets. To overcome this, the facet size was reduced. One could say that the head was up-sampled. This was done in the freely available software

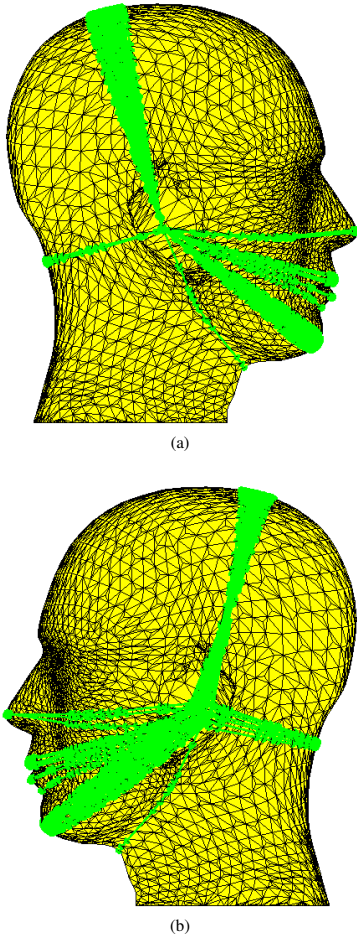


Fig. 3. The SAM phantom head geodesic lines that are emitted from the right ear and reaches the left ear seen from the right (a) and left (b) side of the head. The lines that falls within 10mm of the left antenna position are shown. The angle between the lines is 0.25° .

Blender used for 3D editing. The up-sampling was done with a setting to maintain the total volume. The result can be seen in Fig. 2. It would of course be better to have a mathematical description of the head, that is smooth and differentiable, but it would then be a mathematical challenge in it self to find the geodesic lines. It would be desirable to use the up-sampled head in the simulation, but this creates issues with the meshing of the complex geometry. Here the underlying assumption is that the faceted head does not make a significant difference from a smooth head, neither in simulations nor in the model.

In a few areas the head is concave. This is only in areas in the front of the head, mostly around the nose. The geodesic lines are found as simple straight lines across the concave areas. One could potentially calculate the diffraction at the point where the line escapes the surface of the head and again

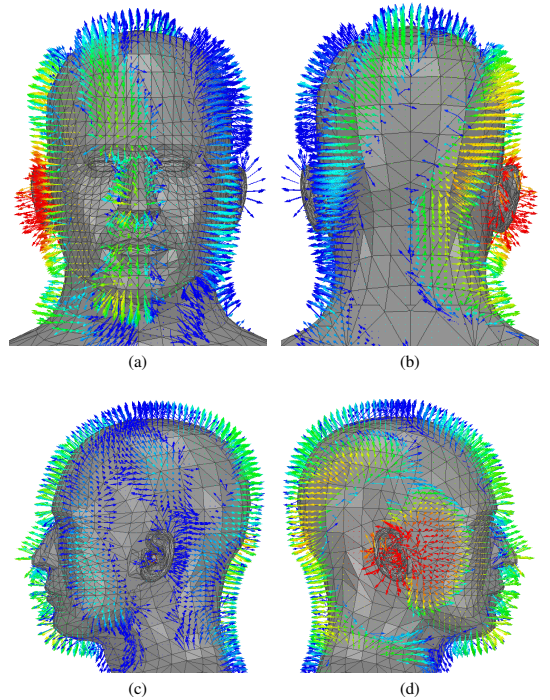


Fig. 4. The SAM phantom head with the simulated electric field just above the surface plotted as vectors seen from the front (a), back (b), left (c), and right (d) side of the head. The logarithmic color scale ranges from 50 V/m (red) to 0.5 V/m (blue).

when it contacts the surface. To reduce the complexity, and on the assumption of low impact on the result, this was not done. Instead, in the calculation of the loss, it has simply been included as a straight piece over the head.

It is noted that when finding the geodesic lines the ears had been removed. The ears are viewed as part of the antenna and the effect from the ears is included in the simulated radiation pattern that is put into the model.

In Fig. 2 geodesic paths originating from the right ears with a length of 200 mm is shown. It is seen that the geodesic lines create a wavefront. The paths around the back and over the top of the head are smoothly distributed. The paths around the front of the head is diffracted in different directions, but they still constitute a relatively uniform wavefront. In Fig. 3 only the geodesic lines that reach the antenna on the opposite side of the head are shown. It is clear that there is one path around the back, one over the top and four paths around the front. The four paths in the front run over the tip of the nose, the mouth, the chin and the transition from the head to the neck. There is possibly a path in the front at the root of the nose, but since it is so small the discrete number of lines does not capture it. This also means that it will not have a significant contribution. It is noted that each of the paths either constitute a local minimum or maximum with respect to the path length.

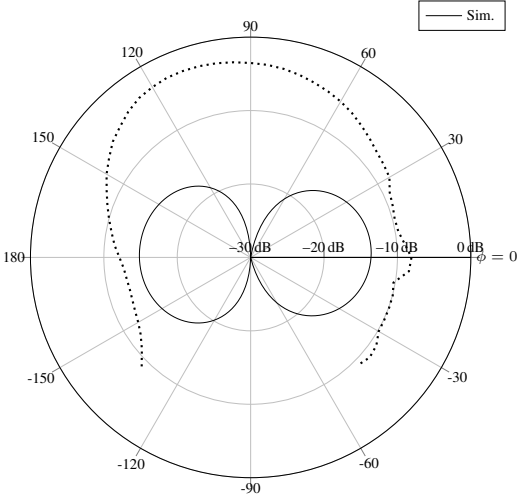


Fig. 5. Plane cut in the XY-plane of the magnitude of the theta component of the simulated radiation pattern at 2.45 GHz (solid line). The dotted line shows the contour of the head.

Each of the paths are approximated by 100 points. These are uniformly distributed along the path. To get estimates of the curvature and the torsion, the 100 points are smoothed. This is done with a local regression with a second degree polynomial. For each of these 100 points the attenuation is found. The numerical integration of the total loss is done with the trapezoidal method over the 100 points.

The final numerical challenge is to approximate the derivative $\frac{d\psi_0}{d\chi}$. Since the head model is faceted, the distance between lines is not continuous. Therefore the derivative for each of the six paths have been approximated as:

$$\frac{d\psi_0}{d\chi} = \sqrt{\frac{\Delta\psi_0 n_{lim}}{2\chi_{lim}}} \quad (10)$$

where $\Delta\psi_0 = 0.25^\circ$ is the discrete angle between adjacent lines at the source and n_{lim} is the number of lines for a given path that get within a certain distance, $\chi_{lim} = 10$ mm of the observation point.

V. RESULTS AND DISCUSSION

Various simulations were run to compare with the model. First, the antenna presented in [14] was simulated at 2.45 GHz. In [14] the measurements of the prototype antennas are found. In Fig. 4 the electric field vectors just above the surface of the head is shown. It is clearly seen that wavefronts similar to those in Fig. 2 are present. It is also seen from Fig. 4d that the wavefronts launched from the source have different phases. This justifies the use of the phase of the electric fields in the model. In Fig. 5 the magnitude of the gain of the right antenna in the XY-plane is seen. The antenna has two lobes, one towards the front and one towards the back. In Fig. 6 the phase of the antenna is seen. Compared to Fig. 4d it is seen to explain the phase differences between the lobes.

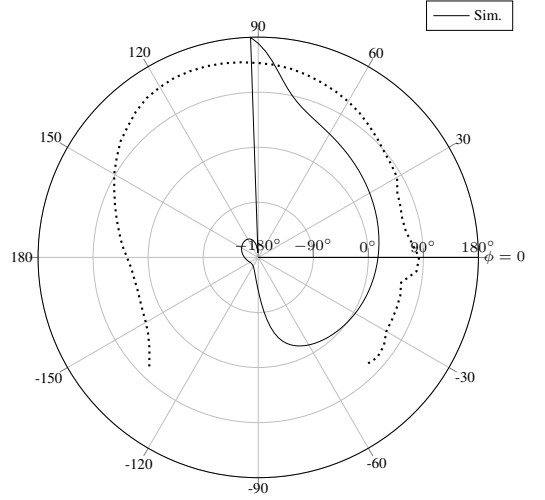


Fig. 6. Plane cut in the XY-plane of the phase of the theta component of the simulated radiation pattern at 2.45 GHz (solid line). The dotted line shows the contour of the head.

A simulation in the frequency range of 2 GHz to 3 GHz was done. The gain and phase of the antennas were exported and applied to the model. In Fig. 7 the magnitude of the simulated and modeled path gain is shown. The general trend of the curves are clearly the same; the path gains stay within 6 dB of each other over the entire frequency span. It is noted that even though strict convergence criteria were used, the convergence far away from the resonance frequency of the antenna and below -100 dB can not be completely guaranteed. Small changes in the mesh setup can change the simulation results with a few decibels at the edges of the frequency range, whereas the level at 2.45 GHz stays within 1 dB. In Fig. 8 the phase of the simulated and modeled path gain is shown. Good correspondence between the simulated and modeled results are seen here as well. The difference is again more pronounced at the edges of the frequency range.

To investigate if the common trends of the path gains are only caused by the effect of the reflection coefficient, the MAPG as given by Equation 9 was calculated. The simulated and modeled MAPG is shown in Fig. 9. It is seen that the trends of the two path gains remain the same even without the windowing effect of the reflection coefficient. Similarly, in order to see if the effect of the efficiency is the cause of the trend of the MAPG, the propagation gain, S_{21}^{prop} , was calculated. The propagation gain is given as the maximum achievable path gain divided by the radiation efficiency, ϵ_{cd} , squared:

$$S_{21}^{prop} = \frac{|S_{21}^{max}|}{\epsilon_{cd}^2} \quad (11)$$

The radiation efficiency is squared to remove the effect from the transmitting and the receiving antenna. The propagation gain is shown in Fig. 10. Even though the differences between

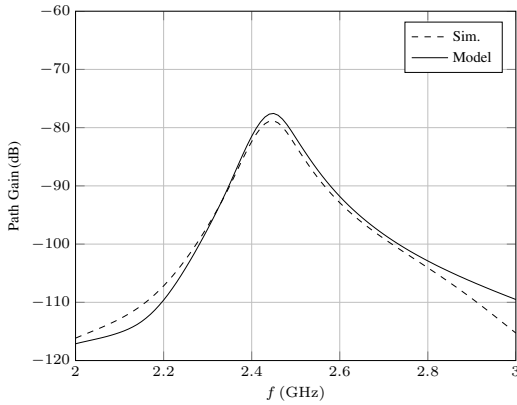


Fig. 7. Simulated (dashed line) and modeled (solid line) E2E path gain.

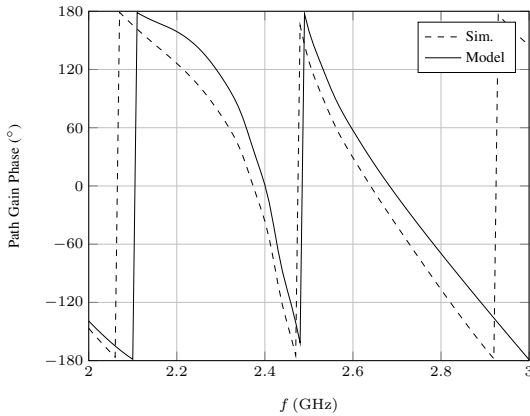


Fig. 8. Simulated (dashed line) and modeled (solid line) phase of the E2E path gain.

the simulated and modeled result are seen more clearly here, the general trend remains the same.

The contribution of the different paths around the head to the total modeled MAPG is seen in Fig. 11. The four paths around the front of the head have been aggregated. The main contributions clearly come from the front and back path. It is seen that the destructive interference of these two paths is the cause of the dip in the propagation gain around 2.2 GHz. The MAPG of both the front and the back path alone is higher than the total MAPG. The two paths are also seen to have increasing destructive interference towards 3 GHz since both path MAPGs are getting close to the total MAPG.

Here the modeled results use the radiation pattern from a full E2E simulation with a radiation surface defined around the ear and transformed to the far-field. An additional simulation was done where only a small rectangular cut-out including the right ear with the antenna inside was included. If the radiation pattern from that simulation is used, the modeled

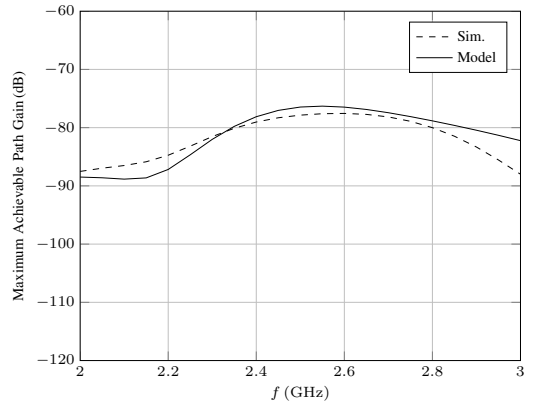


Fig. 9. Simulated (dashed line) and modeled (solid line) E2E maximum achievable path gain.

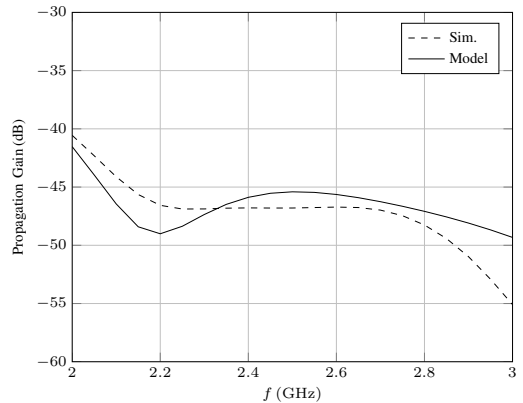


Fig. 10. Simulated (dashed line) and modeled (solid line) E2E propagation gain.

results remain the same within less than 1 dB. This enables the use of the model where only a cut-out simulation has been made. This is a much simpler and faster simulation to do than the full E2E simulation.

Another set of simulations were done at 2.45 GHz. The antenna was rotated in the ear in steps of 10° as done in [17]. Measurements can be found in that article as well. The simulated and modeled MAPG can be seen in Fig. 12. It is clear that the simulated and modeled results correlate well. The simulated and modeled propagation gain is seen in Fig. 13. The trends are still the same although the model does not replicate the entire dip in propagation gain at 300° .

In Fig. 14 the contributions of the different paths to the total MAPG is shown. At around 0° the main contribution comes from the front path. At around 180° almost no energy comes from the front path. The total MAPG is made up almost entirely of the back path contribution. This change in "main" path is not seen in Fig. 12, which confirms that the model

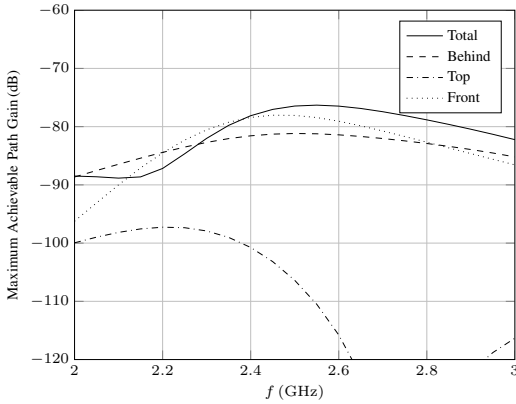


Fig. 11. Modeled E2E maximum achievable path gain divided into different paths. Total (solid), behind the head (dashed), over the top of the head (dash-dotted), and around the front of the head (dotted).

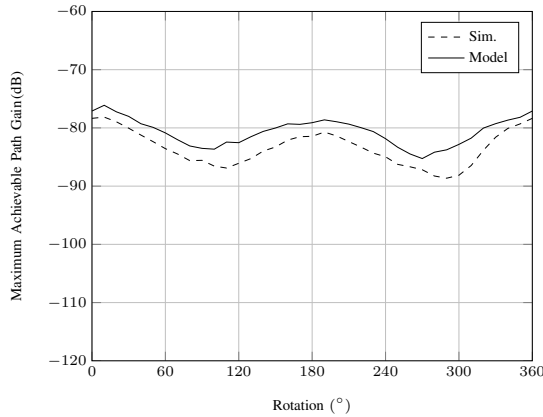


Fig. 12. Simulated (dashed line) and modeled (solid line) E2E maximum achievable path gain for different angles of rotation of the antenna.

captures the E2E propagations correctly.

VI. CONCLUSION

The first E2E propagation model to use the geodesic lines around a head has been presented. Furthermore, it is the first E2E model to utilize a lossy dielectric GTD approximation. The model shows good correlation with simulation, especially at the resonance frequency of the antenna. The correlation remains visible even when the envelope effect of the reflection coefficient as well as the efficiency is removed. Simulation of a small cut-out box around the ear combined with the model enables faster results for the E2E path gain. It has been shown that the model captures the transition between different 'main' paths. This validates the model's assumption of the division of the propagation into the different geodesic paths around the head.

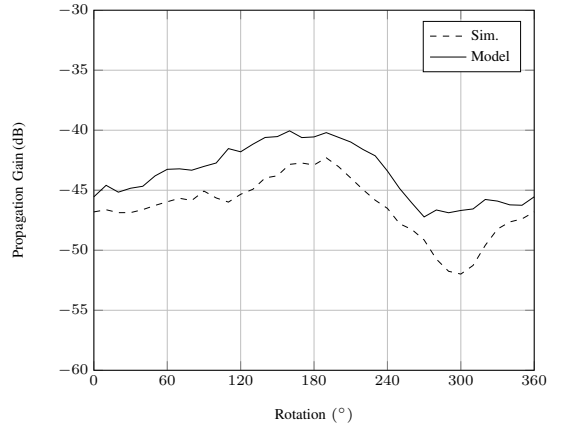


Fig. 13. Simulated (dashed line) and modeled (solid line) E2E propagation gain for different angles of rotation of the antenna.

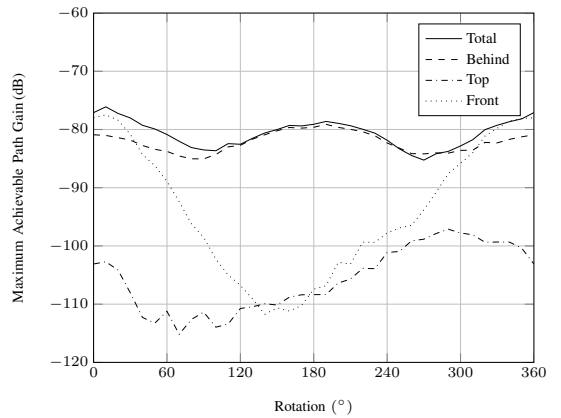


Fig. 14. Modeled E2E maximum achievable path gain divided into different paths for different angles of rotation of the antenna. Total (solid), behind the head (dashed), over the top of the head (dash-dotted), and around the front of the head (dotted).

REFERENCES

- [1] N. P. B. Kammergaard, S. H. Kvist, J. Thaysen, and K. B. Jakobsen, "Off-body transmission range improvement for hearing instruments by the use of ear-to-ear communication," in *Proceedings of 2015 Loughborough Antennas & Propagation Conference*. IEEE, 2015.
- [2] T. E. P. Alves, B. Poussot, and J.-M. Laheurte, "Analytical Propagation Modeling of BAN Channels Based on the Creeping-Wave Theory," *IEEE Trans. Antennas Propagat.*, vol. 59, no. 4, pp. 1269–1274, Apr. 2011.
- [3] C. Oliveira and L. M. Correia, "A Statistical Model to Characterize User Influence in Body Area Networks," in *Vehicular Technology Conference Fall (VTC 2010-Fall)*, 2010 IEEE 72nd, Sep. 2010.
- [4] E. Plouhinec, B. Uguen, M. Mhedhbi, and S. Avrillon, "3D UTD modeling of a measured antenna disturbed by a dielectric circular cylinder in WBAN context," in *2014 IEEE 79th Vehicular Technology Conference (VTC Spring)*, May 2014, pp. 1–5.
- [5] M. Ghaddar, L. Talbi, and T. A. Denidni, "Human Body Modelling for Prediction of Effect of People on Indoor Propagation Channel," *Electronics Letters*, vol. 40, no. 25, pp. 1592–1594, Dec 2004.

- [6] R. Chandra and A. J. Johansson, "An Analytical Link-Loss Model for On-Body Propagation Around the Body Based on Elliptical Approximation of the Torso With Arms' Influence Included," *IEEE Antennas and Propag. Lett.*, vol. 12, pp. 528–531, Apr 2013.
- [7] Y. Zhao, Y. Hao, A. Alomainy, and C. G. Parini, "UWB On-Body Radio Channel Modeling Using Ray Theory and Subband FDTD Method," *IEEE Trans. Microwave Theory Tech.*, vol. 54, no. 4, pp. 1827–1835, Apr 2006.
- [8] Y. Hao, A. Alomainy, Y. Zhao, C. G. Parini, Y. I. Nechayev, P. S. Hall, and C. C. Constantinou, "Statistical and Deterministic Modelling of Radio Propagation Channels in WBAN at 2.45GHz," in *Antennas and Propagation Society International Symposium 2006, IEEE*, 2006, pp. 2169–2172.
- [9] S. H. Kvist, J. Thaysen, and K. B. Jakobsen, "Ear-to-ear on-body channel model for hearing aid applications," *IEEE Transactions on Antennas and Propagation*, vol. 63, no. 1, pp. 344–352, 2015.
- [10] R. Chandra and A. J. Johansson, "A link loss model for the on-body propagation channel for binaural hearing aids," *IEEE Trans. Antennas Propag.*, vol. 61, no. 12, pp. 6180–6190, 2013.
- [11] N. P. B. Kammersgaard, S. H. Kvist, J. Thaysen, and K. B. Jakobsen, "Validity of PEC approximation for on-body propagation," *2016 10th European Conference on Antennas and Propagation (EuCAP)*, 2016.
- [12] —, "Geometrical theory of diffraction formulation for on-body propagation," *Submitted to IEEE Transactions on Antennas and Propagation*, 2018.
- [13] J. Vidkjaer, "Linear Active Two-Ports," in *Class Notes, 31415 RF-Communication Circuits*, 2013, ch. 3. [Online]. Available: <http://rftoolbox.dtu.dk/book/Ch3.pdf>
- [14] N. P. I. Kammersgaard, S. H. Kvist, J. Thaysen, and K. B. Jakobsen, "In-the-ear circular-shaped balanced inverted-a antenna for hearing instruments," *IEEE Antennas and Wireless Propagation Letters*, vol. 15, pp. 1839–1843, 2016.
- [15] "IEEE recommended practice for determining the peak spatial-average specific absorption rate (SAR) in the human head from wireless communications devices: Measurement techniques," 2013.
- [16] A. Pressley, *Elementary differential geometry*, 2nd ed. Springer, 2010.
- [17] N. P. I. Kammersgaard, S. H. Kvist, J. Thaysen, and K. B. Jakobsen, "Impact of placement of in-the-ear antenna on ear-to-ear path gain," *Proceedings of 2015 Loughborough Antennas & Propagation Conference*, 2015.



Nikolaj Peter Brunvoll Kammersgaard received the B.Sc. and M.Sc. degrees in electrical engineering from the Technical University of Denmark, Lyngby, in 2013 and 2014, respectively. Since 2014, he has been affiliated with GN Hearing A/S, a Danish hearing aid manufacturer, where he is currently pursuing an Industrial Ph.D. degree in cooperation with the Technical University of Denmark. His research interests include on-body antennas and propagation, as well as electrically small antennas and physical limitations of antennas. He was awarded the Student

Paper Award for best student paper at the International Workshop on Antenna Technology 2015. In 2015, he was awarded with "Kandidatprisen" from the Danish Association of Engineers (IDA). The award is given to three recently graduated promising electrical engineers for their Master's thesis.



Søren Helstrup Kvist received the B.Sc., M.Sc. and Ph.D. degrees in electrical engineering from the Technical University of Denmark in 2007, 2009 and 2014, respectively. Since 2009 he has been affiliated with GN Hearing A/S, a Danish hearing aid manufacturer, where he is currently employed as manager of the Radio Systems group. His research interests include on-body antennas and propagation, as well as electrically small antennas and physical limitations of antennas. Dr. Kvist was awarded the "Elektroprisen 2015" from the Danish Association

of Engineers (IDA). The award is given for excellent technical and scientific work within electrical engineering.



Jesper Thaysen received the B.Sc., M.Sc. and Ph.D. degrees in electrical engineering from the Technical University of Denmark in 1998, 2000 and 2005, respectively, and an MBA from Middlesex University in 2015. Since 2008 he has been employed at GN Hearing A/S, a Danish hearing aid manufacturer, where he currently acts as the Head of the Global Manufacturing Organization. His research interests include small antennas and on-body antennas and propagation. Dr. Thaysen has overseen more than 40 B.Sc. and M.Sc. students, as well as 3 Ph.D.

students, as the company representative in university-industry cooperative projects.



Kaj Bjarne Jakobsen received the B.Sc.EE and the M.Sc.EE degree from the Technical University of Denmark, Kgs. Lyngby, in 1985 and 1986, respectively, the Ph.D. degree in Electrical Engineering from University of Dayton, Dayton, OH, in 1989, and the HD in Organization and Management, Copenhagen Business School, Copenhagen in 2000. From 1986-1989 he was a Fulbright Scholar at the Department of Electrical Engineering, University of Dayton, OH. Since 1990 he has been with the Department of Electrical Engineering, Technical University of Denmark, Kgs. Lyngby, where he is Associate Professor. His research interests are in body-centric wireless network, wireless body area network, and body sensor network. He received in 1989 the NCR Stakeholder Award, Ohio, USA, and was appointed Teacher-of-the-Year at the Technical University of Denmark in 1994.

University of Denmark, Kgs. Lyngby, where he is Associate Professor. His research interests are in body-centric wireless network, wireless body area network, and body sensor network. He received in 1989 the NCR Stakeholder Award, Ohio, USA, and was appointed Teacher-of-the-Year at the Technical University of Denmark in 1994.

PAPER 2

“GEOMETRICAL THEORY OF DIFFRACTION FORMULATION FOR ON BODY PROPAGATION”

N. P. B. Kammersgaard, S. H. Kvist, J. Thaysen, and K. B. Jakobsen

Submitted: Jan. 2018

[P2] N. P. B. Kammersgaard, S. H. Kvist, J. Thaysen, and K. B. Jakobsen, “Geometrical theory of diffraction formulation for on body propagation”, *Submitted to IEEE Transactions on Antennas and Propagation*, Jan. 2018.

Geometrical Theory of Diffraction Formulation for On-Body Propagation

Nikolaj P. B. Kammersgaard, Søren H. Kvist, Jesper Thaysen, and Kaj B. Jakobsen

Abstract—A Geometrical Theory of Diffraction model for on-body propagation is developed in the article. The exact solution to the canonical problem of a plane wave incident on an infinitely long cylinder, with arbitrary constitutive parameters, is found. The same is done for a magnetic and an electric infinitesimal dipole source of any orientation, located on the surface of the cylinder. The exact solutions are transformed with the Watson transformation to yield asymptotic expressions that are valid in the deep shadow region. These asymptotic expressions are validated by comparison to the numerically evaluated exact solution. It is found that the expressions are valid as long as the object is opaque, with a geometry down to the size of $\frac{\kappa}{\kappa^2 + \tau^2} > \lambda_0/2$, and the rays not too torsional $\tau/\kappa < 2$, where κ and τ are the curvature and torsion of the local geometry, respectively. The asymptotic expressions are found to approximate the exact solution significantly better than the asymptotic expression of an equivalent perfect electric conductor geometry. The same is the case for the impedance boundary condition asymptotic approximation for low dielectric constant materials. Finally, the asymptotic expressions are generalized so they can be applied to any convex geometry of the human body or an opaque lossy dielectric of electrically large size.

Index Terms—Geometrical Theory of Diffraction, asymptotic approximation, on-body communication, WBAN, lossy dielectric cylinder.

I. INTRODUCTION

ON-BODY antennas and propagation have received enormous attention in recent years. It has been a major research area, but has recently also resulted in many commercial uses. Within the past two years, for example, more than 10 sets of so-called ‘truly’ wireless headsets have been launched. The ‘truly’ wireless term refers to the fact that these headsets have independent left and right devices with no wire in-between. These devices are dependent on the following three kinds of connections; on-body communication between the ears or Ear-to-Ear (E2E) communication, on-body communication to for example a phone in the pocket or Pocket-to-Ear (P2E) communication, and off-body communication with any kind of music streaming device not placed on the body. Exactly the same user cases are present for modern BlueTooth[®] connected Hearing Instruments (HIs). For the HIs, the E2E communication is important in order to improve the acoustic performance. The E2E connection allows the two HIs’ microphones on the left and right ear, respectively, to work together in a similar manner as an antenna array.

N. P. B. Kammersgaard and K. B. Jakobsen are with the Electromagnetic Systems Group, Department of Electrical Engineering, Technical University of Denmark, Kgs. Lyngby, 2800 Denmark (e-mail: npivka@elektro.dtu.dk).

N. P. B. Kammersgaard, S. H. Kvist and J. Thaysen are with GN Hearing A/S, Ballerup, 2750 Denmark.

Manuscript submitted January, 2018.

The exact understanding and modeling of the propagation of the fields on the surface of the body is crucial in order to design on-body wireless devices. The use of creeping wave theory has proven to be a good approximation in many cases. Primarily Geometrical Theory of Diffraction (GTD) or Uniform Geometrical Theory of Diffraction (UTD) have been applied to the problem of on-body propagation. Examples of the use of GTD or UTD can be found in [1]–[3]. In most cases the body is assumed to be a Perfect Electric Conductor (PEC) [3]–[6]. Others only investigate torsion free cases [1], [7], [8]. The validity of the PEC approximation as well as influence of torsion was briefly investigated in [9], [10].

A GTD/UTD formulation for the Impedance Boundary Condition (IBC) was done in [11], [12]. This approximation would be more appropriate to use for on-body propagation than the PEC assumption. The IBC approximation is based on an assumption only valid for a material with high conductivity, however. This assumption is not fulfilled for human tissue at 2.45 GHz, and therefore it is relevant to find a formulation valid for human tissue.

The purpose of this work is to provide a GTD formulation for the on-body propagation. The model should be as precise as possible but yet intuitive. This is why GTD is chosen in this work instead of UTD. The intuitiveness of the exponential decaying fields in GTD outweighs the precision of the UTD in the transition region. Still the model should include effects from the electromagnetic properties of the human tissue, the frequency and polarization of the electromagnetic field, as well as the curvature and torsion of the geometry.

The model addresses two types of propagation. The first is the off-body connection between an antenna on the body and an antenna off the body. By assuming the off-body antenna is placed in the far-field, this can be modeled by calculating the fields on an infinite long, lossy dielectric (human tissue) cylinder caused by an incident plane wave. The second is the on-body connection between two antennas placed on the body. This is modeled by calculating the fields on an infinite long, lossy dielectric (human tissue) cylinder caused by an infinitesimal dipole source on the surface of the cylinder. The cylinder is chosen since it gives rise to geodesics (shortest paths) with all combinations of curvature and torsion. This makes it possible to approximate any kind of geometry by the assumption that the propagation only depends on the local geometry. Therefore, general GTD expressions for the off-body and on-body propagation can be found from these two canonical problems.

The paper is organized as follows. In Section II the eigenfunction solution to the two canonical problems are found.

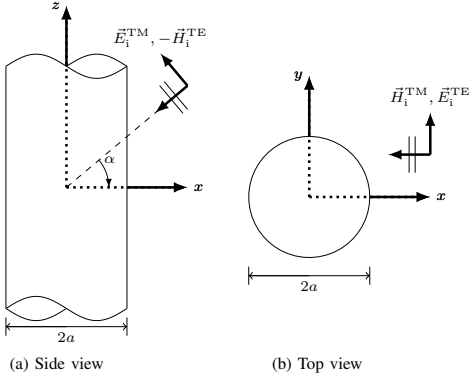


Fig. 1. The geometry of the infinitely long dielectric cylinder model with an incident plane wave.

In Section III the asymptotic or GTD expressions are found. In Section IV, numerical calculations of the eigenfunction solution to the plane wave incidence case is compared to the asymptotic solution to validate the expression. Furthermore, the limitations of the GTD solution is investigated. In Section V the GTD expressions for the two cases are generalized to any geometry. Finally, Section VI contains the conclusion.

An $e^{j\omega t}$ time dependence for the electromagnetic fields are assumed and suppressed throughout the paper. The constitutive parameters of human tissue are taken from [13], [14].

II. EIGENFUNCTION SOLUTION

A. Plane Wave Incidence

The solution to the canonical problem of an infinite long, lossy dielectric cylinder illuminated by a oblique incident plane wave is shown in the following. The geometry is seen in Fig. 1. A standard polar coordinate system is used, based on the coordinate system shown in the figure. The original solution can be found in [15], [16]. Note that [15] has a sign error in the coefficient named c_n as pointed out in [9]. The problem has also previously been solved for a IBC cylinder [11]. The notation of [11] is used.

The incident TM_z and TE_z polarized plane wave is given by:

$$\vec{E}_1^{\text{TM}}(\rho, \phi, z) = E_0(\hat{z} \cos \alpha - \hat{x} \sin \alpha) e^{jk_0(z \sin \alpha + \rho \cos \phi \cos \alpha)} \quad (1a)$$

$$\vec{E}_1^{\text{TE}}(\rho, \phi, z) = E_0 \hat{y} e^{jk_0(z \sin \alpha + \rho \cos \phi \cos \alpha)} \quad (1b)$$

where $k_0 = \omega \sqrt{\epsilon_0 \mu_0}$ is the free space wave number with the free space permittivity and permeability given by ϵ_0 and μ_0 , respectively. E_0 is the amplitude of the incident wave. And α is the angle of incidence as shown in Fig. 1.

Vector potentials for TM_z and TE_z polarized incident waves are introduced with the notation of [17]:

- For a TM_z incident wave: $\vec{A}_z^{\text{TM}} = \hat{z} A_z^{\text{TM}}$, $\vec{F}_z^{\text{TM}} = \hat{z} F_z^{\text{TM}}$ and

$$\vec{E}_1 = -\nabla \times \vec{F}_z^{\text{TM}} + \frac{1}{j\omega\epsilon_0} \nabla \times \nabla \times \vec{A}_z^{\text{TM}} \quad (2a)$$

$$\vec{H}_1 = \nabla \times \vec{A}_z^{\text{TM}} + \frac{1}{j\omega\mu_0} \nabla \times \nabla \times \vec{F}_z^{\text{TM}} \quad (2b)$$

- For a TE_z incident wave: $\vec{F}_z^{\text{TE}} = \hat{z} F_z^{\text{TE}}$, $\vec{A}_z^{\text{TE}} = \hat{z} A_z^{\text{TE}}$ and

$$\vec{E}_2 = -\nabla \times \vec{F}_z^{\text{TE}} + \frac{1}{j\omega\epsilon_0} \nabla \times \nabla \times \vec{A}_z^{\text{TE}} \quad (3a)$$

$$\vec{H}_2 = \nabla \times \vec{A}_z^{\text{TE}} + \frac{1}{j\omega\mu_0} \nabla \times \nabla \times \vec{F}_z^{\text{TE}} \quad (3b)$$

The total field will be a superposition of these fields:

$$\vec{E} = \vec{E}_1 + \vec{E}_2 \quad (4a)$$

$$\vec{H} = \vec{H}_1 + \vec{H}_2 \quad (4b)$$

It can be shown that the TM_z and TE_z potentials satisfy the same wave equation as the fields [17]:

$$(\nabla^2 + k_0^2) \begin{bmatrix} \vec{A}_z \\ \vec{F}_z \end{bmatrix} = 0 \quad (5)$$

The approach in [15] is followed. First the z variation is isolated in the term $e^{jk_z z}$ where $k_z = k_0 \sin \alpha$. The incident plane wave is written with the expansion of the $e^{j\rho \cos \phi \sin \alpha}$ term by the use of first-order Bessel functions. This gives the following equations for the fields outside the cylinder:

$$\begin{bmatrix} A_z \\ F_z \end{bmatrix} = e^{jk_z z} \sum_{n=-\infty}^{\infty} j^n e^{-jn\phi} \begin{bmatrix} \tilde{A}_z \\ \tilde{F}_z \end{bmatrix} \quad (6)$$

where ϕ and z are the coordinates for the observation point and \tilde{A}_z and \tilde{F}_z are given by:

$$\begin{bmatrix} \tilde{A}_z^{\text{TM}} \\ \tilde{F}_z^{\text{TE}} \end{bmatrix} = \begin{bmatrix} C_0^m \\ C_0^e \end{bmatrix} \left(J_n(k_{t0}\rho) - \begin{bmatrix} A_n^m \\ A_n^e \end{bmatrix} H_n^{(2)}(k_{t0}\rho) \right) \quad (7a)$$

$$\begin{bmatrix} \tilde{F}_z^{\text{TM}} \\ \tilde{A}_z^{\text{TE}} \end{bmatrix} = \begin{bmatrix} -C_0^e \\ C_0^m \end{bmatrix} A_n^c H_n^{(2)}(k_{t0}\rho) \quad (7b)$$

where ρ is the coordinate of the observation point, $k_{t0} = k_0 \cos \alpha$ and $\eta_0 = \sqrt{\frac{\mu_0}{\epsilon_0}}$ is the intrinsic impedance of free space, J_n are first-order Bessel functions, $H_n^{(2)}$ are second-order Hankel functions and:

$$C_0^m = E_0 \frac{j}{\eta_0 k_{t0}} \quad (8a)$$

$$C_0^e = E_0 \frac{1}{j k_{t0}} \quad (8b)$$

Similar expressions for the fields inside the cylinder can be found in [15], [16]. The tangential fields inside and outside the cylinder are equated at the surface of the cylinder to satisfy the boundary conditions. This gives the following coefficients:

$$\begin{bmatrix} A_n^m \\ A_n^e \end{bmatrix} = \frac{J_n(k_{t0}a) \left(\begin{bmatrix} F_n N_n \\ G_n M_n \end{bmatrix} - q_c^2 \right)}{H_n^{(2)}(k_{t0}a) (F_n G_n - q_c^2)} \quad (9a)$$

$$A_n^c = \frac{2q_c}{\pi(k_{t0}a) \left(H_n^{(2)}(k_{t0}a) \right)^2 (F_n G_n - q_c^2)} \quad (9b)$$

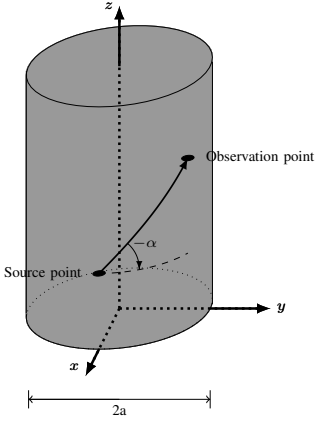


Fig. 2. The geometry of the infinitely long dielectric cylinder model with a source and observation point. The source and observation points are connected by the shortest path between them.

with

$$\begin{bmatrix} F_n \\ G_n \end{bmatrix} = \frac{H_n^{(2)'}(k_{t0}a)}{H_n^{(2)}(k_{t0}a)} - \begin{bmatrix} q_e \\ q_m \end{bmatrix} \frac{J_n'(k_{t1}a)}{J_n(k_{t1}a)} \quad (10a)$$

$$\begin{bmatrix} M_n \\ N_n \end{bmatrix} = \frac{J_n'(k_{t0}a)}{J_n(k_{t0}a)} - \begin{bmatrix} q_e \\ q_m \end{bmatrix} \frac{J_n'(k_{t1}a)}{J_n(k_{t1}a)} \quad (10b)$$

where $k_{t1} = \sqrt{k_1^2 - (k_0 \sin \alpha)^2}$. The wave number of the lossy dielectric k_1 is given by $k_1 = \omega \sqrt{\epsilon_1 \mu_1}$ with the permittivity and permeability of the lossy dielectric given by ϵ_1 and μ_1 , respectively, and finally,

$$q_m = \frac{\epsilon_1 k_{t0}}{\epsilon_0 k_{t1}} \quad (11a)$$

$$q_e = \frac{\mu_1 k_{t0}}{\mu_0 k_{t1}} \quad (11b)$$

$$q_c = \frac{nk_z}{k_{t0}k_0a} \left[1 - \left(\frac{k_{t0}}{k_{t1}} \right)^2 \right] \quad (11c)$$

B. Infinitesimal Dipole Sources

The canonical problem of the fields from an infinitesimal dipole source on the surface of an infinitely long dielectric cylinder is solved in the following. The focus is on the case with the observation point placed on the surface of the cylinder as well. This makes it possible to calculate the coupling or path loss between two infinitesimal dipoles on the surface. The geometry is defined in Fig. 2. Again a standard polar coordinate system is used. Without loss of generalization, the source point is assumed to be at $(x=a, y=0, z=0)$. The location of the observation point is then simply given by its coordinates. A similar approach for the impedance boundary conditions has been made in [12], [18], [19] and for a perfect electric conductor in [20]–[22]. The case with the source away from the cylinder is solved in [23]. The same potentials as

defined in Eq. 2 and Eq. 3 are used. Furthermore, the following Fourier transforms of the potentials are defined:

$$A_z = \frac{1}{2\pi} \sum_{n=-\infty}^{\infty} e^{jn\phi} \int_{-\infty}^{\infty} \tilde{A}_z e^{jk_z z} dk_z \quad (12a)$$

$$F_z = \frac{1}{2\pi} \sum_{n=-\infty}^{\infty} e^{jn\phi} \int_{-\infty}^{\infty} \tilde{F}_z e^{jk_z z} dk_z \quad (12b)$$

where ϕ and z are the coordinates of the observation point.

By solving the boundary condition on the cylinder for the tangential fields, the potentials from tangential magnetic and electric infinitesimal dipoles can be found. The potentials from the z -oriented sources become:

$$\tilde{A}_z = \frac{H_n^{(2)}(k_{t0}\rho)}{2\pi a k_{t0} (F_n G_n - q_c^2) H_n^{(2)}(k_{t0}a)} \cdot \left(-F_n J_z - \frac{j q_c}{\eta_0} M_z \right) \quad (13a)$$

$$\tilde{F}_z = \frac{H_n^{(2)}(k_{t0}\rho)}{2\pi a k_{t0} (F_n G_n - q_c^2) H_n^{(2)}(k_{t0}a)} \cdot (j \eta_0 q_c J_z - G_n M_z) \quad (13b)$$

where ρ is the radial coordinate of the observation point, which will be equal to a in our case. J_z and M_z are the z -oriented electric and magnetic dipole moments, respectively. And the potentials from the ϕ -oriented sources are:

$$\tilde{A}_\phi = \frac{H_n^{(2)}(k_{t0}\rho)}{2\pi a k_{t0} (F_n G_n - q_c^2) H_n^{(2)}(k_{t0}a)} \cdot \left[\left(\frac{k_z n H_n^{(2)'}(k_{t0}a)}{k_{t0} a k_{t1}^2 H_n^{(2)}(k_{t0}a)} - \frac{q_e k_z n J_n'(k_{t0}a)}{k_{t0}^3 a J_n(k_{t0}a)} \right) J_\phi - \left(\frac{j k_1 J_n'(k_{t0}a)}{k_{t1} \eta_1 J_n(k_{t0}a)} F_n - \frac{j n k_z}{\eta_0 k_{t1}^2 a} q_c \right) M_\phi \right] \quad (14a)$$

$$\tilde{F}_\phi = \frac{H_n^{(2)}(k_{t0}\rho)}{2\pi a k_{t0} (F_n G_n - q_c^2) H_n^{(2)}(k_{t0}a)} \cdot \left[\left(\frac{j k_1 \eta_1 J_n'(k_{t0}a)}{k_{t1} J_n(k_{t0}a)} G_n - \frac{j \eta_0 n k_z}{k_{t1}^2 a} q_c \right) J_\phi + \left(\frac{k_z n H_n^{(2)'}(k_{t0}a)}{k_{t0} a k_{t1}^2 H_n^{(2)}(k_{t0}a)} - \frac{q_m k_z n J_n'(k_{t0}a)}{k_{t0}^3 a J_n(k_{t0}a)} \right) M_\phi \right] \quad (14b)$$

where J_ϕ and M_ϕ are the ϕ -oriented electric and magnetic dipole moments, respectively. In the potentials the symbols are defined as for the plane wave incidence, except for k_z that is a variable here. This also effects k_{t0} and k_{t1} , which will be given as $k_{t0} = \sqrt{k_0^2 - k_z^2}$ and $k_{t1} = \sqrt{k_1^2 - k_z^2}$. The definition of q_m , q_e and q_c are the same, but the updated expressions for k_{t0} , k_{t1} and k_z should be used.

The potentials from the magnetic and electric infinitesimal dipoles oriented normal to the surface of the cylinder can be

found by the use of the reciprocity theorem and the fields from the z-oriented sources as shown here:

$$E_{\rho}^{J_z} J_{\rho} = E_z^{J_{\rho}} J_z = \frac{1}{j\omega\epsilon_0} k_{t0}^2 A_z^{J_{\rho}} J_z \quad (15a)$$

$$E_{\rho}^{M_z} J_{\rho} = -H_z^{J_{\rho}} M_z = -\frac{1}{j\omega\mu_0} k_{t0}^2 F_z^{J_{\rho}} M_z \quad (15b)$$

$$H_{\rho}^{J_z} M_{\rho} = -E_z^{M_{\rho}} J_z = -\frac{1}{j\omega\epsilon_0} k_{t0}^2 A_z^{M_{\rho}} J_z \quad (15c)$$

$$H_{\rho}^{M_z} M_{\rho} = H_z^{M_{\rho}} M_z = \frac{1}{j\omega\mu_0} k_{t0}^2 F_z^{M_{\rho}} M_z \quad (15d)$$

The potentials from the ρ -oriented sources become:

$$\begin{aligned} \tilde{A}_z = & \frac{H_n^{(2)}(k_{t0}\rho)}{2\pi a k_{t0} (F_n G_n - q_c^2) H_n^{(2)}(k_{t0}a)} \\ & \cdot \left[\left(\frac{jnk_0}{k_{t0}^2 a} q_c - \frac{jk_z H_n^{(2)'}(k_{t0}a)}{k_{t0} H_n^{(2)}(k_{t0}a)} F_n \right) J_{\rho} \right. \\ & \left. - \left(\frac{nk_0}{k_{t0}^2 a \eta_0} F_n - \frac{k_z H_n^{(2)'}(k_{t0}a)}{k_{t0} \eta_0 H_n^{(2)}(k_{t0}a)} q_c \right) M_{\rho} \right] \quad (16a) \end{aligned}$$

$$\begin{aligned} \tilde{F}_z = & \frac{H_n^{(2)}(k_{t0}\rho)}{2\pi a k_{t0} (F_n G_n - q_c^2) H_n^{(2)}(k_{t0}a)} \\ & \cdot \left[\left(\frac{nk_0 \eta_0}{k_{t0}^2 a} G_n - \frac{k_z \eta_0 H_n^{(2)'}(k_{t0}a)}{k_{t0} H_n^{(2)}(k_{t0}a)} q_c \right) J_{\rho} \right. \\ & \left. + \left(\frac{jnk_0}{k_{t0}^2 a} q_c - \frac{jk_z H_n^{(2)'}(k_{t0}a)}{k_{t0} H_n^{(2)}(k_{t0}a)} G_n \right) M_{\rho} \right] \quad (16b) \end{aligned}$$

where J_{ρ} and M_{ρ} are the ρ -oriented electric and magnetic dipole moments, respectively.

III. GTD SOLUTION

A. Plane Wave Incidence

To evaluate Eq. 7 an assumption is made to simplify the fractions $\frac{J_n'(k_{t1}a)}{J_n(k_{t1}a)}$. By the use of the Debye representation of the Bessel function given in [24] the fractions can be rewritten as:

$$\begin{aligned} \frac{J_n'(k_{t1}a)}{J_n(k_{t1}a)} & \approx \sqrt{1 - \left(\frac{n}{k_{t1}a} \right)^2} \\ & \cdot \tan \left(-k_{t1} a \sqrt{1 - \left(\frac{n}{k_{t1}a} \right)^2} - jn \operatorname{acosh} \left(\frac{n}{k_{t1}a} \right) + \frac{\pi}{4} \right) \\ & \approx j \sqrt{1 - \left(\frac{n}{k_{t1}a} \right)^2} \quad (17) \end{aligned}$$

The first approximation is valid for large n and $k_{t1}a$, but is good for small n as well. The second is valid when the imaginary part of the argument of the tangent function is large. This is the case when the cylinder is opaque, which leads to a large imaginary part of $k_{t1}a$.

By applying the Watson transformation [25] to Eq. 7 with the approximation of Eq. 17 the potentials can be calculated in the deep shadow by the use of the Cauchy residue theorem. Furthermore, the following Fock substitution has been applied [26]:

$$v = k_{t0}a + m_t \tau \quad (18)$$

with $m_t = (k_{t0}a/2)^{1/3}$. The Hankel functions have been approximated by the use of the Fock-Airy functions $W_{1,2}(\tau)$. This is a valid approximation when the order and argument are approximately equivalent. This results in the following expressions for the potentials:

$$\begin{aligned} \begin{bmatrix} A_z^{\text{TM}} \\ F_z^{\text{TE}} \end{bmatrix}^{\pm} & \sim \sum_{p=1}^{\infty} \begin{bmatrix} C_0^{\text{m}} \\ C_0^{\text{e}} \end{bmatrix} \begin{bmatrix} D_p^{\text{m}} \\ D_p^{\text{e}} \end{bmatrix} \sqrt{\frac{k_0\pi}{2j}} \cos \alpha H_v^{(2)}(k_{t0}\rho) \\ & \cdot e^{-jk_0 t \cos^2 \alpha - \alpha_p t} \quad (19a) \end{aligned}$$

$$\begin{aligned} \begin{bmatrix} F_z^{\text{TM}} \\ A_z^{\text{TE}} \end{bmatrix}^{\pm} & \sim \sum_{p=1}^{\infty} \begin{bmatrix} -C_0^{\text{e}} \\ C_0^{\text{m}} \end{bmatrix} D_p^{\text{c}} \sqrt{\frac{k_0\pi}{2j}} \cos \alpha H_v^{(2)}(k_{t0}\rho) \\ & \cdot e^{-jk_0 t \cos^2 \alpha - \alpha_p t} \quad (19b) \end{aligned}$$

where t is the distance the rays travel on the surface of the cylinder. The \pm refers to the direction of travel. The '+' corresponds to counter-clockwise travel where $t = \frac{(\phi - \pi/2)a}{\cos \alpha}$. The '-' corresponds to clockwise travel where $t = \frac{(3\pi/2 - \phi)a}{\cos \alpha}$. Multiple encirclements can be included by dividing with $1 - e^{-jk_0 t 2\pi a - \alpha_p 2\pi a / \cos \alpha}$, which for all relevant situations is approximately equal to 1. The diffraction constants are given by:

$$D_p^{\text{m,e}} = \frac{2\pi m_t^2 \left(\frac{-W_2'(\tau)}{m_t W_2(\tau)} - jq_{\text{e,m}} \sqrt{1 - \left(\frac{k_{t0}a + m_t \tau_p}{k_{t1}a} \right)^2} \right)}{\sqrt{\frac{k_0\pi}{2j}} \cos \alpha D'_W(\tau_p)} \quad (20a)$$

$$D_p^{\text{c}} = \pm \frac{2j\pi m_t^2 q_c(\tau_p)}{\sqrt{\frac{k_0\pi}{2j}} \cos \alpha D'_W(\tau_p)} = \pm \sqrt{-D_p^{\text{m}} D_p^{\text{e}}} \quad (20b)$$

where τ_p is the p^{th} singularity of A_n^{m} , A_n^{e} , and A_n^{c} given by the p^{th} zero of

$$\begin{aligned} D_W(\tau) = & \left(W_2'(\tau) + jm_t q_{\text{e}} \sqrt{1 - \left(\frac{k_{t0}a + m_t \tau}{k_{t1}a} \right)^2} W_2(\tau) \right) \\ & \cdot \left(W_2'(\tau) + jm_t q_{\text{m}} \sqrt{1 - \left(\frac{k_{t0}a + m_t \tau}{k_{t1}a} \right)^2} W_2(\tau) \right) \\ & - [m_t q_c(\tau) W_2(\tau)]^2 \quad (21) \end{aligned}$$

and $D'_W(\tau)$ is the derivative of $D_W(\tau)$ with respect to τ . This

can, at τ_p , be expressed as

$$\begin{aligned}
D'_W(\tau_p) &= \left(\tau_p W_2(\tau_p)^2 - \frac{j m_t^2 q_e \frac{k_{t0} a + m_t \tau_p}{(k_{t1} a)^2}}{\sqrt{1 - \left(\frac{k_{t0} a + m_t \tau_p}{k_{t1} a} \right)^2}} W_2(\tau_p)^2 \right. \\
&- W_2'(\tau_p)^2 \left. \right) \left(\frac{W_2'(\tau_p)}{W_2(\tau_p)} + j m_t q_m \sqrt{1 - \left(\frac{k_{t0} a + m_t \tau_p}{k_{t1} a} \right)^2} \right) \\
&+ \left(\tau_p W_2(\tau_p)^2 - \frac{j m_t^2 q_m \frac{k_{t0} a + m_t \tau_p}{(k_{t1} a)^2}}{\sqrt{1 - \left(\frac{k_{t0} a + m_t \tau_p}{k_{t1} a} \right)^2}} W_2(\tau_p)^2 \right. \\
&- W_2'(\tau_p)^2 \left. \right) \left(\frac{W_2'(\tau_p)}{W_2(\tau_p)} + j m_t q_e \sqrt{1 - \left(\frac{k_{t0} a + m_t \tau_p}{k_{t1} a} \right)^2} \right) \\
&- 2 m_t^2 q_c(\tau_p) q_c'(\tau_p) W_2(\tau_p)^2 \quad (22)
\end{aligned}$$

where the Airy differential equation $W_2''(\tau) - \tau W_2(\tau) = 0$ has been used to simplify the expression. In Eq. 20b the right branch of the square root has to be chosen to ensure that the equal sign is correct. By substitution of n with v and then with $k_{t0} a + m_t \tau$ the expressions for $q_c(\tau)$ and $q_c'(\tau)$ can be found as:

$$q_c(\tau) = \left(1 + \frac{\tau}{2 m_t^2} \right) \frac{k_z}{k_0} \left[1 - \left(\frac{k_{t0}}{k_{t1}} \right)^2 \right] \quad (23a)$$

$$q_c'(\tau) = \frac{1}{2 m_t^2} \frac{k_z}{k_0} \left[1 - \left(\frac{k_{t0}}{k_{t1}} \right)^2 \right] \quad (23b)$$

The attenuation factor is given by

$$\alpha_p = j \frac{m_t \cos \alpha}{a} \tau_p \quad (24)$$

The τ_p 's are found to be approximately located along the line, which originates in origo and makes an angle of -120° with the real axis in the complex plane. Therefore, the α_p 's will have an imaginary part, which will effectively increase the wave number. The wavelength along the cylinder is therefore shorter than the free space wavelength.

B. Infinitesimal Dipole Sources

The same procedure is followed as for the case of plane wave incidence. The expressions for the potentials are simplified by the use of Eq. 17. The Watson transformation is used as well as the Fock substitution from Eq. 18. The integral over k_z is evaluated by the use of the steepest decent method where only the first order approximation in the asymptotic expansion is used. The details of this process are well outlined in [27].

TABLE I
CONSTITUTIVE PARAMETERS OF DIFFERENT TISSUES

Tissue	2.45 GHz		5.8 GHz	
	σ (S/m)	ϵ_r	σ (S/m)	ϵ_r
Muscle [13]	1.74	52.7	4.96	48.5
Skin [13]	1.46	38.0	3.72	35.1
Fat [13]	0.105	5.28	0.293	4.95
Standard [14]	1.8	39.2	5.27	35.3

The result for the potentials caused by a ρ -oriented electric source are given by:

$$\begin{aligned}
A_z &= J_\rho \sqrt{\frac{k_0 \pi}{2j}} \cos \alpha \sqrt{\frac{\pi}{2j k_0 t}} \frac{j k_0}{4\pi} H_v^{(2)}(k_{t0} \rho) e^{-j k_0 t - \alpha_p t} \\
&\cdot \left(\frac{jv}{k_{t0} a} D_p^e H_v^{(2)}(k_{t0} a) + \sin(\alpha) D_p^m H_v^{(2)'}(k_{t0} a) \right) \quad (25a)
\end{aligned}$$

$$\begin{aligned}
F_z &= J_\rho \sqrt{\frac{k_0 \pi}{2j}} \cos \alpha \sqrt{\frac{\pi}{2j k_0 t}} \frac{j k_0 \eta_0}{4\pi} H_v^{(2)}(k_{t0} \rho) e^{-j k_0 t - \alpha_p t} \\
&\cdot \left(\frac{jv}{k_{t0} a} D_p^e H_v^{(2)}(k_{t0} a) - \sin(\alpha) D_p^c H_v^{(2)'}(k_{t0} a) \right) \quad (25b)
\end{aligned}$$

The expressions for the electric and magnetic sources of other orientations have been left out in order to reduce the paper length.

From the potentials the ρ -oriented electric field from a ρ -oriented electric source is calculated and results in:

$$\begin{aligned}
E_\rho &= J_\rho \frac{k_0 \pi}{2j} \cos^2 \alpha \frac{j k_0 \eta_0}{4\pi} \frac{e^{-j k_0 t - \alpha_p t}}{\sqrt{t}} \\
&\left[H_v^{(2)}(k_{t0} \rho) \right. \\
&\cdot \left(\frac{v^2}{k_{t0}^2 a \rho} D_p^e H_v^{(2)}(k_{t0} a) + \frac{jv \sin \alpha}{k_{t0} \rho} D_p^c H_v^{(2)'}(k_{t0} a) \right) \\
&+ H_v^{(2)'}(k_{t0} \rho) \\
&\cdot \left. \left(\frac{jv \sin \alpha}{k_{t0} a} D_p^c H_v^{(2)}(k_{t0} a) + \sin^2 \alpha D_p^m H_v^{(2)'}(k_{t0} a) \right) \right] \quad (26)
\end{aligned}$$

IV. NUMERICAL RESULTS

The eigenfunction solution for the plane wave incidence given in Section II-A has been evaluated numerically. This is done by truncating the summation of Eq. 6. Truncation at $n = k_0 \rho + 20$ yields a sufficient accuracy.

The GTD solution found in Section III-A has also been evaluated. The most challenging part of the evaluation is to find the zeros of Eq. 21. This can be done by different numerical methods as listed in [11]. Here the zeros have been found by a simple algorithm that searches an area around origo in the complex plane to find minimums of error of Eq. 21. When the requested amount of minimums have been found, the error for each minimum is reduced below a threshold by zooming in on each of these. The minimums are then considered to be solutions to the equation. Here the number of zeroes or modes used is four. Two modes are more than

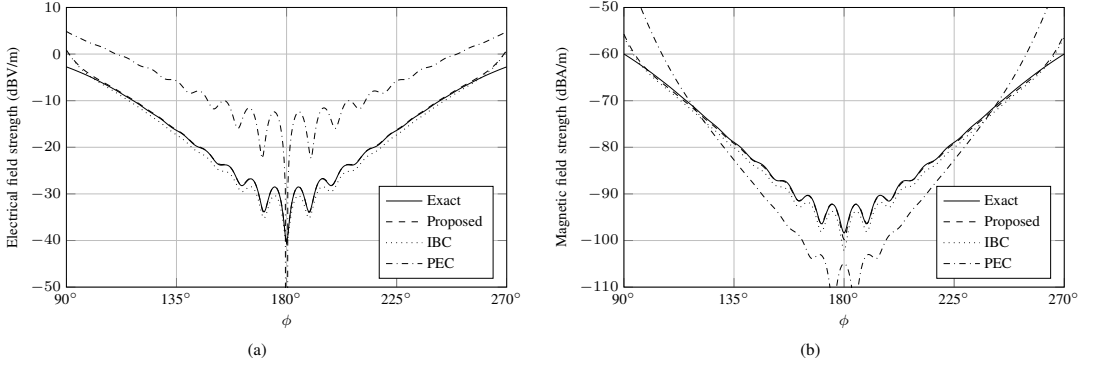


Fig. 3. Field plots for a 'fat' cylinder with $a = 160$ mm and $\alpha = 30^\circ$ at 5.8 GHz. Electric field strength in the TE case (a) and magnetic field strength in the TM case (b).

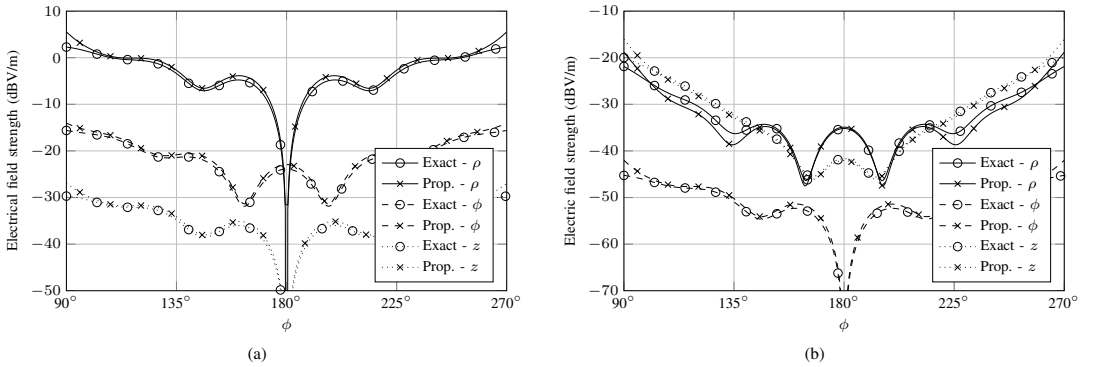


Fig. 4. Field plots for a 'human standard' cylinder with $a = 80$ mm and $\alpha = 10^\circ$ at 2.45 GHz. Electric field strength for each polarization in TE (a) and TM (b) case.

enough in the deep shadow. The error threshold is set to 10^{-8} , but less will do.

In Fig. 3 the proposed approximation has been compared to the exact solution, an IBC approximation and a PEC approximation. The results shown are from a cylinder with radius $a = 160$ mm, incidence angle of $\alpha = 30^\circ$ and constitutive parameters of fat (see Table I). This could be a helix shaped path around the human torso. The solution frequency is 5.8 GHz. The results for the E-fields on the cylinder from a TE incident wave is seen in Fig. 3a. The results for the H-fields on the cylinder from a TM incident wave is seen in Fig. 3b. The H-field has been chosen for the TM wave to enable comparison to the PEC approximation. The E-field on the cylinder in the TM case for a PEC cylinder is zero.

It is clear that the PEC approximation is far from precise. The IBC approximation and proposed approximation are both very close to the exact solution. In the vicinity of the shadow boundary at 90° and 270° they start to drift away from the exact solution as expected. The proposed solution can hardly be distinguished from the exact solution in the deep shadow.

The error is less than 0.2 dB. The IBC approximation has a small visible error, but below 2 dB.

In Fig. 4 the results of the proposed approximation is compared to the exact solution for each of the three polarizations for each of the incident waves. The results are for a cylinder with radius $a = 80$ mm, incidence angle of $\alpha = 10^\circ$, and constitutive parameters as specified by the standard [14] (see Table I). This corresponds to a typical path on the human head. The solution frequency is 2.45 GHz. All polarizations are seen to be modeled well with less than 1 dB of error in the deep shadow. The errors are a bit larger than the results for the 160 mm cylinder at 5.8 GHz since the electrical length of the 80 mm cylinder at 2.45 GHz is close to the limit of an electrically large structure.

To investigate the area of validity for the proposed approximation, the relative root-mean-square error for a sweep of the radius of the cylinder a and the angle of incidence α has been calculated. The relative error RE was calculated as:

$$RE = \frac{|\vec{E}_{\text{exact}} - \vec{E}_{\text{approx}}|}{|\vec{E}_{\text{exact}}|} \quad (27)$$

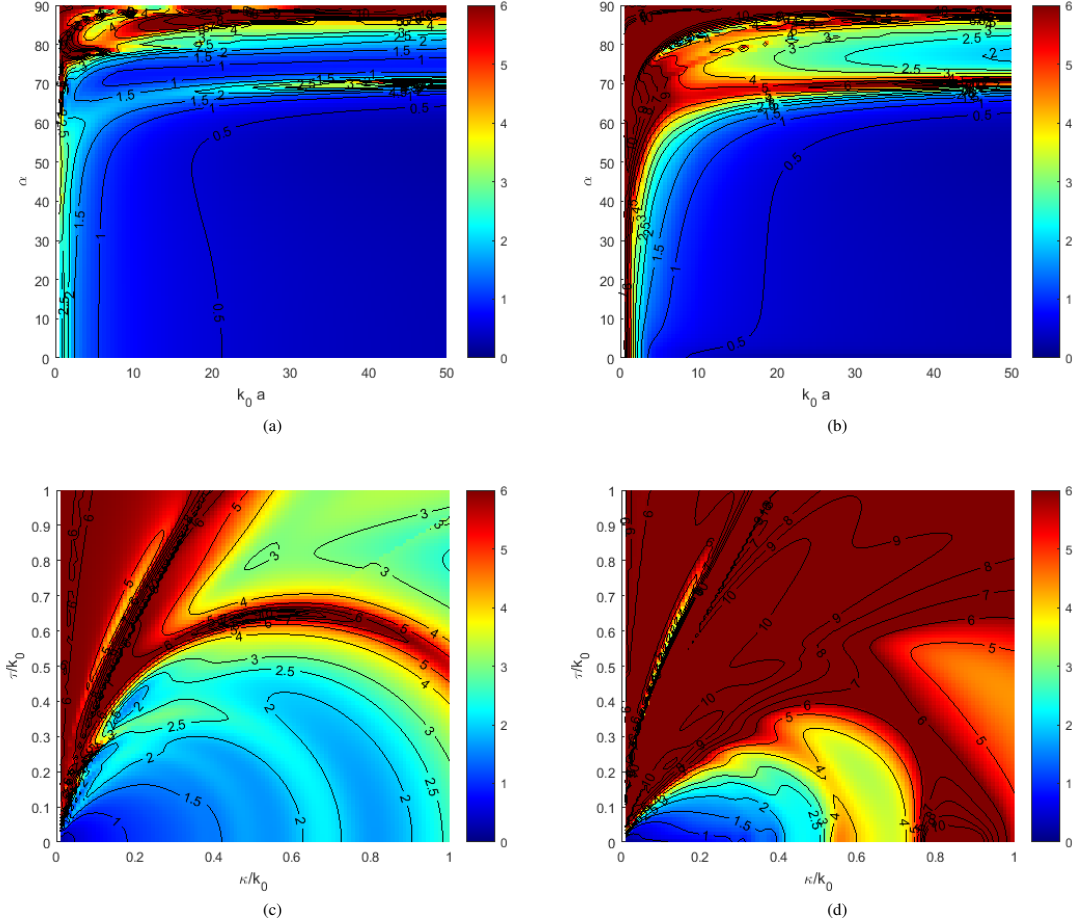


Fig. 5. Root-mean-square of the relative error (from zero (blue) to six (red) decibel) in the electric field in the deep shadow for different cylinders. As a function of the electrical length of the cylinder $k_0 a$ and the angle of incidence α in the TE (a) and TM (b) cases. As a function of the electrical curvature $\frac{\kappa}{k_0}$ and the electrical torsion $\frac{\tau}{k_0}$ in the TE (c) and TM (d) cases.

The relative root-mean-square error was found for the ϕ -angles from 135° to 225° . This is the area where all points are at least 45° into the shadow. The cylinder's constitutive parameters were $\epsilon_r = 39.2$ and $\sigma = 1.8 \text{ S/m}$ as given by the standard [14] for 2.45 GHz. The solution frequency was 2.45 GHz. The decibel value of the RMS-error is shown in Fig. 5. In Fig. 5a and Fig. 5b the error is plotted for the TE and TM cases versus the electrical radius of the cylinder $k_0 a$ and the angle of incidence α . In Fig. 5c and Fig. 5d the error is plotted for the TE and TM cases versus the electrical curvature of the cylinder κ/k_0 and the electrical torsion τ/k_0 .

It is seen that the approximation is precise for large structures at low angles of incidence. A good rule of thumb for the validity could be that $k_0 a > \pi$ or equivalently $a > \lambda_0/2$ and $\alpha < 60^\circ$. If this is converted to general geometric parameters

it corresponds to $\frac{\kappa}{\kappa^2 + \tau^2} > \lambda_0/2$ and $\tau/\kappa < 2$.

V. GTD FORMULATION FOR GENERAL GEOMETRY

The expressions for the diffracted electric and magnetic fields on and away from the cylinder can be described by the use of a few constants. The coupling between the TE and TM mode in air and the modes on the cylinder are given by the square root of D_p^e and D_p^m . This can be realized by using the first order Debye expansion of the Hankel functions in Eq. 19. Thereby the diffracted field \vec{E}^{d} in the deep shadow region away from the cylinder, caused by an incident plane wave \vec{E}^{i} , can be described as:

$$\vec{E}^{\text{d}} \sim \vec{E}^{\text{i}} \cdot \overline{\overline{T}} \frac{e^{-jk_0 s}}{\sqrt{s}} e^{-jk_0 t - \alpha_p t} \quad (28)$$

where

$$\bar{T} \sim \sum_{p=1}^{\infty} \left(\hat{b}' \hat{b} D_p^m + \hat{b}' \hat{n} D_p^c - \hat{n}' \hat{b} D_p^c + \hat{n}' \hat{n} D_p^e \right) \quad (29)$$

where $(\hat{t}', \hat{n}', \hat{b}')$ are the tangential, normal, and binormal unit vectors, respectively, at the source or ingoing grazing point and similarly $(\hat{t}, \hat{n}, \hat{b})$ are the unit vectors at the observation or outgoing grazing point. The shift in sign of D_p^c is explained by the shift of direction of \hat{b} dependent on the way of travel. The equation can be rewritten to:

$$\bar{T} \sim \sum_{p=1}^{\infty} \left(\hat{b}' D_{p,i}^m + \hat{n}' D_{p,i}^e \right) \left(\hat{b} D_{p,o}^m + \hat{n} D_{p,o}^e \right) \quad (30)$$

where the 'i' and 'o' subscript refers to incoming or outgoing waves with respect to the cylinder. The magnitudes of the constants are given by:

$$|D_{p,i}^m| = |D_{p,o}^m| = \left| \sqrt{D_p^m} \right| \quad (31a)$$

$$|D_{p,i}^e| = |D_{p,o}^e| = \left| \sqrt{D_p^e} \right| \quad (31b)$$

where phases are chosen in such a way that:

$$D_{p,i}^m D_{p,o}^m = D_p^m \quad (32a)$$

$$D_{p,i}^m D_{p,o}^e = D_p^c \quad (32b)$$

$$D_{p,i}^e D_{p,o}^m = -D_p^c \quad (32c)$$

$$D_{p,o}^e D_{p,i}^e = D_p^e \quad (32d)$$

The fields on the cylinder from an incident plane wave can be described as well. By evaluating Eq. 19 for points on the surface the so-called attachment coefficients can be determined. In the deep shadow on the cylinder the diffracted fields \bar{E}^d from an incident plane wave \bar{E}^i will be given by:

$$\bar{E}^d \sim \bar{E}^i \cdot \bar{S} e^{-jk_0 t - \alpha_p t} \quad (33)$$

where

$$\bar{S} \sim \sum_{p=1}^{\infty} \left(\hat{b}' D_{p,i}^m + \hat{n}' D_{p,i}^e \right) \left(\hat{t} A_{p,t}^e + \hat{b} A_{p,b}^e + \hat{n} A_{p,n}^e \right) \quad (34)$$

with the attachment coefficient given by (The argument, $k_{t0}a$, of the Hankel functions has been suppressed):

$$A_{p,n}^e = \sqrt{\frac{k_0 \pi}{2j}} \cos \alpha \left(\frac{v}{k_{t0}a} D_{p,o}^e H_v^{(2)} - j \sin \alpha D_{p,o}^m H_v^{(2)'} \right)$$

$$A_{p,b}^e = \sqrt{\frac{k_0 \pi}{2j}} \cos \alpha \left[j \sin \alpha D_{p,o}^e H_v^{(2)'} + \left(1 + \frac{m_t \tau_p \sin^2 \alpha}{k_{t0}a} \right) D_{p,o}^m H_v^{(2)} \right]$$

$$A_{p,t}^e = \sqrt{\frac{k_0 \pi}{2j}} \cos \alpha \left[-j \cos \alpha D_{p,o}^e H_v^{(2)'} - \left(\frac{m_t \tau_p \cos \alpha \sin \alpha}{k_{t0}a} \right) D_{p,o}^m H_v^{(2)} \right] \quad (35)$$

Equivalently the diffracted fields \bar{E}^d in the shadow part of the far-field from a point source \bar{J}_i on the surface can be found by reciprocity to be:

$$\bar{E}^d \sim \frac{jk_0 \eta_0}{4\pi} \bar{J}_i \cdot \bar{U} \frac{e^{-jk_0 t - \alpha_p t}}{\sqrt{t+s}} \frac{e^{-jk_0 s}}{\sqrt{s}} \quad (36)$$

where

$$\bar{U} \sim \sum_{p=1}^{\infty} \left(\hat{t}' L_{p,t}^e + \hat{b}' L_{p,b}^e + \hat{n}' L_{p,n}^e \right) \left(\hat{b} D_{p,o}^m + \hat{n} D_{p,o}^e \right) \quad (37)$$

The launching coefficients are given by:

$$L_{p,n}^e = \sqrt{\frac{k_0 \pi}{2j}} \cos \alpha \left(\frac{v}{k_{t0}a} D_{p,i}^e H_v^{(2)} + j \sin \alpha D_{p,i}^m H_v^{(2)'} \right)$$

$$L_{p,b}^e = \sqrt{\frac{k_0 \pi}{2j}} \cos \alpha \left[j \sin \alpha D_{p,i}^e H_v^{(2)'} - \left(1 + \frac{m_t \tau_p \sin^2 \alpha}{k_{t0}a} \right) D_{p,i}^m H_v^{(2)} \right]$$

$$L_{p,t}^e = \sqrt{\frac{k_0 \pi}{2j}} \cos \alpha \left[-j \cos \alpha D_{p,i}^e H_v^{(2)'} + \left(\frac{m_t \tau_p \cos \alpha \sin \alpha}{k_{t0}a} \right) D_{p,i}^m H_v^{(2)} \right] \quad (38)$$

By the use of the launching and attachment coefficients the field on the cylinder caused by a source \bar{J}_i on the cylinder can be found as:

$$\bar{E}^d \sim \frac{jk_0 \eta_0}{4\pi} \bar{J}_i \cdot \bar{V} \frac{e^{-jk_0 t - \alpha_p t}}{\sqrt{t}} \quad (39)$$

where

$$\bar{V} \sim \sum_{p=1}^{\infty} \left(\hat{t}' L_{p,t}^e + \hat{b}' L_{p,b}^e + \hat{n}' L_{p,n}^e \right) \left(\hat{t} A_{p,t}^e + \hat{b} A_{p,b}^e + \hat{n} A_{p,n}^e \right) \quad (40)$$

The coefficients first determined from the plane wave incidence case matches with the ones from the infinitesimal dipole source case. This can be seen by comparing to Eq. 26.

The behavior of the creeping wave on the body has been described by the use of the unit vectors, which are defined by the geodesic paths. The only thing that remains is to replace a , $\cos \alpha$ and $\sin \alpha$ with expressions not specific to the cylinder. This can be done by the use of:

$$a = \frac{\kappa}{\kappa^2 + \tau^2} \quad (41a)$$

$$\cos \alpha = \frac{\kappa}{\sqrt{\kappa^2 + \tau^2}} \quad (41b)$$

$$\sin \alpha = \frac{-\tau}{\sqrt{\kappa^2 + \tau^2}} \quad (41c)$$

where κ and τ is the surface ray curvature and torsion, respectively. Furthermore, when the term $\frac{1}{\sqrt{t}}$ or $\frac{1}{\sqrt{t+s}}$ appears one should replace it with:

$$\frac{1}{\sqrt{t}} \sqrt{\frac{d\chi_0}{d\chi}} = \sqrt{\frac{d\psi_0}{d\chi}} \quad (42)$$

where $d\chi$ and $d\chi_0$ are the distance between adjacent rays at the observation and source point, respectively. $d\psi_0 = d\chi_0/t$

is the angle between adjacent rays at the source. Finally, the attenuation will be variable over the surface since the curvature and torsion along a geodesic may change for a general geometry contrary to a cylinder. Therefore, the term $\alpha_p t$ should be replaced by $\int_0^t \alpha_p(t') dt'$. From these equations the fields in the proximity of the human body or any opaque lossy dielectric object and in the deep shadow can be determined for any convex geometry.

VI. CONCLUSION

A general geometrical theory of diffraction formulation of the on-body propagation was found. The canonical problem of an infinitely long cylinder was solved. It was done for plane wave incidence as well as for a magnetic or an electric infinitesimal dipole source on the surface of the cylinder. The exact solution was transformed to an asymptotic form valid in the deep shadow region of an opaque electrically large human body or lossy dielectric cylinder with radius a . The model was shown to be valid as long as $a > \lambda_0/2$ and $\alpha < 60^\circ$ or $\frac{\kappa}{\kappa^2 + \tau^2} > \lambda_0/2$ and $\tau/\kappa < 2$. Furthermore, the improvement by the use of this model compared to a PEC approximation of the human body was significant. Especially, for the TM case and torsional cases. The improvement over an IBC model was smaller, but significant for low dielectric constant tissue such as fat. The asymptotic formulation for the cylinder was generalized to any convex geometry. It was shown that the two different excitations of the cylinder resulted in the same generalized constants. Future work could be to solve other canonical geometries to further validate the model. The relevant cases would especially be an ellipsoid and an elliptical cylinder.

REFERENCES

- [1] R. Chandra and A. J. Johansson, "A link loss model for the on-body propagation channel for binaural hearing aids," *IEEE Trans. Antennas Propag.*, vol. 61, no. 12, pp. 6180–6190, 2013.
- [2] E. Plouhinec, B. Uguen, M. Mhedhbi, and S. Avrillon, "3D UTD modeling of a measured antenna disturbed by a dielectric circular cylinder in WBAN context," in *2014 IEEE 79th Vehicular Technology Conference (VTC Spring)*, May 2014, pp. 1–5.
- [3] S. H. Kvist, J. Thaysen, and K. B. Jakobsen, "Ear-to-ear on-body channel model for hearing aid applications," *IEEE Transactions on Antennas and Propagation*, vol. 63, no. 1, pp. 344–352, 2015.
- [4] Y. Zhao, Y. Hao, A. Alomainy, and C. G. Parini, "UWB On-Body Radio Channel Modeling Using Ray Theory and Subband FDTD Method," *IEEE Trans. Microwave Theory Tech.*, vol. 54, no. 4, pp. 1827–1835, Apr 2006.
- [5] R. Chandra and A. J. Johansson, "An Analytical Link-Loss Model for On-Body Propagation Around the Body Based on Elliptical Approximation of the Torso With Arms' Influence Included," *IEEE Antennas Wirel. Propag. Lett.*, vol. 12, pp. 528–531, Apr 2013.
- [6] M. Ghaddar, L. Talbi, and T. A. Denidni, "Human Body Modelling for Prediction of Effect of People on Indoor Propagation Channel," *Electronics Letters*, vol. 40, no. 25, pp. 1592–1594, Dec 2004.
- [7] T. E. P. Alves, B. Poussot, and J.-M. Laheurte, "Analytical Propagation Modeling of BAN Channels Based on the Creeping-Wave Theory," *IEEE Trans. Antennas Propag.*, vol. 59, no. 4, pp. 1269–1274, Apr 2011.
- [8] C. Oliveira and L. M. Correia, "A Statistical Model to Characterize User Influence in Body Area Networks," in *Vehicular Technology Conference Fall (VTC 2010-Fall)*, 2010 IEEE 72nd, Sep 2010.
- [9] N. P. B. Kammersgaard, S. H. Kvist, J. Thaysen, and K. B. Jakobsen, "Validity of PEC approximation for on-body propagation," *2016 10th European Conference on Antennas and Propagation (EuCAP)*, 2016.
- [10] —, "Electromagnetic fields at the surface of human-body cylinders," *Proceedings of the 2016 International Workshop on Antenna Technology*, pp. 170–173, 2016.
- [11] A. G. Aguilar, P. H. Pathak, and M. Sierra-Perez, "A canonical UTD solution for electromagnetic scattering by an electrically large impedance circular cylinder illuminated by an obliquely incident plane wave," *IEEE Transactions on Antennas and Propagation*, vol. 61, no. 10, pp. 5144–5154, 2013.
- [12] A. G. Aguilar, Z. Sipus, and M. Sierra-Perez, "An asymptotic solution for surface fields on a dielectric-coated circular cylinder with an effective impedance boundary condition," *IEEE Transactions on Antennas and Propagation*, vol. 61, no. 10, pp. 5175–5183, 2013.
- [13] S. Gabriel, R. W. Lau, and C. Gabriel, "The Dielectric Properties of Biological Tissues: III. Parametric Models for the Dielectric Spectrum of Tissues," *Physics in Medicine and Biology*, Nov 1996.
- [14] "IEEE recommended practice for determining the peak spatial-average specific absorption rate (SAR) in the human head from wireless communications devices: Measurement techniques," 2013.
- [15] B. R. Levy and J. B. Keller, "Diffraction by a Smooth Object," *Communications on Pure and Applied Mathematics*, vol. 12, no. 1, pp. 159–209, 1959.
- [16] J. R. Wait, "Scattering of a plane wave from a circular dielectric cylinder at oblique incidence," *Canadian Journal of Physics*, vol. 33, no. 5, pp. 189–195, 1955.
- [17] R. F. Harrington, *Time-Harmonic Electromagnetic Fields*. John Wiley & Sons, 2001.
- [18] C. Tokgoz and R. J. Marhefka, "A UTD based asymptotic solution for the surface magnetic field on a source excited circular cylinder with an impedance boundary condition," *IEEE Transactions on Antennas and Propagation*, vol. 54, no. 6, pp. 1750–1757, 2006.
- [19] B. Alisan, V. B. Erturk, and A. Altintas, "Efficient computation of non-paraxial surface fields excited on an electrically large circular cylinder with an impedance boundary condition," *IEEE Transactions on Antennas and Propagation*, vol. 54, no. 9, pp. 2559–2567, 2006.
- [20] P. H. Pathak and R. G. Kouyoumjian, "An analysis of the radiation from apertures in curved surfaces by the geometrical theory of diffraction," *Proceedings of the IEEE*, vol. 62, no. 11, pp. 1438–47, 1438–1447, 1974.
- [21] P. H. Pathak, N. Wang, W. D. Burnside, and R. G. Kouyoumjian, "A uniform gtd solution for the radiation from sources on a convex surface," *IEEE Transactions on Antennas and Propagation*, vol. AP-29, no. 4, pp. 609–22, 609–622, 1981.
- [22] P. H. Pathak and N. Wang, "Ray analysis of mutual coupling between antennas on a convex surface," *IEEE Transactions on Antennas and Propagation*, vol. 29, no. 6, pp. 911–922, 1981.
- [23] A. Fort, F. Keshmiri, G. R. Crusats, C. Craeye, and C. Oestges, "A body area propagation model derived from fundamental principles: Analytical analysis and comparison with measurements," *IEEE Transactions on Antennas and Propagation*, vol. 58, no. 2, pp. 503–514, 2010.
- [24] R. Paknys, "Evaluation of hankel functions with complex argument and complex-order," *IEEE Transactions on Antennas and Propagation*, vol. 40, no. 5, pp. 569–578, 1992.
- [25] G. Watson, "The diffraction of electric waves by the earth," *Proceedings of the Royal Society of London Series A-containing Papers of a Mathematical and Physical Character*, vol. 95, no. 666, pp. 83–99, 1918.
- [26] V. Fock, "Diffraction of radio waves around the earths surface," *Zhurnal Eksperimentalnoi i Teoreticheskoi Fiziki*, vol. 15, no. 9, pp. 479–496, 1945.
- [27] P. H. Pathak and N. Wang, "An analysis of the mutual coupling between antennas on a smooth convex surface," *Final Report 784583-7*, pp. The Ohio State University ElectroScience Lab., Dep. Elec. Eng., 1978.



Nikolaj Peter Brunvoll Kammersgaard received the B.Sc. and M.Sc. degrees in electrical engineering from the Technical University of Denmark, Lyngby, in 2013 and 2014, respectively. Since 2014, he has been affiliated with GN Hearing A/S, a Danish hearing aid manufacturer, where he is currently pursuing an Industrial Ph.D. degree in cooperation with the Technical University of Denmark. His research interests include on-body antennas and propagation, as well as electrically small antennas and physical limitations of antennas. He was awarded the Student

Paper Award for best student paper at the International Workshop on Antenna Technology 2015. In 2015, he was awarded with "Kandidatprisen" from the Danish Association of Engineers (IDA). The award is given to three recently graduated promising electrical engineers for their Master's thesis.



Søren Helstrup Kvist received the B.Sc., M.Sc. and Ph.D. degrees in electrical engineering from the Technical University of Denmark in 2007, 2009 and 2014, respectively. Since 2009 he has been affiliated with GN Hearing A/S, a Danish hearing aid manufacturer, where he is currently employed as manager of the Radio Systems group. His research interests include on-body antennas and propagation, as well as electrically small antennas and physical limitations of antennas. Dr. Kvist was awarded the "Elektroprisen 2015" from the Danish Association

of Engineers (IDA). The award is given for excellent technical and scientific work within electrical engineering.



Jesper Thaysen received the B.Sc., M.Sc. and Ph.D. degrees in electrical engineering from the Technical University of Denmark in 1998, 2000 and 2005, respectively, and an MBA from Middlesex University in 2015. Since 2008 he has been employed at GN Hearing A/S, a Danish hearing aid manufacturer, where he currently acts as the Head of the Global Manufacturing Organization. His research interests include small antennas and on-body antennas and propagation. Dr. Thaysen has overseen more than 40 B.Sc. and M.Sc. students, as well as 3 Ph.D.

students, as the company representative in university-industry cooperative projects.



Kaj Bjarne Jakobsen received the B.Sc.EE and the M.Sc.EE degree from the Technical University of Denmark, Kgs. Lyngby, in 1985 and 1986, respectively, the Ph.D. degree in Electrical Engineering from University of Dayton, Dayton, OH, in 1989, and the HD in Organization and Management, Copenhagen Business School, Copenhagen in 2000. From 1986-1989 he was a Fulbright Scholar at the Department of Electrical Engineering, University of Dayton, OH. Since 1990 he has been with the Department of Electrical Engineering, Technical

University of Denmark, Kgs. Lyngby, where he is Associate Professor. His research interests are in body-centric wireless network, wireless body area network, and body sensor network. He received in 1989 the NCR Stakeholder Award, Ohio, USA, and was appointed Teacher-of-the-Year at the Technical University of Denmark in 1994.

PAPER 3

“IN-THE-EAR CIRCULAR-SHAPED BALANCED INVERTED-A ANTENNA FOR HEARING INSTRUMENTS”

N. P. B. Kammersgaard, S. H. Kvist, J. Thaysen, and K. B. Jakobsen

Published: 2016

[P3] N. P. B. Kammersgaard, S. H. Kvist, J. Thaysen, and K. B. Jakobsen, “In-the-ear circular-shaped balanced inverted-a antenna for hearing instruments”, *IEEE Antennas and Wireless Propagation Letters*, vol. 15, pp. 1839–1843, 2016.

In-the-Ear Circular-Shaped Balanced Inverted-A Antenna for Hearing Instruments

Nikolaj P. B. Kammersgaard, Sren H. Kvist, Jesper Thaysen, and Kaj B. Jakobsen

Abstract—A novel in-the-ear antenna for hearing instruments that operates at 2.45 GHz is presented. The antenna is designed to obtain a polarization perpendicular to the surface of the head in order to optimize the ear-to-ear communication. The antenna consists of a bent dipole with a shorting pin used for impedance matching. It is self-resonant and well matched in the entire Industrial, Scientific, and Medical band from 2.40 to 2.48 GHz. The simulated and measured peak ear-to-ear path gain $|S_{21}|$ is -74.5 and -72.9 dB, respectively. The radiation pattern of the antenna is analyzed, and the implications of the radiation pattern on the ear-to-ear communication are discussed.

Index Terms—Creeping waves, ear-to-ear (E2E), hearing instrument (HI), in-the-ear (ITE), on-body, path gain, wireless body area networks.

I. INTRODUCTION

RESEARCH and applications within on-body communication and wireless body area networks have increased significantly in the last decade. Numerous wireless wearable devices are now available. Within the hearing instrument (HI) industry, wireless connectivity is also in focus. There is an interest in enabling on-body communication between the HIs and wireless wearable devices such as smart phones. This makes it possible to control the HI settings from the phone and to use the HIs as a wireless headset. Off-body communication with, for example, TVs for sound streaming to the HIs is desired as well. Furthermore, wireless on-body ear-to-ear (E2E) communication between the HIs is desired in order to improve their capability to restore hearing.

The Industrial, Scientific, and Medical (ISM) band from 2.40 to 2.48 GHz is especially interesting since it is a worldwide license-free band that enables communication with phones and other wireless devices through Bluetooth. Since it is desirable to have only one radio transceiver in an HI, the ISM band is preferable for all wireless communication needs of the HI. In the ISM band, communication between a wireless off-body device or a wireless wearable device and the HIs is significantly easier

to achieve than on-body E2E communication between the HIs. This is caused by the fact that such wireless devices are often physically larger than HIs and, therefore, offer more efficient antennas and less strict requirements to power consumption. Also, the antennas in these devices do not experience the same near-field losses caused by the human body as antennas in HIs, which are almost completely surrounded by the human tissue. Furthermore, the propagation loss between the HIs alone is more than 40 dB [1]. Therefore, the main focus is to optimize the E2E path gain.

Most antenna research has been focused on behind-the-ear (BTE) HIs. In [2], an antenna for BTE HIs is presented with a path gain $|S_{21}|$ of -52 dB. This antenna concept has also been used for commercial products [3]. For cosmetic and acoustic reasons, many HI users prefer in-the-ear (ITE) HIs instead of BTE HIs. Due to the higher loss from the human tissue experienced by an ITE antenna, the path gain is lower than for BTE antennas. In [4] and [5], antennas for ITE HIs are presented. The best path gain obtained is -89 dB. In [6] and [7], an antenna with a simulated and measured E2E path gain at 2.45 GHz of -85.9 and -82.1 dB, respectively, is presented. The antenna is polarized parallel to the head, which is not optimal for on-body communication. Here, a novel ITE antenna with perpendicular polarization with respect to the surface of the head and improved performance is presented.

In Section II, the theory behind the antenna will be presented. In Section III, the antenna simulation and measurement setup will be presented. In Section IV, the results from the simulation and cabled measurements of a prototype will be presented and discussed. Finally, the conclusion is included in Section V.

II. THEORY

At 2.45 GHz, virtually no energy propagates through the body since the body is very lossy [8]. It has been shown that the energy propagates around the body as creeping waves [9]. Furthermore, it has been shown that the E2E communication channel can be modeled as a number of elliptical paths around the head [10], [11]. In [11], an on-body radiation pattern is introduced and used to estimate the magnitude of the creeping wave launched in different directions. The on-body radiation pattern will be used to evaluate the radiation pattern of the antenna. In [11], only the magnitude is used. Here, the phase of the electric field will be included together with the gain as expressed by the following equation:

$$G_{\text{on-body}}(\phi) = \int_0^\pi G_\theta(\theta, \phi) e^{j\angle E_\theta(\theta, \phi)} \sin\theta d\theta \quad (1)$$

Manuscript received July 10, 2015; revised November 27, 2015 and January 6, 2016; accepted February 6, 2016. Date of publication March 7, 2016; date of current version December 7, 2016.

N. P. B. Kammersgaard is with the Department of Electrical Engineering, Electromagnetic Systems, Technical University of Denmark, 2800 Kgs. Lyngby, Denmark, and also with GN ReSound A/S, 2750 Ballerup, Denmark (e-mail: npivka@elektro.dtu.dk).

S. H. Kvist and J. Thaysen are with GN ReSound A/S, 2750 Ballerup, Denmark (e-mail: skvist@gnsound.com; jthaysen@gnsound.com).

K. B. Jakobsen are with the Department of Electrical Engineering, Electromagnetic Systems, Technical University of Denmark, 2800 Kgs. Lyngby, Denmark (e-mail: kbj@elektro.dtu.dk).

Color versions of one or more of the figures in this letter are available online at <http://ieeexplore.ieee.org>.

Digital Object Identifier 10.1109/LAWP.2016.2538966

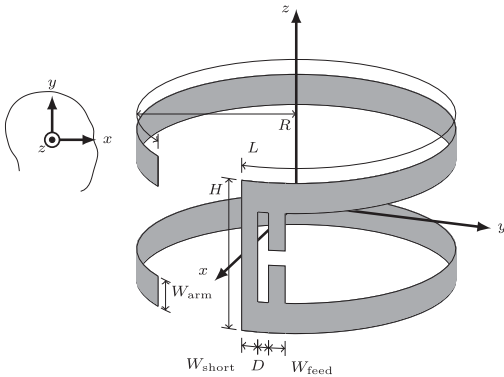


Fig. 1. Circular-shaped balanced inverted-A antenna.

TABLE I
OPTIMIZED ANTENNA DESIGN PARAMETERS

Parameter	Value (mm)
L	29
H	5.0
W_{arm}	1.0
W_{short}	0.60
W_{feed}	0.60
D	0.30
R	5.0

where $G_{\theta}(\theta, \phi)$ is the θ -component of the gain for the antenna mounted on the head, and $E_{\theta}(\theta, \phi)$ is the θ -component of the electric field for the antenna when mounted on the head. The resulting $G_{\text{on-body}}(\phi)$ will thus have a magnitude or “gain” and a phase. It is noted that only the θ -component is used since the ϕ -component of the creeping wave decays much faster. In [12] and [13], it is shown that a perpendicular polarization with respect to the surface of the head is preferable in order to obtain the highest possible path gain. Therefore, the antenna presented here has been designed to obtain perpendicular polarization.

III. EXPERIMENTAL SETUP

The antenna used, an inverted-A antenna, consists of a bent dipole and a shorting pin, as seen in Fig. 1. The dimensions of the antenna are given in Table I. A coordinate system is introduced, where the z -axis is perpendicular to the surface of the head, the xy -plane coincides with the surface of the head, and the x -axis points toward the front of the head. The antenna is symmetric around the xy -plane. Since the antenna is only 5 mm tall, it is completely hidden by the tragus, i.e., the cartilaginous fleshy projection that partially covers the entrance to the external ear, when seen from the front of the head. The total length of the dipole is around a half wavelength at 2.45 GHz. This ensures that the antenna is self-resonant. The antenna has been bent to minimize the size. For half-wave dipole antennas, the highest currents are around the feed. The feed is

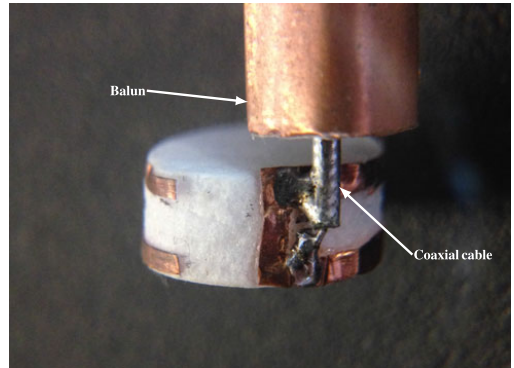
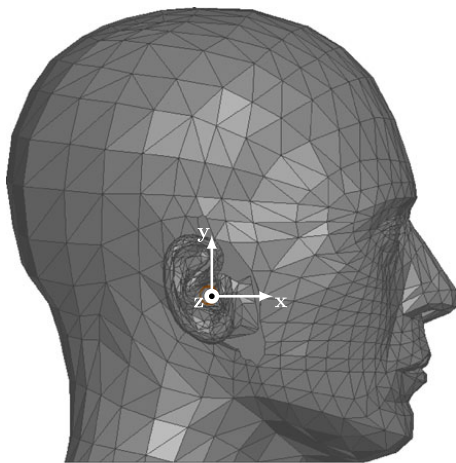


Fig. 2. Fabricated prototype of the circular-shaped balanced inverted-A antenna. The connected coaxial cable and balun are seen at the top.

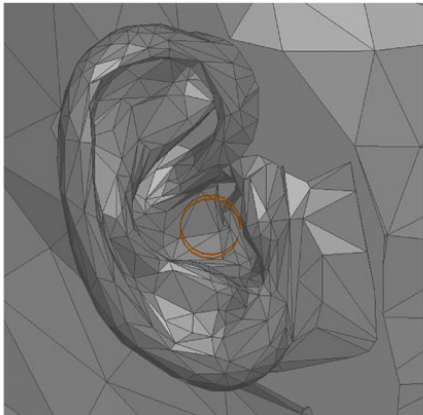
oriented perpendicular to the surface of the head. This ensures that the desired polarization is obtained. The currents on the two arms are opposite, and thus, the electric field cancels in the far field, which leaves only the radiation from the perpendicular current, as desired. The shorting pin has been introduced to match the antenna to 50Ω . The distance between the shorting pin and the feed point of the antenna impedance was adjusted to obtain the desired impedance of 50Ω .

Two prototypes of the antenna were fabricated. One of these can be seen in Fig. 2. The prototype was cut in copper tape (thickness $35 \mu\text{m}$ and $\sigma = 58 \text{ MS/m}$) and was glued onto a dielectric cylinder made of ROHACELL HF ($\epsilon'_r = 1.05$ and $\tan \delta < 0.0002$). The antenna was fed from a coaxial cable, which was fitted with a balun in order to reduce the parasitic currents on the cable. The prototypes were placed in the ear of a test person, and the scattering parameters were measured with a vector network analyzer in a radio anechoic chamber. The antennas were carefully placed with the shorts pointed toward the front of the head to ensure that the coordinate systems of Figs. 1 and 3 align as in the simulation setup. This was done since variations were seen if the antennas were rotated. Furthermore, the antennas were placed in the center of the ear opening with equal distance to the surrounding skin to ensure consistent measurements. Four independent measurements on the test person were done, where the antennas were removed from the ear and placed again. The median measurement with respect to the path gain at 2.45 GHz was used in the results, i.e., the measurement with the third highest path gain at 2.45 GHz. The mean of the four path gains at 2.45 GHz was -70.9 dB , and the mean plus or minus the standard deviation was -69.1 and -74.2 dB .

The simulations were done on the specific anthropomorphic mannequin (SAM), which had been modified with realistic ears. The model can be seen in Fig. 3 with the antenna visible in the ear. The simulations were made in ANSYS HFSS 2014. For the simulations and measurements, a characteristic impedance Z_0 of 50Ω was used.



(a)



(b)

Fig. 3. (a) SAM phantom head with the coordinate system used and (b) a closeup of the realistic ear where the antenna can be seen.

IV. RESULTS AND DISCUSSION

The simulated and measured path gain $|S_{21}|$ can be seen in Fig. 4. The simulated and measured peak E2E path gain is -74.5 and -72.9 dB, respectively. Within the entire ISM band, the simulated and measured E2E path gain is better than -77.8 and -74.4 dB, respectively. As seen in Table II, this is more than 5 dB higher than any other path gains reported in the literature [4]–[7]. The result is directly comparable to that of [6] and [7] since the antenna is contained in the same cylinder and the same experimental setup is used. The main cause of the improved E2E path gain is attributed to the polarization. It is noted that the radiation pattern of the antenna in free space is the same as that of an infinitesimal dipole oriented in the z -direction and, therefore, completely θ -polarized. In the simulation where

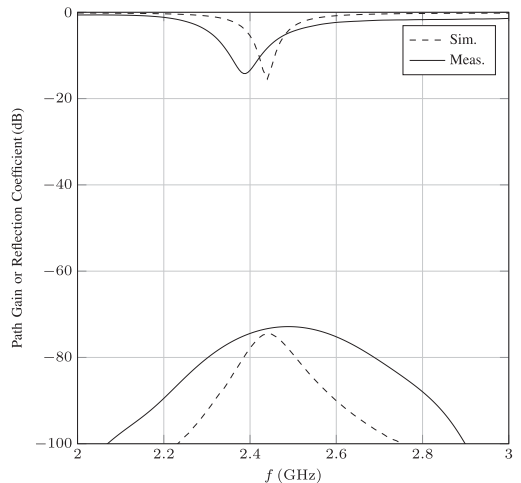


Fig. 4. Simulated (dashed line) and measured (solid line) E2E path gain and reflection coefficient.

TABLE II
COMPARISON TO PREVIOUSLY REPORTED E2E PATH GAINS

Paper	E2E path gain at 2.45 GHz
This work	-74.6 dB
Chandra <i>et al.</i> [4]	-91.7 dB
Huitema <i>et al.</i> [5]	-89 dB / -95 dB*
Kammersgaard <i>et al.</i> [6], [7]	-85.9 dB

*Distance between antennas 160 mm/150 mm.

the antenna is placed inside the ear, the θ polarization is 7.1 dB stronger than the ϕ polarization. This shows that the antenna is polarized as intended. The polarization of [6] and [7] is parallel to the surface of the head. This is believed to be the main cause of the difference in performance between [6], [7], and this work. The simulated and measured reflection coefficient is shown on a logarithmic scale in Fig. 4 and in the Smith chart in Fig. 5. It is seen that the antenna is well matched in the entire ISM band. It is seen from the reflection coefficient and the path gain that the prototype is more broadband. This is due to higher loss in the measurements, and that the balun fitted on the prototype only works in the proximity of 2.45 GHz.

The magnitude of the simulated on-body radiation pattern at 2.45 GHz calculated from (1) is seen in Fig. 6. From the radiation pattern, it is seen that the antenna launches creeping waves primarily toward the back and front of the head. The main wave is toward the front of the head. The phase of the simulated on-body radiation pattern at 2.45 GHz is shown in Fig. 7. There is an electric phase difference between the forward and backward directions of around 155° , which shows that the antenna launches two separate waves. If the radiation pattern is compared to the one in [14], which is for a short dipole of length 4 mm placed in the ear, it is seen that they are almost

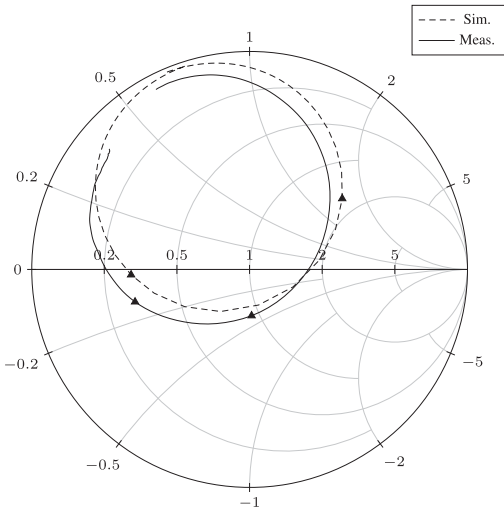


Fig. 5. Smith chart that shows the simulated (dashed line) and measured (solid line) reflection coefficient. The lower and upper frequency in the ISM band are marked by triangles.

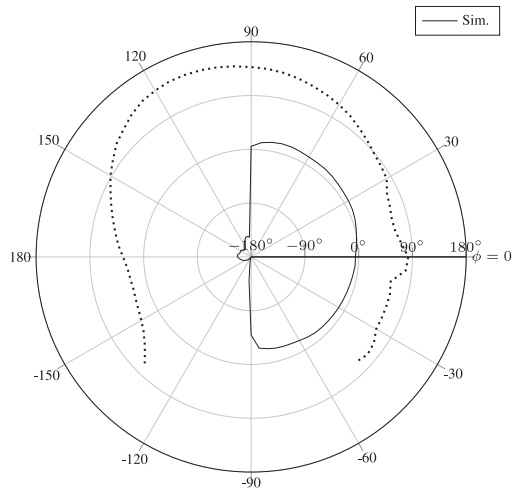


Fig. 7. Phase of the simulated on-body radiation pattern at 2.45 GHz (solid line). The dashed line shows the contour of the head.

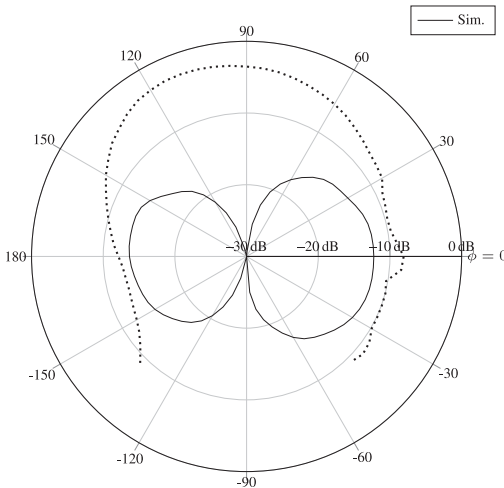


Fig. 6. Magnitude of the simulated on-body radiation pattern at 2.45 GHz (solid line). The dashed line shows the contour of the head.

completely alike. The radiation pattern in [14] is explained by the presence of the pinna, i.e., the outer ear. The gain pattern is also quite similar to that of the ITE antenna presented in [7], which indicates that the shape of the pattern is dominated by the pinna and not the antenna. If the radiation pattern is compared to the radiation pattern in [11, Fig. 6], which is from a proposed BTE antenna, the following is observed. The ITE antenna has lower gain than the BTE antenna, which can be explained by

the position inside the ear. Furthermore, the BTE antenna’s main lobe is toward the back of the head, which is opposite for the ITE antenna. This can be explained by the fact that the pinna is blocking the creeping wave toward the front for the BTE antenna and toward the back for the ITE antenna.

V. CONCLUSION

A novel ITE circular-shaped balanced inverted-A antenna for HIs has been designed, simulated, fabricated, and measured. The antenna is self-resonant due to the near half-wavelength total length. It is well matched to 50 Ω in the ISM band due to the shorting pin. Furthermore, it is polarized perpendicular to the surface of the head in order to optimize the E2E path gain. The antenna yields a peak E2E path gain $|S_{21}|$ of -74.5 and -72.9 dB for the simulation and measurement, respectively. The path gain is significantly higher than previously published results. In the entire ISM band, the E2E path gain $|S_{21}|$ is better than -77.8 and -74.4 dB for the simulation and measurement, respectively.

The on-body radiation pattern of the ITE antenna has been analyzed and compared to the radiation pattern of a BTE antenna. The ITE antenna has two lobes with the main one toward the front of the head, while the BTE antenna has its main lobe toward the back. This is caused by the pinna.

REFERENCES

- [1] T. Alves, B. Poussot, and J. M. Laheurte, “Analytical propagation modeling of BAN channels based on the creeping-wave theory,” *IEEE Trans. Antennas Propag.*, vol. 59, no. 4, pp. 1269–1274, Apr. 2011.
- [2] S. H. Kvist, S. Özden, J. Thaysen, and K. B. Jakobsen, “Improvement of the ear-to-ear path gain at 2.45 GHz using parasitic antenna element,” in *Proc. 6th Eur. Conf. Antennas Propag.*, 2012, pp. 944–947.

- [3] GN ReSound A/S. (Aug. 2014). *ReSound Verso*. [Online]. Available: <http://www.resound.com/products/hearing-aids/resound-verso>
- [4] R. Chandra and A. J. Johansson, "Miniaturized antennas for link between binaural hearing aids," in *Proc. 32nd Annu. Int. Conf. IEEE Eng. Med. Biol. Soc.*, Aug. 2010, pp. 688–691.
- [5] L. Huitema, S. Sufyar, C. Delaveaud, and R. D'Errico, "Miniature antenna effect on the ear-to-ear radio channel characteristics," in *Proc. 6th Eur. Conf. Antennas Propag.*, 2012, pp. 3402–3406.
- [6] N. P. I. Kammersgaard, S. H. Kvist, J. Thaysen, and K. B. Jakobsen, "In-the-ear spiral monopole antenna for hearing instruments," *Electron. Lett.*, vol. 50, no. 21, pp. 1509–1510, 2014.
- [7] N. P. I. Kammersgaard, S. H. Kvist, J. Thaysen, and K. B. Jakobsen, "Body-worn spiral monopole antenna for body-centric communications," in *Proc. 2015 Int. Workshop Antenna Technol.*, Seoul, South Korea, Mar. 2015, pp. 107–110.
- [8] S. Gabriel, R. W. Lau, and C. Gabriel, "The dielectric properties of biological tissues: III. Parametric models for the dielectric spectrum of tissues," *Phys. Med. Biol.*, vol. 41, pp. 2271–2293, 1996.
- [9] J. Ryckaert, P. De Doncker, R. Meys, A. de Le Hoye, and S. Donnay, "Channel model for wireless communication around human body," *Electron. Lett.*, vol. 40, no. 9, pp. 543–544, Apr. 2004.
- [10] R. Chandra and A. J. Johansson, "A link loss model for the on-body propagation channel for binaural hearing aids," *IEEE Trans. Antennas Propag.*, vol. 61, no. 12, pp. 6180–6190, Dec. 2013.
- [11] S. H. Kvist, J. Thaysen, and K. B. Jakobsen, "Ear-to-ear on-body channel model for hearing aid applications," *IEEE Trans. Antennas Propag.*, vol. 63, no. 1, pp. 344–352, Jan. 2015.
- [12] P. S. Hall *et al.*, "Antennas and propagation for on-body communication systems," *IEEE Antennas Propag. Mag.*, vol. 49, no. 3, pp. 41–58, Jun. 2007.
- [13] S. H. Kvist, J. Thaysen, and K. B. Jakobsen, "Polarization of unbalanced antennas for ear-to-ear on-body communications at 2.45 GHz," in *Proc. Loughborough Antennas Propag. Conf.*, Loughborough, U.K., Oct. 2011, pp. 1–4.
- [14] N. P. I. Kammersgaard, S. H. Kvist, J. Thaysen, and K. B. Jakobsen, "Pinna model for hearing instrument applications," in *Proc. Loughborough Antennas Propag. Conf.*, Loughborough, U.K., Nov. 2014, pp. 141–143.

PAPER 4

“BODY-WORN ANTENNAS FOR BODY-CENTRIC WIRELESS COMMUNICATIONS”

N. P. I. Kammersgaard, S. H. Kvist, S. Özden, J. Thaysen, and K. B. Jakobsen

Published: 2014

[P4] N. P. I. Kammersgaard, S. H. Kvist, S. Özden, J. Thaysen, and K. B. Jakobsen, “Body-worn antennas for body-centric wireless communications”, in *Proceedings of 2014 Loughborough Antennas and Propagation Conference*, IEEE, 2014, pp. 2–6.

Body-Worn Antennas for Body-Centric Wireless Communications

(Invited Paper)

Nikolaj P. I. Kammersgaard*[†], Søren H. Kvist[†], Sinasi Özden[†], Jesper Thaysen[†], and Kaj B. Jakobsen*

*Department of Electrical Engineering, Electromagnetic Systems, Technical University of Denmark, Ørstedes Plads, Building 348, DK-2800 Kgs. Lyngby, Denmark

*kbj@elektro.dtu.dk, *[†]s110371@student.dtu.dk

[†]GN ReSound A/S, Lautrupbjerg 7, DK-2750 Ballerup, Denmark

[†]skvist@, jthaysen@, siozden@gnresound.com

Abstract—Ear-to-ear (E2E) on-body propagation and on-body antennas for body-centric wireless communications are presented.

I. INTRODUCTION

Body-centric wireless communications have received much attention in the literature in recent years. This is due to the rise of small body-worn devices, which need to communicate wirelessly in order to offer improved functionality to the user. The Industrial, Scientific and Medical (ISM) band at 2.4 GHz is license free worldwide, and is therefore used to enable many Wireless Body Area Network (WBAN) applications. Additionally, all modern mobile phones are already equipped to communicate at 2.4 GHz by the use of the widespread Bluetooth[®] protocol.

Hearing Instruments (HIs) are a good example of such small body-worn devices, that have become increasingly advanced in recent years. Modern top-line HIs are thus expected to be able to communicate wirelessly with mobile accessories, such as audio streamers and mobile phones. Furthermore, the binaurally fitted HIs are needed to communicate wirelessly with each other, ear-to-ear, in order to synchronize the amplification settings between the HIs. Further, it is possible to obtain audiological advantages, which, e.g. eases conversation in noisy areas. In order to conserve power, the accessory-link and the ear-to-ear link need to utilize the same radio and antenna. The challenge in using 2.4 GHz is that the head is lossy at these frequencies, with a skin depth $\delta_s \approx 21$ mm [1], [2]. Therefore, the energy cannot propagate through the head. Instead the energy propagates around the head as creeping waves [2], [3].

The HIs can be classified in four main types, see Fig. 1. The Behind-The-Ear (BTE) and the Receiver-In-the-Ear (RIE) HIs sit behind the ear, as shown in Fig. 1a and Fig. 1b, respectively. The In-The-Ear (ITE) and In-The-Canal (ITC) types are custom-made to fit the individual ear canals, and are shown in Fig. 1c and Fig. 1d, respectively. Common to all four types is that they are generally made as small as possible, in an effort to conceal the devices.

The early work on body-worn antennas and propagation

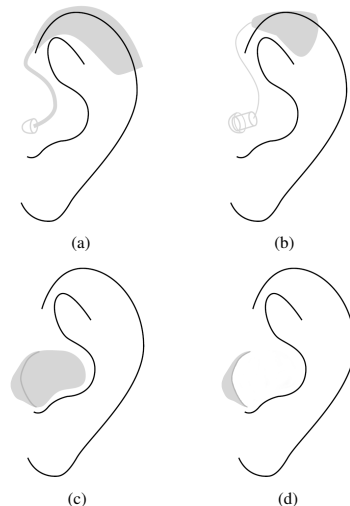


Fig. 1. The hearing instrument (HI) types in the use position for Behind-the-Ear (BTE) (a), Receiver-in-the-Ear (RIE) (b), In-the-Ear (ITE) (c), and the smaller versions of the ITE, the In-the-Canal (ITC) and Completely-in-the-Canal (CIC) (d) [2].

mainly involved off-body antennas and propagation, for use with devices such as mobile phones. These handsets and their antennas were rather large, since size was dictated by other components than the antenna. By comparison, today's body-worn devices are vanishingly small; A development that is driven by the availability of ever smaller electronic components. Thus, due to their small size compared to the wavelength at 2.4 GHz, the HIs can be viewed almost as point sources, which can be leveraged as a vehicle to explore the on-body propagation.

In this presentation, the characteristics of the ear-to-ear on-body propagation will be reviewed. Additionally, some of the many examples of body-worn antennas found in the literature will be reviewed, e.g., [4]–[23], including some that

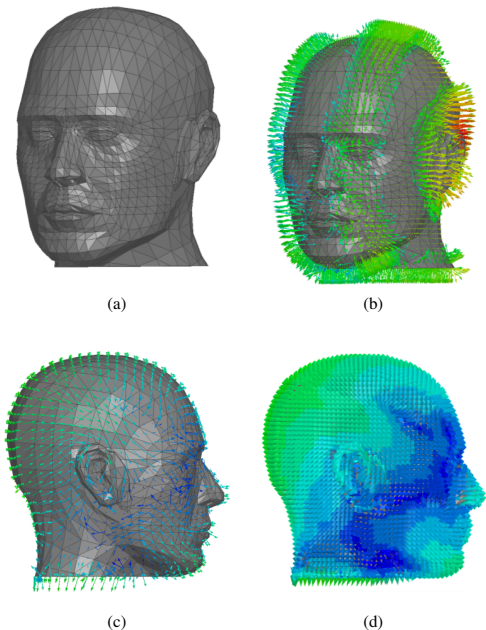


Fig. 2. The SAM head with ears (a) and electric field vectors (b) and Poynting vector showing the direction (c) and the interference pattern (d) [24], [25], [26].

are suitable for use in small body-worn devices, such as HIs.

II. EAR-TO-EAR ON-BODY PROPAGATION

The 2.4 GHz ear-to-ear propagation effects have been investigated in [25], [26], where the ear-to-ear on-body path gain was measured on the Specific Anthropomorphic Mannequin (SAM) head model. It was shown that the electromagnetic waves creep around the head along different paths, and combine in an interference pattern that determines the ear-to-ear path gain. To illustrate the creeping waves, a realistic SAM head with ears was used and a small antenna was placed behind each ear [24]. The SAM head and the simulated electric field that is radiated from the antenna are shown in Fig. 2a and 2b, respectively. The electric field vectors are seen to be normal to the surface of the head and the creeping waves are seen to propagate along the surface of the head. Two plots of the Poynting vector a few millimeters above the head is shown for two vector arrow sizes to illustrate the orientation along the head surface and the interference pattern, see Fig. 2c and Fig. 2d, respectively. Thus, the on-body propagation can propagate along multiple paths around the human body, to combine in a pattern of constructive or destructive interference, which in general will depend on the shape of the body, the position of the antenna, and the on-body radiation pattern of the antenna.

To find the attenuation experienced by the wave as it creeps around the head, it is modelled as a series of elliptical

cylinders. The attenuation for one path is [27], [28]

$$W = e^{-L}, \quad (1)$$

where L is the complex attenuation in neper on an elliptical PEC cylinder given by [29]

$$L = \sqrt[3]{\frac{k_0}{2} \left(\frac{3\pi ab}{8}\right)^2} e^{\frac{j\pi}{6}} \int_{\varphi_1}^{\varphi_2} \frac{ab}{(a^4 \cos^2 \varphi + b^4 \sin^2 \varphi)(a^2 \cos^2 \varphi + b^2 \sin^2 \varphi)} d\varphi, \quad (2)$$

where a is the major axis and b is the minor axis of the elliptical cylinder, φ_1 and φ_2 are the angles on the elliptical cylinder and the angle that the waves creeps on the cylinder is $\varphi_2 - \varphi_1$ thus the path length d that the wave travels along the surface of the elliptical cylinder head is [29], [30]

$$d = ab \int_{\varphi_1}^{\varphi_2} \sqrt{\frac{a^4 \cos^2 \varphi + b^4 \sin^2 \varphi}{(a^2 \cos^2 \varphi + b^2 \sin^2 \varphi)^3}} d\varphi. \quad (3)$$

The waves that creep around the head can then be modeled as a sum of N waves that each travel along an elliptical path n on the head of path length d_n . The ear-to-ear on-body path gain $\frac{P_R}{P_T}$ can then be expressed as [30]

$$\frac{P_R}{P_T} = \frac{\lambda_0^2}{4\pi^2} \left| \frac{2\pi}{\alpha_N - \alpha_1} \sum_{n=1}^N \frac{\sqrt{G_{T,n} G_{R,n}} e^{-L_n} e^{-jk_0 d_n}}{d_n} \Delta\alpha \right|^2, \quad (4)$$

where λ_0 and k_0 are the wavelength and wave number in free space, respectively. Each of the creeping waves are weighted by the on-body gain that is associated with the n^{th} path for the transmitter and the receiver antenna, $G_{T,n}$ and $G_{R,n}$, respectively. The N creeping wave contributions to the received signal are then weighted by $\Delta\alpha$ and added, which is essentially a numerical integration over the angle α . In [30] it is shown that an accurate model can be obtained for $N = 50$ paths.

III. ON-BODY ANTENNAS

Body-worn antennas can be classified into on-body and off-body antennas. To obtain a high on-body path gain ($|S_{21}|$) the on-body antenna is to radiate such that the electric field is perpendicular to the surface of the body, see Fig. 3b. This will ensure an efficient launch of a creeping wave [3], [31]–[33]. Further, the antenna should radiate along the surface of the body. Many on-body antennas have been presented in the literature, e.g., [4]–[9], [15], [24], [34]–[36]. However, to be useful, e.g., in HIs, the antenna must be physically small in order to fit the devices—but not necessarily electrically small at 2.4 GHz.

The on-body antennas can be realized as either unbalanced or balanced antennas. Five examples are shown in Fig. 4 and 5, respectively. In Fig. 4a and 4b are shown two unbalanced antennas, a straight monopole antenna that rests on top of

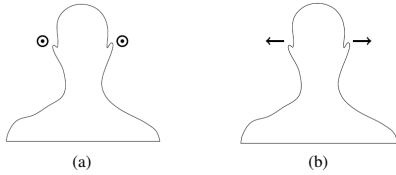


Fig. 3. Hearing-instrument antenna configurations. HI antennas oriented parallel (a) and perpendicular (b) to the head [37].

the ear and a meandered monopole antenna that is fed at the center of the side of the ground plane. Two examples of balanced antennas are shown in Fig. 4c and 4d, respectively; one antenna with two parallel, circular plates, see Fig. 4c; and one with two parallel rings, see Fig. 4d. A magnetic dual, a meandered slot loop is shown in Fig. 5. In Fig. 6 is shown the current distribution on the unbalanced monopole shown in Fig. 4a. It is seen that the current runs tangentially to the head, high and low current density is shown in red and blue, respectively. In Fig. 7 is shown a prototype of the on-body antenna in Fig. 4c fitted with a balun.

It was shown in [30] that an on-body radiation pattern that optimizes the ear-to-ear on-body path gain can be synthesized. The radiation pattern synthesis is shown in Fig. 8. The on-body radiation pattern was synthesized as a weighted sum of the first six spherical wave mode expansion coefficients, Q_j , in order to emulate an electrically small antenna. The mode weights were found by the use of a genetic algorithm in combination with the ear-to-ear path gain model described above. The optimization was converged after 100 iterations of the genetic algorithm, see Fig. 8a. The weights of the spherical wave expansion coefficients, Q_j , are shown in Fig. 8b. The synthesized on-body radiation pattern is shown in Fig. 8c, with the orientation of the SAM head indicated by the dotted line.

IV. CONCLUSION

Ear-to-ear on-body propagation has been reviewed with illustrations of creeping waves on a realistic specific anthropomorphic mannequin (SAM) head with ears. A theoretical model for the E2E on-body path gain was presented. Different types of on-body antennas have been presented along with an on-body radiation pattern that is synthesized by the use of spherical wave expansion in order to optimize the E2E on-body path gain.

REFERENCES

- [1] P. S. Hall and Y. Hao, *Antennas and propagation for body-centric wireless communications*. Artech House, Inc. Norwood, MA, USA, 2006.
- [2] S. H. Kvist, *Antennas and Propagation for Body-Centric Wireless Communications*. Ph.D. dissertation, DTU Elektro, Technical University of Denmark (DTU), Kgs. Lyngby, Denmark, ISBN 978-87-92465-47-4, 2013.
- [3] P. S. Hall, Y. Nechayev, and L. Akhoondzadeh-Asl, "Surface and creeping waves excitation by body-worn antennas," *2010 Loughborough Antennas and Propagation Conference, LAPC 2010*, pp. 48–51, 2010.
- [4] G. A. Conway and W. G. Scanlon, "Antennas for over-body-surface communication at 2.45 GHz," *IEEE Transactions on Antennas and Propagation*, vol. 57, no. 4, pp. 844–855, 2009.

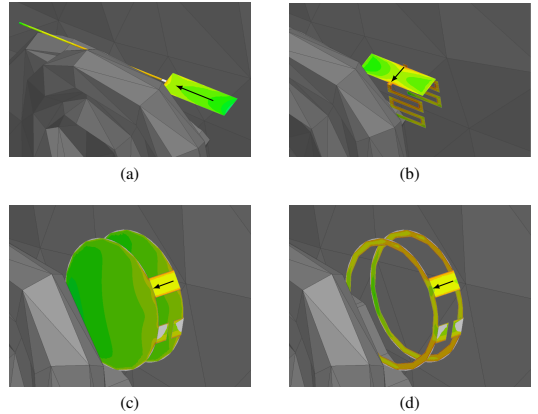


Fig. 4. On-body antenna types shown with simulated surface current distributions. Two types of unbalanced antennas, a straight monopole antenna that rests on top of the ear (a) and a meandered monopole antenna that is fed at the center of the side of the ground plane (b). Two types of balanced antennas, one antenna with two parallel, circular plates (c) and one with two parallel rings (d) [2], [35].



Fig. 5. Meandered slot loop on-body antenna type. The rectangular battery compartment is shown in white in the center [36].

- [5] G. A. Conway, S. L. Cotton, and W. G. Scanlon, "An antennas and propagation approach to improving physical layer performance in wireless body area networks," *IEEE Journal on Selected Areas in Communications*, vol. 27, no. 1, pp. 27–36, 2009.
- [6] N. Chahat, M. Zhadobov, L. Le Coq, and R. Sauleau, "Wearable endfire textile antenna for on-body communications at 60 GHz," *IEEE Antennas and Wireless Propagation Letters*, vol. 11, pp. 799–802, 2012.
- [7] Q. Bai and R. Langley, "Crumpling of PIFA textile antenna," *IEEE Transactions on Antennas and Propagation*, vol. 60, no. 1, pp. 63–70, 2012.
- [8] T. Alves, R. Augustine, P. Queffelec, M. Grzeskowiak, B. Pousot, and J. M. Laheurte, "Polymeric ferrite-loaded antennas for on-body

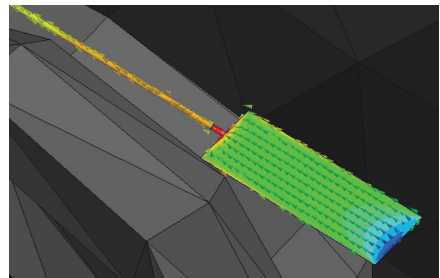
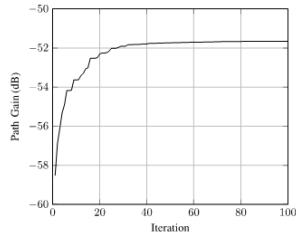


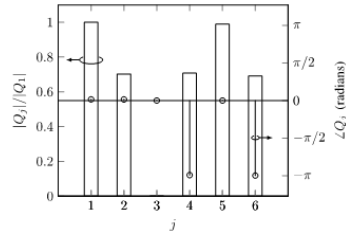
Fig. 6. Current distribution on the body-worn antenna shown in Fig. 4a [38].



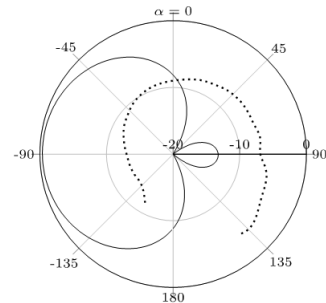
Fig. 7. Prototype of the on-body antenna shown in Fig. 4c [34].



(a)



(b)



(c)

Fig. 8. Path gain convergence of the genetic algorithm with a genome of the first 6 spherical wave mode weights (a) and the spherical wave expansion coefficients, Q_j , after 100 iterations of the genetic algorithm (b). Synthesized on-body radiation pattern such that the ear-to-ear on-body path gain is optimized. The orientation of the SAM head is indicated by the dotted line (c) [2].

communications," *Microwave and Optical Technology Letters*, vol. 51, no. 11, pp. 2530–2533, 2009.

[9] L. Akhondzadeh-Asl, Y. Nechayev, P. S. Hall, and C. C. Constantinou, "Parasitic array antenna with enhanced surface wave launching for on-body communications," *IEEE Transactions on Antennas and Propagation*, vol. 61, no. 4, pp. 1976–1985, 2013.

[10] C.-H. Lin, K. Saito, M. Takahashi, and K. Ito, "A compact planar inverted-F antenna for 2.45 GHz on-body communications," *IEEE Transactions on Antennas and Propagation*, vol. 60, no. 9, pp. 4422–4426, 2012.

[11] A. M. Faiz, T. Alves, B. Poussot, and J. M. Laheurte, "Diversity antenna combining slot-loop DRA for BAN applications," *Electronics Letters*, vol. 48, no. 1, pp. 7–8, 2012.

[12] B. Sanz-Izquierdo, J. A. Miller, J. C. Batchelor, and M. I. Sobhy, "Dual-band wearable metallic button antennas and transmission in body area networks," *IET Microwaves Antennas and Propagation*, vol. 4, no. 2, pp. 182–190, 2010.

[13] S. Rao, N. Llobart, E. Moradi, K. Koski, T. Bjorninen, L. Sydanheimo, J. M. Rabaey, J. M. Carmenta, Y. Rahmat-Samii, and L. Ukkonen, "Antenna applications corner: miniature implantable and wearable on-body antennas: Towards the new era of wireless body-centric systems," *IEEE Antennas and Propagation Magazine*, vol. 56, no. 1, pp. 271–291, 2014.

[14] G. Fontgalland, U. Olgun, and J. L. Volakis, "Low-profile vertically polarized printed antenna for body-worn applications," *2013 IEEE Antennas and Propagation Society International Symposium (APSURSI)*, pp. 986–986, 2013.

[15] A. K. Skrivervik, D. D. Cara, J. Trajkovikj, and J.-F. Zurcher, "Compact UWB antennas for wireless body area networks (W-BANs)," *2014 IEEE-APS Topical Conference on Antennas and Propagation in Wireless Communications (APWC)*, pp. 125–128, 2014.

[16] J. Bringquier, R. Mittra, and K. Yoo, "Modeling and design of wideband antennas for body area networks (BANs)," *IEEE Region 10 Annual International Conference, Proceedings/TENCON*, 2007.

[17] W. G. Whittow, C. C. Njoku, and Y. C. Vardaxoglou, "Fine scale simulations of patch antennas with heterogeneous substrates," *2013 USNC-URSI Radio Science Meeting (Joint with AP-S Symposium)*, p. 223, 2013.

[18] A. Bisognin, J. Thielieux, W. Wei, D. Titz, F. Ferrero, P. Brachat, G. Jacquemod, H. Happy, and C. Luxey, "Inkjet coplanar square monopole on flexible substrate for 60 GHz applications," *IEEE Antennas and Wireless Propagation Letters*, vol. 13, pp. 435–438, 2014.

[19] L. K. Larsen, S. H. Kvist, W. H. Yatman, J. Thaysen, and K. B. Jakobsen, "Mini-remote-control antenna for on-body wireless communication systems," *2012 Loughborough Antennas and Propagation Conference*, 2012.

[20] A. Ruaro, J. Thaysen, S. Glstrhoff, K. B. Jakobsen, and S. H. Kvist, "Influence of the antenna impedance variation and input matching network Q on LNA key figures," *LAPC 2012 - 2012 Loughborough Antennas and Propagation Conference*, 2012.

[21] S. Pehrson, S. H. Kvist, K. B. Jakobsen, and J. Thaysen, "Morphological investigation of the differences on the ear-to-ear path gain and the packet loss at 2.45 GHz," *34th Annual Antenna Measurement Techniques Association Symposium 2012*, pp. 43–48, 2012.

[22] P. F. Medina, S. H. Kvist, K. B. Jakobsen, and J. Thaysen, "Transmit and receive diversity in body-centric wireless communications," *34th Annual*

Antenna Measurement Techniques Association Symposium 2012, pp. 38–42, 2012.

[23] S. H. Kvist and K. B. Jakobsen, "Investigation of the chest-ear radio propagation channel," *EuCAP 2010 - the 4th European Conference on Antennas and Propagation*, p. 5505460, 2010.

[24] S. H. Kvist, S. zden, J. Thaysen, and K. B. Jakobsen, "Improvement of the ear-to-ear path gain at 2.45 GHz using parasitic antenna element," *2012 6th European Conference on Antennas and Propagation*, pp. 944–947, 2012.

[25] S. H. Kvist, J. Thaysen, and K. B. Jakobsen, "Investigation of the ear-to-ear radio propagation channel," in *European Conference on Antennas and Propagation*, 2011, pp. 3796–3800.

[26] S. Kvist, J. Thaysen, and K. B. Jakobsen, "The effect of the head size on the ear-to-ear radio-propagation channel for body-centric wireless

- networks," in *Loughborough Antennas & Propagation Conference*, 2010, pp. 345–348.
- [27] R. Chandra and A. J. Johansson, "An elliptical analytic link loss model for wireless propagation around the human torso," *Proceedings of 6th European Conference on Antennas and Propagation, EuCAP 2012*, pp. 3121–3124, 2012.
- [28] —, "A link loss model for the on-body propagation channel for binaural hearing aids," *IEEE Transactions on Antennas and Propagation*, vol. 61, no. 12, pp. 6180–6190, 2013.
- [29] C. A. Balanis and J. Peters, L., "Aperture radiation from an axially slotted elliptical conducting cylinder using geometrical theory of diffraction," *IEEE Transactions on Antennas and Propagation*, vol. AP-17, no. 4, pp. 507–513, 1969.
- [30] S. H. Kvist, J. Thaysen, and K. B. Jakobsen, "Ear-to-ear on-body channel model for hearing aid applications," *IEEE Transactions on Antennas and Propagation*, accepted 2014.
- [31] P. Hall, Y. Hao, Y. Nechayev, A. Alomainy, C. Constantinou, C. Parini, M. Kamarudin, T. Salim, D. Hee, R. Dubrovka, A. Owadally, W. Song, A. Serra, P. Nepa, M. Gallo, and M. Bozzetti, "Antennas and propagation for on-body communication systems," *IEEE Antennas and Propagation Magazine*, vol. 49, no. 3, pp. 41–58, 2007.
- [32] L. Akhondzadeh-Asl, P. S. Hall, and Y. Nechayev, "Wave excitation on human body by a short dipole," *EuCAP 2010 - the 4th European Conference on Antennas and Propagation*, 2010.
- [33] P. S. Hall, Y. I. Nechayev, and M. R. Kamarudin, "Antennas for on-body communication systems," *Proceedings - 2005 IEEE International Workshop on Antenna Technology: Small Antennas and Novel Metamaterials, IWAT 2005*, vol. 2005, pp. 17–20, 2005.
- [34] S. H. Kvist, K. B. Jakobsen, and J. Thaysen, "Design and measurement of a 2.45 GHz on-body antenna optimized for hearing instrument applications," *34th Annual Antenna Measurement Techniques Association Symposium 2012*, pp. 33–37, 2012.
- [35] N. P. I. Kammersgaard, S. H. Kvist, J. Thaysen, and K. B. Jakobsen, "In-the-ear spiral monopole antenna for hearing instruments," *Electronics Letters*, vol. 50, no. 21, 2014 (accepted).
- [36] W. H. Yatman, L. K. Larsen, S. H. Kvist, J. Thaysen, and K. B. Jakobsen, "In-the-ear hearing-instrument antenna for ISM-band body-centric ear-to-ear communications," *LAPC 2012 - 2012 Loughborough Antennas and Propagation Conference*, pp. 1–4, 2012.
- [37] S. H. Kvist, J. Thaysen, and K. B. Jakobsen, "Time-domain measurement of the ear-to-ear on-body path gain at 2.45 GHz in a radio anechoic environment," *Loughborough Antennas & Propagation Conference (LAPC)*, 2012.
- [38] —, "Polarization of unbalanced antennas for ear-to-ear on-body communications at 2.45 GHz," *Loughborough Antennas & Propagation Conference*, pp. 1–4, 2011.

PAPER 5

“OFF-BODY TRANSMISSION RANGE IMPROVEMENT FOR HEARING INSTRUMENTS BY THE USE OF EAR-TO-EAR COMMUNICATION”

N. P. B. Kammersgaard, S. H. Kvist, J. Thaysen, and K. B. Jakobsen

Published: 2015

[P5] N. P. B. Kammersgaard, S. H. Kvist, J. Thaysen, and K. B. Jakobsen, “Off-body transmission range improvement for hearing instruments by the use of ear-to-ear communication”, in *Proceedings of 2015 Loughborough Antennas & Propagation Conference*, IEEE, 2015.

Off-Body Transmission Range Improvement for Hearing Instruments by the Use of Ear-to-Ear Communication

Nikolaj P. B. Kammersgaard*[†], Søren H. Kvist[†], Jesper Thaysen[†] and Kaj B. Jakobsen*
 npivka@elektro.dtu.dk, skvist@gnresound.com, jthaysen@gnresound.com, kbj@elektro.dtu.dk

*Department of Electrical Engineering, Electromagnetic Systems, Technical University of Denmark,
 Ørstedes Plads, Building 348, DK-2800 Kgs. Lyngby, Denmark

[†]GN ReSound A/S, Lautrupbjerg 7, DK-2750 Ballerup, Denmark

Abstract—A novel idea for improving the off-body transmission range for hearing instruments is presented. The idea is to use the ear-to-ear communication to improve the range. If one of the hearing instruments loses the connection to an off-body accessory it can reestablish the connection through the other hearing instrument. The median improvement of the measured and simulated gain of the hearing instrument is 9.7 dB and 7.0 dB, respectively. This corresponds to a transmission range improvement of 204% and 123% under free-space conditions and 74% and 49% if a ground reflection is assumed.

I. INTRODUCTION

Wireless Body Area Networks (WBAN) have been researched a lot during the last decade. WBAN is wireless communication between electronic devices where at least one of them are located on or in the body. The communication can be classified into *on-body*, *off-body* and *in-body* using the terminology of [1]. WBAN is used in numerous applications such as smart phones, smart watches, smart glasses, and medical applications such as implants and monitoring. Within the hearing instrument (HI) industry WBAN is also used. The purpose has been to enable off-body communication with accessories and ear-to-ear (E2E) on-body communication between the HIs, since this can improve the usability and acoustic performance. The focus has been on the Industrial, Scientific and Medical (ISM) band at 2.45 GHz. At 2.45 GHz the body tissue is very lossy [2]. This means that the electromagnetic energy can not propagate through the head, but instead propagates around the head as creeping waves [3]. Therefore, the major challenge has been to enable E2E communication since it depends on the creeping waves around the head. In [4] and [5] it has been shown that E2E communication is possible to achieve, for HIs placed behind the ear (BTE) and in the ear (ITE).

The off-body communication with accessories is relatively easier to achieve. The communication is in free-space and the accessory radio system is often more powerful and less in contact with the body. This is especially the case when it is line-of-sight (LOS) conditions. When there is no-line-of-sight (NLOS) conditions, i.e., the head is located between the HI

and the accessory the communication link has a much shorter transmission range.

The purpose of the work is to improve the transmission range under NLOS conditions. The idea is to do this by the use of E2E communication. If a HI is under NLOS conditions and loses the link with the accessory, it can simply reestablish the link through the other HI by the use of the E2E communication. This means that the link of HI in NLOS conditions will be improved to the level of the link of the HI in LOS conditions. The implementation of this technique is purely software related.

A measured and simulated cut of the radiation pattern of an ITE antenna is presented. The radiation pattern is analyzed to quantify the possible improvements by the use of the E2E communication to improve the off-body transmission range.

II. THEORY

The improvements will be analyzed when free-space propagation and when a reflection from a smooth planar surface is assumed. In the first case Friis transmission equation given in Eq. 1 will be used.

$$\frac{P_R}{P_T} = \frac{G_R G_T \lambda^2}{(4\pi d)^2}, \quad (1)$$

where P_R and P_T are the received and transmitted power, G_R and G_T are the gains of the receiving and transmitting antenna, λ is the wavelength and d is the distance between the antennas. If a minimal required received power is assumed $P_{R,\min}$ the range R can be calculated as the maximum distance d as given by Eq. 2.

$$R = \frac{\lambda}{4\pi} \sqrt{\frac{P_T G_R G_T}{P_{R,\min}}}, \quad (2)$$

A reflection from a smooth planar ground is assumed where the receiving and transmitting antennas are located at a height of h_R and h_T , respectively and $d \gg \frac{4h_T h_R}{\lambda}$ the transmission formula is given in Eq. 3 [6].

$$\frac{P_R}{P_T} = \frac{G_R G_T (h_R h_T)^2}{d^4}, \quad (3)$$

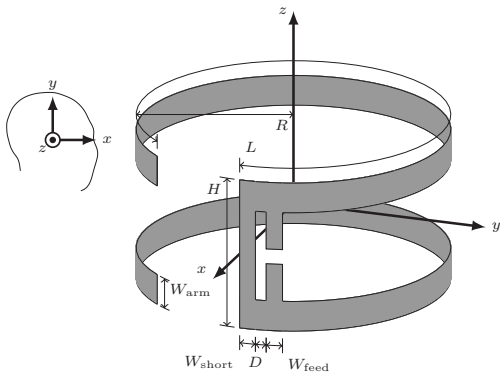


Fig. 1. The circular-shaped balanced inverted-A antenna.

TABLE I
ANTENNA DESIGN PARAMETERS

Parameter	Value (mm)
L	29
H	5.0
W_{arm}	1.0
W_{short}	0.60
W_{feed}	0.60
D	0.30
R	5.0

which gives the range seen in Eq. 4, i.e.,

$$R = \sqrt[4]{\frac{P_T G_R G_T (h_R h_T)^2}{P_{R,\min}}}. \quad (4)$$

III. EXPERIMENTAL SETUP

For the simulations and measurements a circular-shaped balanced inverted-A antenna was used. The antenna can be seen in Fig. 1 and the design parameters in Table I. The antenna is presented in detail in [7]. The antenna was placed in the concha in the right ear for the measurements and simulations.

Simulations were done using ANSYS HFSS 2014. The Specific Anthropomorphic Mannequin (SAM) fitted with realistic ears was used. The head and ears were given homogeneous electrical parameters of $\epsilon_r = 50$ and $\tan\delta = 0.5$. The antenna was modeled as copper. The simulation setup can be seen in Fig. 3. It is noted that the coordinate systems in Fig. 1 and Fig. 3 coincided.

The prototype used for the measurements can be seen in Fig. 2. ROHACELL[®] HF ($\epsilon_r = 1.05$ and $\tan\delta < 0.0002$) was used to support the antenna. The antenna was fed from a coaxial cable. The cable was fitted with a balun to reduce the currents on the cable. For the same reason the cable was bend so that it was running on the skin of the test person.

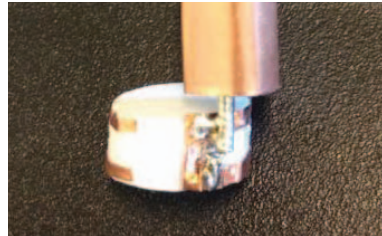


Fig. 2. The fabricated prototype of the circular-shaped balanced inverted-A antenna. The connected coaxial cable and balun are seen at the top.

TABLE II

Assumption	Median transmission range improvement, $\frac{\Delta R}{R}$	
Free-space	204%	123%
Smooth planar ground	74%	49%

The measurements were done in a radio anechoic chamber intended for radiation pattern measurements. The test person was seated on a chair and was rotated in steps of 10° . In that way the XZ-cut in the radiation pattern was measured.

IV. RESULTS AND DISCUSSION

The measured and simulated radiation pattern in the XZ-plane are shown in Fig. 4 and Fig. 5, respectively. It is seen that the absolute level is around 5 dB higher for the measurement than the simulation. The relative differences between the gain in different directions is quite similar for the measurement and simulation although the measurement shows deeper nulls on the opposite side of the head than the HI. These differences are caused by the fact that for the measurements a human head is used and for the simulations the SAM head is used. Since these are not completely alike it will cause some differences. The positioning of the antenna for the measurement is very hard to make precise, which can also cause some differences. See for example in [8] where it was shown that the efficiency changes with two decibels per millimeter the antenna is moved out of the head. Finally, the presence of the cable might have changed the measurements slightly. The important observation is that the measurement and simulation both show large differences in gain dependent on whether it is on the same side of the head as the HI or on the opposite. This is also clear from the simulated 3D radiation pattern seen in Fig. 6. The gain towards the negative z-direction is seen to have large variation and deep nulls caused by interference between different creeping-wave paths around the head.

The radiation pattern of the antenna mounted on the left side of the head is assumed to be a mirror version of the radiation pattern of the one on the right side. The radiation pattern in the XZ-plane, when the best of the right and left gain is used, is shown in Fig. 7. A large improvement in the gain is seen. A similar improvement will be experienced for

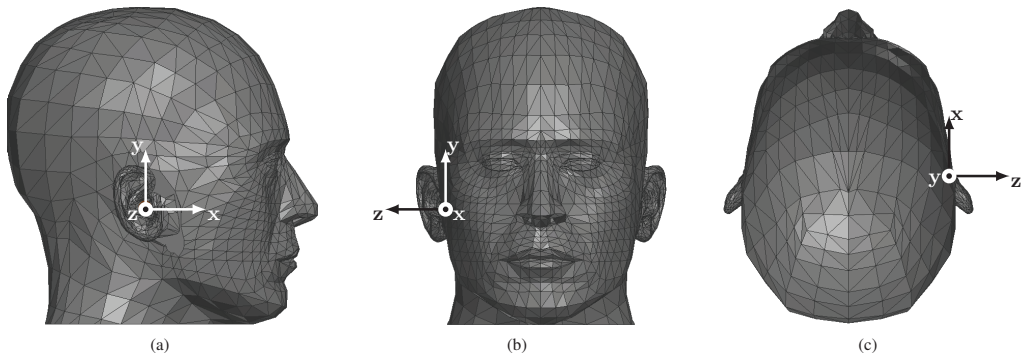


Fig. 3. The SAM phantom head seen from the side (a), front (b) and top (c).

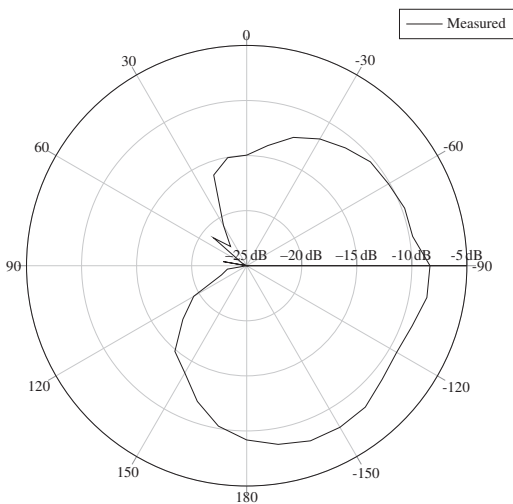


Fig. 4. Measured radiation pattern in the XZ-plane. The nose points towards the front and the antenna is in the right ear. The angle denotes the angle between the x-axis and the nose.

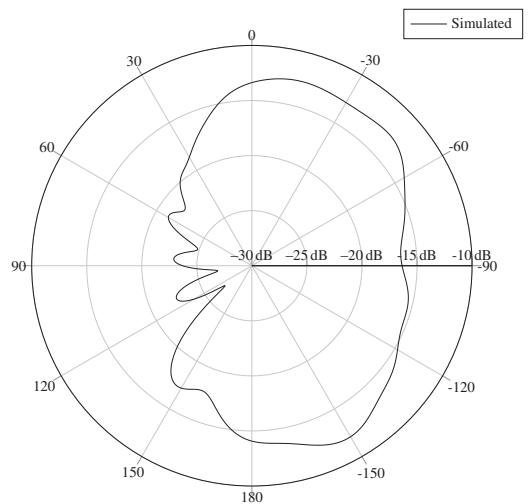


Fig. 5. Simulated radiation pattern in the XZ-plane. The nose points towards the front and the antenna is in the right ear. The angle denotes the angle between the x-axis and the nose.

the left side. The median gain improvement for the antenna on the right side in NLOS conditions by the use of the gain of the antenna on the left side is 9.7 dB and 7.0 dB measured and simulated, respectively. The same will be the case for the antenna on the left side. If the median gain improvement is inserted into Eq. 2 it is found that a median transmission range improvement, $\frac{\Delta R}{R}$ of 204% and 123% is achieved under free-space assumptions. Similarly when Eq. 4 is used it is found that a median transmission range improvement of 74% and 49% is achieved when reflection from a smooth planar ground is assumed. These are the transmission range improvements for when the off-body links will fail when E2E communication is used. Without the E2E communication when moving away from the accessory one of the off-body links will fail and then

later the other. With the E2E communication both will fail at the latter distance.

Further work could be to study the effect of E2E communication use in order to improve the off-body transmission range or stability in a multi-scattering environment. Furthermore, if the HI radios are coherent, the actual received signal could be transmitted between the HIs, which allows for the use of advanced diversity schemes.

V. CONCLUSION

A novel method to improve the off-body transmission range for hearing instruments has been presented. Measured and simulated radiation patterns have been used to analyze the

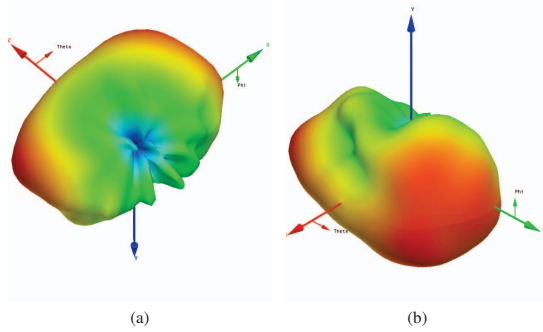


Fig. 6. 3D simulated radiation pattern from two angles. The color scale ranges from -10 dB (red) to -30 dB (blue) gain.

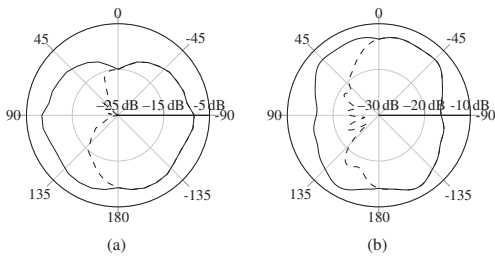


Fig. 7. Improved measured (a) and simulated (b) radiation pattern in the XZ-plane, when the E2E communication is used to improve the gain (solid lines) and the original gains (dashed lines).

possible improvements by the use of the ear-to-ear communication to improve the off-body link. The median gain improvement measured and simulated was 9.7 dB and 7.0 dB, respectively. This corresponds to a median improvement of the transmission range before the off-body link starts to fail of 204% and 123% under free-space assumptions, respectively; and 74% and 49% with a smooth planar ground, respectively. This demonstrates how the ear-to-ear communication, besides usability and acoustic performance improvement in hearing instruments, can improve the off-body transmission range significantly.

REFERENCES

- [1] P. S. Hall and Y. Hao, Eds., *Antennas and Propagation for Body-Centric Wireless Communications*. Norwood, MA, USA: Artech House, 2006.
- [2] S. Gabriel, R. W. Lau, and C. Gabriel, "The dielectric properties of biological tissues: III. Parametric models for the dielectric spectrum of tissues." *Physics in medicine and biology*, vol. 41, pp. 2271–2293, 1996.
- [3] J. Ryckaert, P. De Doncker, R. Meys, A. de Le Hoye, and S. Donnay, "Channel Model for Wireless Communication Around Human Body," *Electronics Letters*, vol. 40, no. 9, pp. 543–544, Apr. 2004.
- [4] S. H. Kvist, S. Özden, J. Thaysen, and K. B. Jakobsen, "Improvement of the Ear-to-Ear Path Gain at 2.45 GHz Using Parasitic Antenna Element," in *6th European Conference on Antennas and Propagation (EuCAP)*, Prague, Czech Republic, Apr. 2012, pp. 944–947.
- [5] N. P. I. Kammersgaard, S. H. Kvist, J. Thaysen, and K. B. Jakobsen, "In-the-ear spiral monopole antenna for hearing instruments," *Electronics Letters*, vol. 50, no. 21, pp. 1509–1511, Oct. 2014.
- [6] R. Vaughan and J. B. Andersen, *Channels, Propagation And Antennas For Mobile Communications*, ser. IEE Electromagnetic Waves Series. London, UK: The Institution of Electrical Engineers, 2003, no. 50.
- [7] N. P. I. Kammersgaard, S. H. Kvist, J. Thaysen, and K. B. Jakobsen, "In-the-Ear Circular-Shaped Balanced Inverted-A Antenna for Hearing Instruments," *Submitted to IEEE Antennas and Wireless Propagation Letters*, 2015.
- [8] —, "Pinna Model for Hearing Instrument Applications," 2014, pp. 141 – 143.

PAPER 6

“VALIDITY OF PEC APPROXIMATION FOR ON-BODY PROPAGATION”

N. P. B. Kammersgaard, S. H. Kvist, J. Thaysen, and K. B. Jakobsen

Published: 2016

[P6] N. P. B. Kammersgaard, S. H. Kvist, J. Thaysen, and K. B. Jakobsen, “Validity of PEC approximation for on-body propagation”, in *Proceedings of Eucap 2016*, EurAPP, 2016.

Validity of PEC Approximation for On-Body Propagation

Nikolaj P. B. Kammersgaard*, Søren H. Kvist†, Jesper Thaysen† and Kaj B. Jakobsen*

npivka@elektro.dtu.dk, skvist@gnresound.com, jthaysen@gnresound.com, kbj@elektro.dtu.dk

*Department of Electrical Engineering, Electromagnetic Systems, Technical University of Denmark, Ørstedss Plads, Building 348, DK-2800 Kgs. Lyngby, Denmark

†GN ReSound A/S, Lautrupbjerg 7, DK-2750 Ballerup, Denmark

Abstract—Many articles on on-body propagation assumes that the human body can be approximated by a perfect electric conductor (PEC) instead of the actual constitutive parameters of the human body, which is that of a lossy dielectric. This assumption is investigated in this article through comparison of the scattering of a plane wave at oblique incidence by a PEC and a lossy dielectric cylinder. The investigation shows that the validity of the assumption depends on the polarization of the plane wave, the angle of incidence, and the region of interest.

I. INTRODUCTION

The area of on-body propagation has been of high interest in recent years. Wireless communications for on-body devices serves as one of the enabling factors in the emerging commercial area of wearables.

Numerous investigations have been made on the on-body propagation and many models have been proposed. In many of these the body is approximated by a perfect electric conductor (PEC) of some shape, [1]–[5]. Often these models justify directly or indirectly this assumption based on [6]. But since [6] is concerned only with the disturbance in the channel between two off-body antennas this seems to be a poor validation.

The purpose of this work is to investigate if modeling the body as a PEC is a valid assumption. Furthermore, if the assumption might be valid under certain other assumptions.

The on-body propagation will be investigated by the use of the exact solution to the fields around an infinitely long cylinder. The fields will be calculated for a PEC cylinder and for a human body average cylinder. The material parameters of the human body are documented in [7]. The average material parameters in [8] is used ($\epsilon_r = 39.2$ and $\sigma = 1.8\text{ S/m}$). The cylinder has a radius of $a = 80\text{ mm}$, which is similar to the radius of the leg or the radius of the head. The fields are calculated for both TM and TE polarization and at three different angles of incidence.

II. THEORY

The infinitely long lossy dielectric cylinder is located in free space. A plane wave is incident and propagating in the direction given by $\hat{d} = (0, \sin \alpha, \cos \alpha)$ as seen in Fig. 1. The propagation constant in the cylinder and in free space

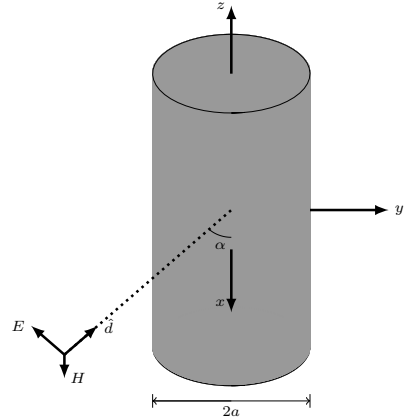


Fig. 1. The geometry of the infinitely long dielectric cylinder model.

are k_1 and k , respectively. Two other propagation constants are defined as $k' = k \sin \alpha$ and $k'_1 = \sqrt{k_1^2 - k^2 \cos^2 \alpha}$. The electric and magnetic fields outside the cylinder incident by a transverse magnetic (TM) plane wave are given by the following formulas obtained from [9], [10]:

$$E_\rho = -jk \cos \alpha \frac{\partial u}{\partial \rho} - \frac{j\mu\omega}{\rho} \frac{\partial v}{\partial \phi} \quad (1)$$

$$E_\phi = -\frac{jk \cos \alpha}{\rho} \frac{\partial u}{\partial \phi} + j\mu\omega \frac{\partial v}{\partial \rho} \quad (2)$$

$$E_z = k'^2 u \quad (3)$$

$$H_\rho = \frac{jk^2}{\mu\omega\rho} \frac{\partial u}{\partial \phi} - jk \cos \alpha \frac{\partial v}{\partial \rho} \quad (4)$$

$$H_\phi = -\frac{jk^2}{\mu\omega} \frac{\partial u}{\partial \rho} - \frac{jk \cos \alpha}{\rho} \frac{\partial v}{\partial \phi} \quad (5)$$

$$H_z = k'^2 v \quad (6)$$

where a common factor of $e^{-jkz \cos \alpha}$ has been suppressed as well as a time dependency of $e^{j\omega t}$. To obtain E_ρ and E_ϕ inside the cylinder the permeability μ must be replaced by

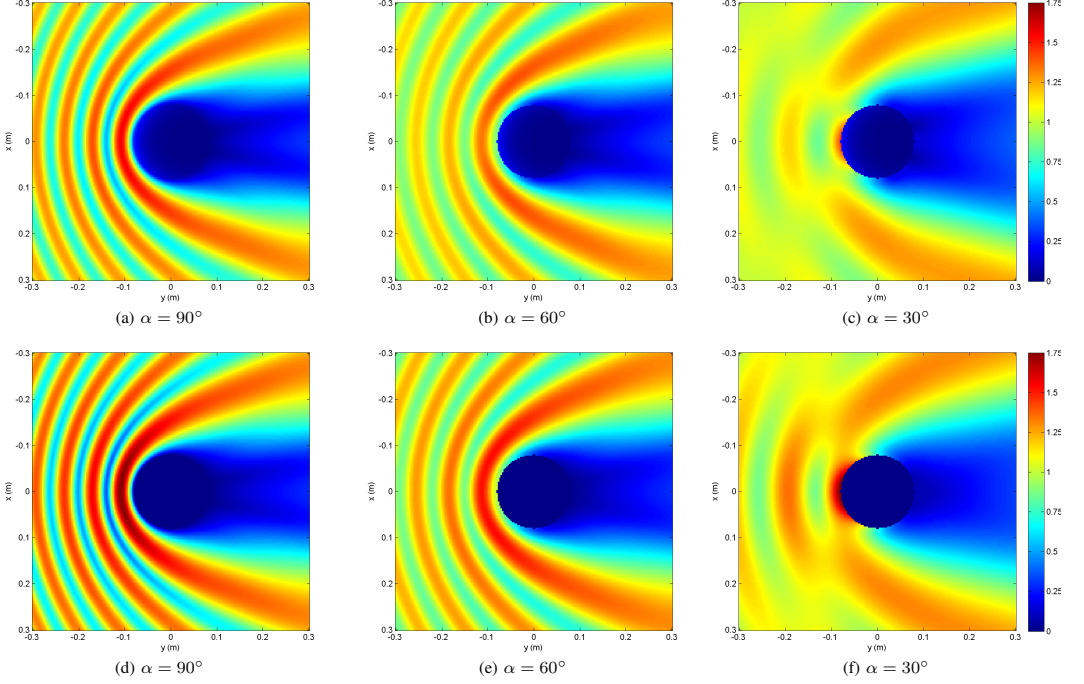


Fig. 2. Electric field strength (V/m) plot for TM plane wave incident on a human-body average (a, b, c) and PEC (d, e, f) cylinder at different angles.

μ_1 . To obtain E_z and H_z inside the cylinder the propagation constant k' must be replaced by k'_1 . To obtain H_ρ and H_ϕ inside the cylinder μ and k must be replaced by μ_1 and k_1 in the terms involving u and remain the same for the terms involving v . For $\rho > a$ the scalar potentials u and v are given by [9]:

$$u = \frac{-E_0 \sin \alpha}{k'^2} \sum_{n=-\infty}^{\infty} \left(J_n(k'\rho) - a_n H_n^{(2)}(k'\rho) \right) e^{-jn\phi} \quad (7)$$

$$v = \frac{-E_0 \sin \alpha}{k'^2} \sum_{n=-\infty}^{\infty} c_n H_n^{(2)}(k'\rho) e^{-jn\phi} \quad (8)$$

and for $\rho < a$ by:

$$u = \frac{-E_0 \sin \alpha}{k'^2} \sum_{n=-\infty}^{\infty} b_n J_n(k'_1 \rho) e^{-jn\phi} \quad (9)$$

$$v = \frac{-E_0 \sin \alpha}{k'^2} \sum_{n=-\infty}^{\infty} d_n J_n(k'_1 \rho) e^{-jn\phi} \quad (10)$$

where a_n, b_n, c_n , and d_n are constants chosen to ensure the continuity of the tangential components of the E-fields and

H-fields across the boundary. The constants are given by:

$$a_n = \frac{J_n(k'a)}{\Delta H_n^{(2)}} \left\{ \left[\frac{\mu_1 J'_n(k'_1 a)}{\mu k'_1 a J_n(k'_1 a)} - \frac{1}{k'a} \frac{H_n^{(2)'}(k'a)}{H_n^{(2)}(k'a)} \right] \cdot \left[\frac{k_1^2}{k^2} \frac{\mu}{\mu_1 k'_1 a} \frac{J'_n(k'_1 a)}{J_n(k'_1 a)} - \frac{1}{k'a} \frac{J'_n(k'a)}{J_n(k'a)} \right] - \left[\frac{1}{(k'a)^2} - \frac{1}{(k'_1 a)^2} \right]^2 n^2 \cos^2 \alpha \right\} \quad (11)$$

$$b_n = \frac{k'^2}{k_1'^2} \left[J_n(k'a) - a_n \frac{H_n^{(2)}(k'a)}{J_n(k'_1 a)} \right]$$

$$c_n = -\frac{2kn \cos \alpha}{\Delta \mu \omega \pi (k'a)^2} \frac{1}{H_n^{(2)}(k'a)} \left[\frac{1}{(k'a)^2} - \frac{1}{(k'_1 a)^2} \right]$$

$$d_n = \frac{k'^2}{k_1'^2} c_n \frac{H_n^{(2)}(k'a)}{J_n(k'_1 a)}$$

where

$$\Delta = \left[\frac{\mu_1 J'_n(k'_1 a)}{\mu k'_1 a J_n(k'_1 a)} - \frac{1}{k'a} \frac{H_n^{(2)'}(k'a)}{H_n^{(2)}(k'a)} \right] \cdot \left[\frac{k_1^2}{k^2} \frac{\mu}{\mu_1 k'_1 a} \frac{J'_n(k'_1 a)}{J_n(k'_1 a)} - \frac{1}{k'a} \frac{H_n^{(2)'}(k'a)}{H_n^{(2)}(k'a)} \right] - \left[\frac{1}{(k'a)^2} - \frac{1}{(k'_1 a)^2} \right]^2 n^2 \cos^2 \alpha.$$

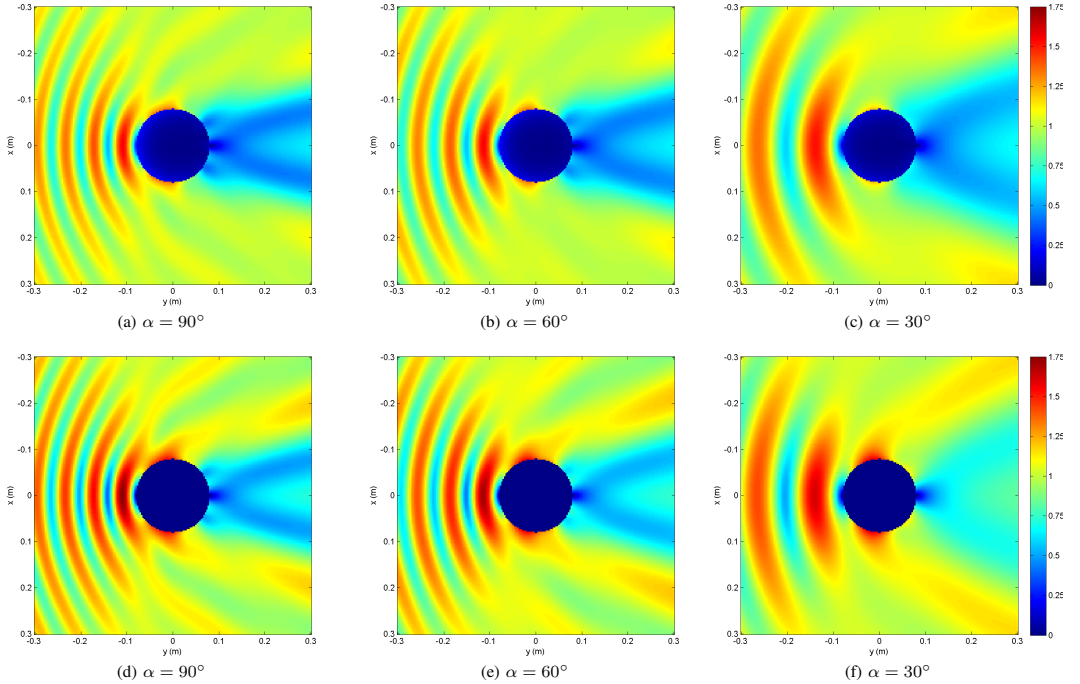


Fig. 3. Electric field strength (V/m) plot for TE plane wave incident on a human-body average (a, b, c) and PEC (d, e, f) cylinder at different angles.

The fields for a transverse electric (TE) plane wave is obtain by interchanging E and H and replacing μ by $-\frac{k^2}{\omega^2\mu}$ and multiplying the fields with $\frac{k}{\mu\omega}$. Note that there is a sign error on c_n in [9].

For the numerical calculation the infinite series need to be truncated at a suitable number N , where the series have converged. Experience shows that truncating at $N = k\rho + 20$ yields very accurate results. To check the validity of the numerical code the fields at the boundary between the cylinder and free space was calculated and the tangential component was found to be continuous. The incident field strength was chosen to be 1 V/m.

III. NUMERICAL RESULTS

The results are seen for the TM polarization and the TE polarization in Fig. 2 and Fig. 3, respectively.

For the TM polarization, for normal incidence, $\alpha = 90^\circ$, it is seen that the fields are almost the same for the PEC and the human-body cylinder. The only slight difference is the front reflection. Gradually, as the angle of incidence α decreases the difference becomes larger as most clearly seen for the plots of the electric field at an incidence angle of $\alpha = 30^\circ$. It is seen that the fields on the back side are higher for the human-body cylinder than for the PEC cylinder. The field strength on the back side increases for lower angles of incidence. In front of

the cylinder the reflection is seen to be much more powerful for the PEC cylinder than for the human-body cylinder.

For the TE polarization the fields are more different at normal incidence, i.e., $\alpha = 90^\circ$. The reflection is seen to be stronger in front of the PEC cylinder than for the human-body cylinder. On the back side the fields are significantly higher for the PEC cylinder. As the angle of incidence decreases the differences between the PEC and human-body cylinder increases. The fields on the back side are significantly higher for the PEC cylinder.

In general, the TM polarization seem to give quite similar results for the PEC and human-body cylinder whereas the difference is slightly larger for the TE polarization. It is noted that the situation in [6] is actually TM polarized and therefore there is a good correspondence with the results found in this reference. Furthermore, the differences in both cases become more pronounce when the angle of incidence decreases.

IV. CONCLUSION

The accuracy of the use of PEC as an approximation of the human body has been investigated. It was found that for normal incidence and TM polarization the human body is very well modeled by PEC. At normal incidence and TE polarization the human body is quite well modeled by PEC. As the angle of incidence become more oblique, the

differences between PEC and actual human-body parameters become more profound. For very oblique angles of incidence and TE polarization the validity of approximating the human-body by PEC is questionable.

REFERENCES

- [1] Y. Hao, A. Alomainy, Y. Zhao, C. G. Parini, Y. I. Nechayev, P. S. Hall, and C. C. Constantinou, "Statistical and Deterministic Modelling of Radio Propagation Channels in WBAN at 2.45GHz," in *Antennas and Propagation Society International Symposium 2006, IEEE*, 2006, pp. 2169–2172.
- [2] Y. Zhao, Y. Hao, A. Alomainy, and C. G. Parini, "UWB On-Body Radio Channel Modeling Using Ray Theory and Subband FDTD Method," *IEEE Trans. Microwave Theory Tech.*, vol. 54, no. 4, pp. 1827–1835, apr 2006.
- [3] R. Chandra and A. J. Johansson, "An Analytical Link-Loss Model for On-Body Propagation Around the Body Based on Elliptical Approximation of the Torso With Arms' Influence Included," *IEEE Antennas Wirel. Propag. Lett.*, vol. 12, pp. 528–531, apr 2013.
- [4] —, "A Link Loss Model for the On-body Propagation Channel for Binaural Hearing Aids," *IEEE Trans. Antennas Propagat.*, vol. 61, no. 12, pp. 6180–6190, dec 2013.
- [5] S. H. Kvist, J. Thaysen, and K. B. Jakobsen, "Ear-to-Ear On-Body Channel Model for Hearing Aid Applications," *IEEE Transactions on Antennas and Propagation*, vol. 63, no. 1, pp. 344–352, jan 2015.
- [6] M. Ghaddar, L. Talbi, and T. A. Denidni, "Human Body Modelling for Prediction of Effect of People on Indoor Propagation Channel," *Electronics Letters*, vol. 40, no. 25, pp. 1592–1594, dec 2004.
- [7] S. Gabriel, R. W. Lau, and C. Gabriel, "The Dielectric Properties of Biological Tissues: III. Parametric Models for the Dielectric Spectrum of Tissues," *Physics in Medicine and Biology*, nov 1996.
- [8] I. S. C. C. . IEEE, "IEEE Recommended Practice for Determining the Peak Spatial-Average Specific Absorption Rate (SAR) in the Human Head From Wireless Communications Devices: Measurement Techniques," dec 2003.
- [9] B. R. Levy and J. B. Keller, "Diffraction by a Smooth Object," *Communications on Pure and Applied Mathematics*, vol. 12, no. 1, pp. 159–209, 1959.
- [10] J. R. Wait, "Scattering of a Plane Wave From a Circular Dielectric Cylinder at Oblique Incidence," *Canadian Journal of Physics*, vol. 33, no. 5, pp. 189–195, 1955.

PAPER 7

“ELECTROMAGNETIC FIELDS AT THE SURFACE OF HUMAN-BODY CYLINDERS”

N. P. B. Kammergaard, S. H. Kvist, J. Thaysen, and K. B. Jakobsen

Published: 2016

[P7] N. P. B. Kammergaard, S. H. Kvist, J. Thaysen, and K. B. Jakobsen, “Electromagnetic fields at the surface of human-body cylinders”, in *Proceedings of the 2016 International Workshop on Antenna Technology*, IEEE, 2016, pp. 170–173.

Electromagnetic Fields at the Surface of Human-Body Cylinders

Nikolaj P. B. Kammersgaard*, Søren H. Kvist†, Jesper Thaysen† and Kaj B. Jakobsen*

npivka@elektro.dtu.dk, skvist@gnresound.com, jthaysen@gnresound.com, kbj@elektro.dtu.dk

*Department of Electrical Engineering, Electromagnetic Systems, Technical University of Denmark, Ørstedes Plads, Building 348, DK-2800 Kgs. Lyngby, Denmark

†GN ReSound A/S, Lautrupbjerg 7, DK-2750 Ballerup, Denmark

Abstract—The electromagnetic fields around an infinitely long cylinder with different material parameters are analyzed. The cylinder is modeled as muscle, skin, fat, and perfect electric conductor respectively. The cylinder is illuminated by a plane wave incident from different angles and with both transverse electric and transverse magnetic polarization. The results show that the material assumption when modeling the human body as a homogeneous material is very important. Furthermore, it is shown that one assumption might lead to higher fields for a specific polarization, angle of incidence and frequency, but that does not translate to similar relative performance at another polarization, angle of incidence, and frequency.

I. INTRODUCTION

Wireless body area networks (WBAN) has been an area of research interest for many years. The technology has unlimited applications within everything from sports equipment and personal communication to medical assistance and monitoring. In recent years the commercial products using WBAN have exploded with for example smart phones, smart watches and smart glasses.

With the purpose of understanding and modeling the propagation of electromagnetic fields in the proximity of the human body numerous models have been presented. Many of these model the human body as a perfect electric conductor (PEC) [1]–[4]. Other models only consider propagation in a torsional-less case [5]–[7]. Some of the same models also only investigate one of the polarizations.

The purpose of this work is to obtain a more general understanding of propagation of the electromagnetic fields close to the human body. It is desired to investigate the effect of different material parameters, angles of incidence, polarizations and frequencies.

The investigation will be done by the use of the exact formulas for the electromagnetic fields in the case of an infinitely long cylinder illuminated by a plane wave at oblique incidence. The electric fields will be calculated just above the cylinder for different material parameter, angles of incidence, polarizations and frequencies.

II. THEORY

The material parameters used are from [8]. The cylinder is modeled as muscle, skin, fat and PEC with the parameters

TABLE I
CONSTITUTIVE PARAMETERS OF DIFFERENT TISSUES

Tissue	2.45 GHz		5.8 GHz	
	σ (S/m)	ϵ_r	σ (S/m)	ϵ_r
Muscle	1.74	52.7	4.96	48.5
Skin	1.46	38.0	3.72	35.1
Fat	0.105	5.28	0.293	4.95

seen in Table I.

The infinitely long lossy dielectric cylinder is located in free space. A plane wave is incident and propagating in the direction given by $\hat{d} = (0, \sin \alpha, \cos \alpha)$ as seen in Fig. 1. The propagation constant in the cylinder and in free space are k_1 and k , respectively. Two other propagation constants are defined as $k' = k \sin \alpha$ and $k'_1 = \sqrt{k_1^2 - k^2 \cos^2 \alpha}$. The electric and magnetic fields outside the cylinder incident by a transverse magnetic (TM) plane wave are given by the following formulas obtained from [9], [10]:

$$E_\rho = -jk \cos \alpha \frac{\partial u}{\partial \rho} - \frac{j\mu\omega}{\rho} \frac{\partial v}{\partial \phi} \quad (1)$$

$$E_\phi = -\frac{jk \cos \alpha}{\rho} \frac{\partial u}{\partial \phi} + j\mu\omega \frac{\partial v}{\partial \rho} \quad (2)$$

$$E_z = k'^2 u \quad (3)$$

$$H_\rho = \frac{jk^2}{\mu\omega\rho} \frac{\partial u}{\partial \phi} - jk \cos \alpha \frac{\partial v}{\partial \rho} \quad (4)$$

$$H_\phi = -\frac{jk^2}{\mu\omega} \frac{\partial u}{\partial \rho} - \frac{jk \cos \alpha}{\rho} \frac{\partial v}{\partial \phi} \quad (5)$$

$$H_z = k'^2 v \quad (6)$$

where a common factor of $e^{-jkz \cos \alpha}$ has been suppressed as well as a time dependency of $e^{j\omega t}$. To obtain E_ρ and E_ϕ inside the cylinder the permeability μ must be replaced by μ_1 . To obtain E_z and H_z inside the cylinder the propagation constant k' must be replaced by k'_1 . To obtain H_ρ and H_ϕ inside the cylinder μ and k must be replaced by μ_1 and k_1 in the terms involving u and remain the same for the terms

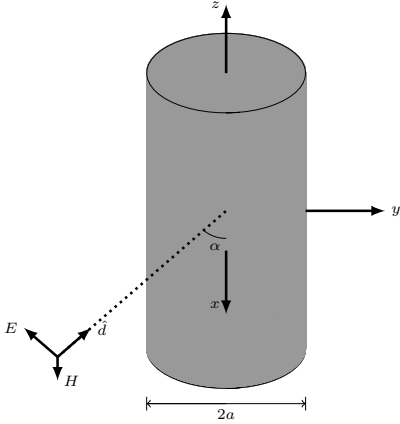


Fig. 1. The geometry of the infinitely long dielectric cylinder model.

involving v . For $\rho > a$ the scalar potentials u and v are given by [9]:

$$u = \frac{-E_0 \sin \alpha}{k'^2} \sum_{n=-\infty}^{\infty} \left(J_n(k'\rho) - a_n H_n^{(2)}(k'\rho) \right) e^{-jn\phi} \quad (7)$$

$$v = \frac{-E_0 \sin \alpha}{k'^2} \sum_{n=-\infty}^{\infty} c_n H_n^{(2)}(k'\rho) e^{-jn\phi} \quad (8)$$

and for $\rho < a$ by:

$$u = \frac{-E_0 \sin \alpha}{k'^2} \sum_{n=-\infty}^{\infty} b_n J_n(k'_1 \rho) e^{-jn\phi} \quad (9)$$

$$v = \frac{-E_0 \sin \alpha}{k'^2} \sum_{n=-\infty}^{\infty} d_n J_n(k'_1 \rho) e^{-jn\phi} \quad (10)$$

where a_n, b_n, c_n , and d_n are constants chosen to ensure the continuity of the tangential components of the E-fields and H-fields across the boundary. The constants are given by:

$$a_n = \frac{J_n(k'a)}{\Delta H_n^{(2)}} \left\{ \left[\frac{\mu_1 J'_n(k'_1 a)}{\mu k'_1 a J_n(k'_1 a)} - \frac{1}{k' a} \frac{H_n^{(2)'}(k' a)}{H_n^{(2)}(k' a)} \right] \cdot \left[\frac{k_1^2}{k^2} \frac{\mu J'_n(k'_1 a)}{\mu_1 k'_1 a J_n(k'_1 a)} - \frac{1}{k' a} \frac{J'_n(k' a)}{J_n(k' a)} \right] - \left[\frac{1}{(k' a)^2} - \frac{1}{(k'_1 a)^2} \right]^2 n^2 \cos^2 \alpha \right\} \quad (11)$$

$$b_n = \frac{k'^2}{k'_1} \left[J_n(k' a) - a_n \frac{H_n^{(2)}(k' a)}{J_n(k'_1 a)} \right]$$

$$c_n = -\frac{2kn \cos \alpha}{\Delta \mu \omega \pi (k' a)^2} \frac{1}{H_n^{(2)}(k' a)} \left[\frac{1}{(k' a)^2} - \frac{1}{(k'_1 a)^2} \right]$$

$$d_n = \frac{k'^2}{k'_1} c_n \frac{H_n^{(2)}(k' a)}{J_n(k'_1 a)}$$

where

$$\Delta = \left[\frac{\mu_1 J'_n(k'_1 a)}{\mu k'_1 a J_n(k'_1 a)} - \frac{1}{k' a} \frac{H_n^{(2)'}(k' a)}{H_n^{(2)}(k' a)} \right] \cdot \left[\frac{k_1^2}{k^2} \frac{\mu J'_n(k'_1 a)}{\mu_1 k'_1 a J_n(k'_1 a)} - \frac{1}{k' a} \frac{H_n^{(2)'}(k' a)}{H_n^{(2)}(k' a)} \right] - \left[\frac{1}{(k' a)^2} - \frac{1}{(k'_1 a)^2} \right]^2 n^2 \cos^2 \alpha.$$

The fields for a transverse electric (TE) plane wave is obtain by interchanging E and H and replacing μ by $-\frac{k^2}{\omega^2 \mu}$ and multiplying the fields with $\frac{k}{\mu \omega}$. Note that there is a sign error on c_n in [9].

For the numerical calculation the infinite series need to be truncated at a suitable number N , where the series have converged. Experience shows that truncating at $N = k\rho + 20$ yields very accurate results. To check the validity of the numerical code the fields at the boundary between the cylinder and free space was calculated and the tangential component was found to be continuous. The incident field strength was chosen to be 1 V/m.

III. NUMERICAL RESULTS

The fields at a distance of 10 mm above a cylinder with radius $a = 160$ mm was calculated with the four different material parameter, for $\alpha = 90^\circ$ and $\alpha = 45^\circ$, for both TM and TE polarization in the two industrial, scientific and medical (ISM) bands at 2.45 GHz and 5.8 GHz, respectively. The results are seen in Fig. 2 and Fig. 3 for the TM and TE cases, respectively.

In general it is seen that the results for the skin and muscle cylinder is almost completely indistinguishable. This is expected since the constitutive parameters are very similar.

For the TM polarization it is seen that the fields are very low on the back side of the cylinder. Especially, for the normal incidence at 2.45 GHz the cylinder made of fat shows significantly higher fields on the back side of the cylinder. This is most likely caused by waves transmitted through the cylinder whereas in the other cases the contribution from the propagation path through the cylinder is negligible. At normal incidence the muscle, skin, and PEC cylinders exhibit almost the exact same behavior. So in this case a human body would most likely be well approximated by PEC. At $\alpha = 45^\circ$ the situation is although completely different. The muscle and skin cylinders has electric fields on the back side that are 10 dB and 15 dB higher than the PEC cylinder at 2.45 GHz and 5.8 GHz, respectively. The general field strength on the back side is also significantly higher for the oblique incidence.

For the TE polarization the fields on the back side of the cylinder is in general significantly higher than the TM polarization. For the normal incidence the fields around the PEC cylinder is slightly higher than for the muscle and skin cylinders which show slightly higher fields than the fat cylinder. At $\alpha = 45^\circ$ these differences are a bit more

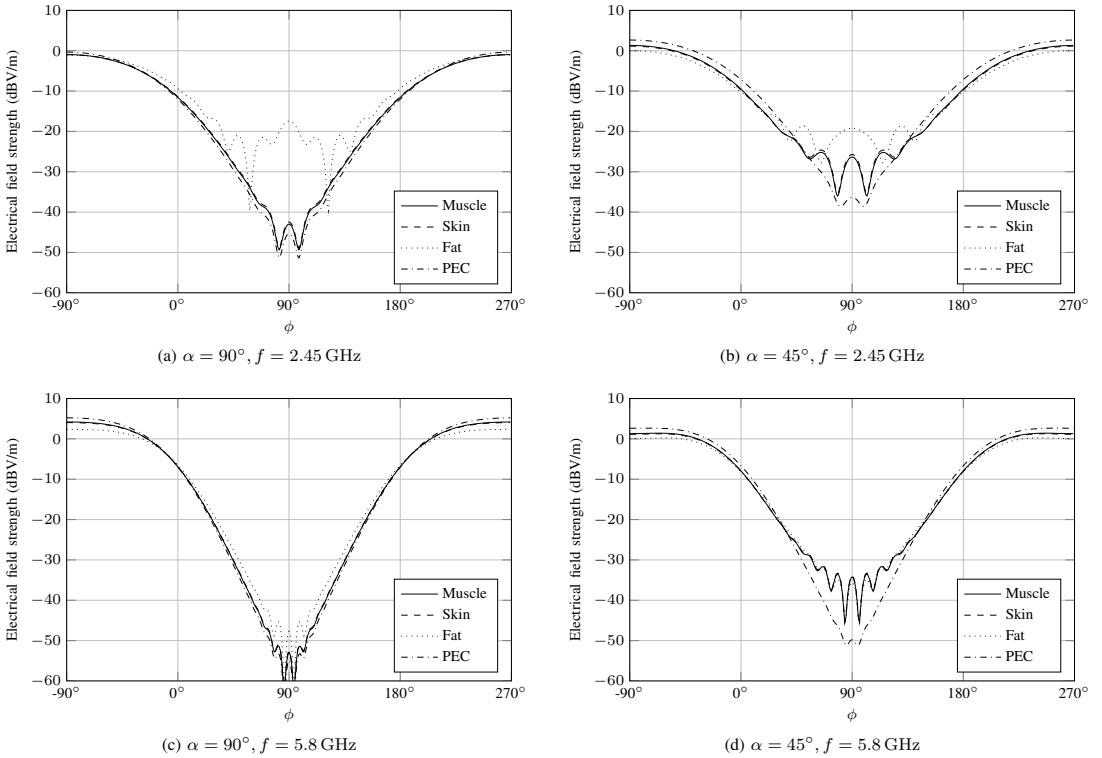


Fig. 2. Electric field plot for a TM plane wave incident on a cylinder at different angles α and frequencies f .

pronounced. The general field strength on the back side do not change significantly.

Finally, it is seen that the main impact of the change in frequency from 2.45 GHz to 5.8 GHz is primarily a bit lower fields and more closely spaced constructive and destructive interferences on the back side caused by the fact that the cylinder is electrically larger at 5.8 GHz.

The most interesting result is the fact that for TM polarization the order of the cylinders according to field strength on the back is fat, skin, muscle, and PEC with an even stronger trend at oblique incidence. Whereas the order is reversed for the TE case. This might be explained by the fact that PEC is ideal for transmission of TE polarization and ideal for attenuation of TM polarization. The human body cylinders are non-ideal PEC. Therefore, the transmission of TE polarization is worse, but so is the attenuation of TM polarization.

IV. CONCLUSION

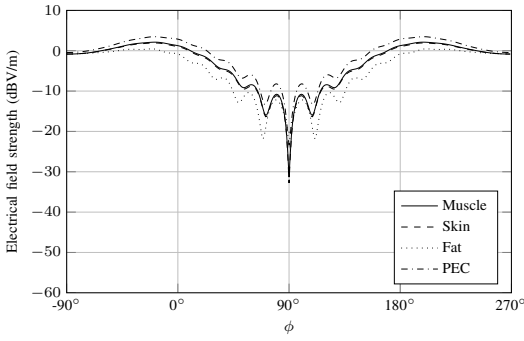
The electromagnetic fields around an infinitely long cylinder with different material parameters have been analyzed. It shows that the human-body parameters in some cases are very well approximated by PEC, but in general the results can vary

quite significantly. Furthermore, it was found that whereas PEC give higher fields than the human-body parameters on the back of the cylinder with TE polarization this was opposite for TM polarization. Oblique incidence gives higher fields than normal incidence for the TM polarization, but almost no change for the TE polarization.

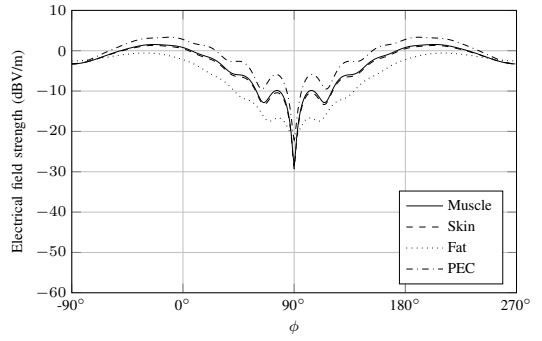
In general it is concluded that the electromagnetic fields around a human body cylinder is not always easily and intuitively predicted.

REFERENCES

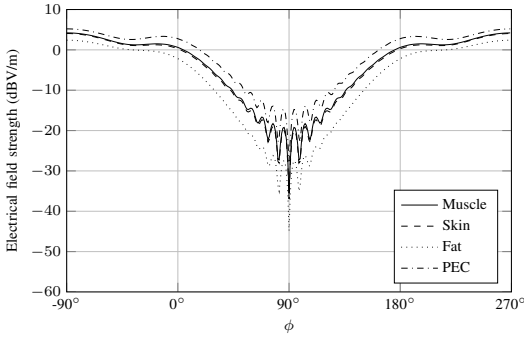
- [1] Y. Zhao, Y. Hao, A. Alomainy, and C. G. Parini, "UWB On-Body Radio Channel Modeling Using Ray Theory and Subband FDTD Method," *IEEE Trans. Microwave Theory Tech.*, vol. 54, no. 4, pp. 1827–1835, Apr 2006.
- [2] S. H. Kvist, J. Thaysen, and K. B. Jakobsen, "Ear-to-Ear On-Body Channel Model for Hearing Aid Applications," *IEEE Transactions on Antennas and Propagation*, vol. 63, no. 1, pp. 344–352, Jan 2015.
- [3] R. Chandra and A. J. Johansson, "An Analytical Link-Loss Model for On-Body Propagation Around the Body Based on Elliptical Approximation of the Torso With Arms' Influence Included," *IEEE Antennas Wirel. Propag. Lett.*, vol. 12, pp. 528–531, Apr 2013.
- [4] M. Ghaddar, L. Talbi, and T. A. Denidni, "Human Body Modelling for Prediction of Effect of People on Indoor Propagation Channel," *Electronics Letters*, vol. 40, no. 25, pp. 1592–1594, Dec 2004.



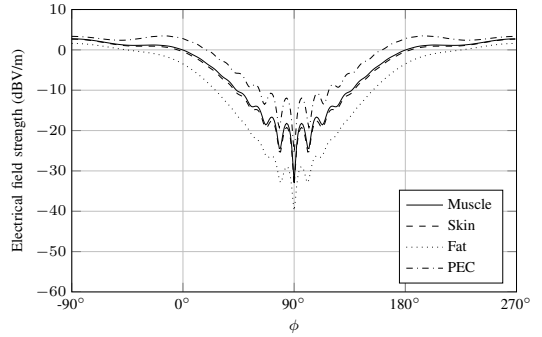
(a) $\alpha = 90^\circ, f = 2.45 \text{ GHz}$



(b) $\alpha = 45^\circ, f = 2.45 \text{ GHz}$



(c) $\alpha = 90^\circ, f = 5.8 \text{ GHz}$



(d) $\alpha = 45^\circ, f = 5.8 \text{ GHz}$

Fig. 3. Electric field plot for a TE plane wave incident on a cylinder at different angles α and frequencies f .

- [5] T. E. P. Alves, B. Poussot, and J.-M. Laheurte, "Analytical Propagation Modeling of BAN Channels Based on the Creeping-Wave Theory," *IEEE Trans. Antennas Propagat.*, vol. 59, no. 4, pp. 1269–1274, Apr 2011.
- [6] R. Chandra and A. J. Johansson, "A Link Loss Model for the On-body Propagation Channel for Binaural Hearing Aids," *IEEE Trans. Antennas Propagat.*, vol. 61, no. 12, pp. 6180–6190, Dec 2013.
- [7] C. Oliveira and L. M. Correia, "A Statistical Model to Characterize User Influence in Body Area Networks," in *Vehicular Technology Conference Fall (VTC 2010-Fall)*, 2010 IEEE 72nd, Sep 2010.
- [8] S. Gabriel, R. W. Lau, and C. Gabriel, "The Dielectric Properties of Biological Tissues: III. Parametric Models for the Dielectric Spectrum of Tissues," *Physics in Medicine and Biology*, Nov 1996.
- [9] B. R. Levy and J. B. Keller, "Diffraction by a Smooth Object," *Communications on Pure and Applied Mathematics*, vol. 12, no. 1, pp. 159–209, 1959.
- [10] J. R. Wait, "Scattering of a Plane Wave From a Circular Dielectric Cylinder at Oblique Incidence," *Canadian Journal of Physics*, vol. 33, no. 5, pp. 189–195, 1955.

PAPER 8

“BODY-WORN SPIRAL MONOPOLE ANTENNA FOR BODY-CENTRIC COMMUNICATIONS”

N. P. I. Kammersgaard, S. H. Kvist, J. Thaysen, and K. B. Jakobsen

Published: 2015

Awarded the first prize for the best student paper at IWAT 2015.

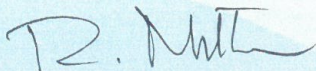
[P8] N. P. I. Kammersgaard, S. H. Kvist, J. Thaysen, and K. B. Jakobsen, “Body-worn spiral monopole antenna for body-centric communications”, in *Proceedings of the 2015 International Workshop on Antenna Technology*, IEEE, 2015, pp. 107–110.

Student Paper Award

presented to

‘Body-Worn Spiral Monopole Antenna for Body-Centric Communications’

**Nikolaj P. I. Kammersgaard, Søren H. Kvisty, Jesper Thayseny,
and Kaj B. Jakobsen Technical University of Denmark, Denmark)**



Raj Mittra

IAC Chair



Young Joong Yoon

General Chair

Body-Worn Spiral Monopole Antenna for Body-Centric Communications

Nikolaj P. I. Kammersgaard*[†], Søren H. Kvist[†], Jesper Thaysen[†] and Kaj B. Jakobsen*

npivka@elektro.dtu.dk, skvist@gnresound.com, jthaysen@gnresound.com, kbj@elektro.dtu.dk

*Department of Electrical Engineering, Electromagnetic Systems, Technical University of Denmark, Ørstedes Plads, Building 348, DK-2800 Kgs. Lyngby, Denmark

[†]GN ReSound A/S, Lautrupbjerg 7, DK-2750 Ballerup, Denmark

Abstract—A novel body-worn spiral monopole antenna is presented. The antenna consists of a ground plane and a spiral monopole. The antenna is designed for Ear-to-Ear (E2E) communication between In-the-Ear (ITE) Hearing Instruments (HIs) at 2.45 GHz and has been simulated, prototyped and measured. The antenna yields a measured and simulated Ear-to-Ear path gain at 2.45 GHz of -82.1 dB and -85.9 dB, respectively. The radiation pattern of the antenna when mounted in the ear is presented and discussed.

I. INTRODUCTION

Research in body-worn antennas for body-centric communication has increased in the last decade. Ever smaller electronics have enabled a wide range of new applications where wireless communication can be implemented. Many of these new applications have been within health equipment. One of these is for HIs. In the HI industry there is an interest in obtaining E2E communication between the HIs. An E2E link improves the acoustic performance of the HIs as well as the usability. Besides E2E communication there is an interest in communication with both on- and off-body accessories. By the use of the license free and worldwide Industrial, Scientific and Medical (ISM) band between 2.40 GHz and 2.48 GHz both E2E and accessory communication can be obtained. At the same time it will enable communication with electronics with Bluetooth. Antennas suitable for Behind-the-Ear (BTE) HIs have been presented in the literature with an E2E path gain of -52 dB [1]. The ITE antennas that has been presented in the literature have not yielded E2E path gains significantly above -90 dB [2], [3]. In the following a novel ITE antenna which is the first to make E2E communication feasible between ITE HIs is presented. The antenna was first presented briefly in [4]. Here the antenna is presented in depth and new results are presented.

II. THEORY

At 2.45 GHz the human body is very lossy [5]. Therefore, the electromagnetic energy can not propagate through the body. It has been shown that the electromagnetic energy propagates around the human body as creeping waves instead [6]. Models for the E2E propagation channel have been presented in [7], [8]. These models estimate the E2E path gain by the



Fig. 1. The fabricated prototype of the spiral monopole antenna. The connected coaxial cable and balun are seen at the top.

use of a number of elliptic paths around the head. For each of these paths an estimate of the magnitude of the creeping wave launched in each path is made. The attenuation along each path is calculated by a closed form expression. Finally, the contributions of each of the paths are added to give the path gain. In [8] the on-body gain is used to estimate the magnitude of the launched creeping waves. The on-body gain will be used to evaluate the radiation pattern of the antenna presented here. The phase of the electric field has been included in the on-body gain to account for the initial phase differences in the launched creeping waves. This means that the on-body gain is an untraditional gain that has both a magnitude and a phase, which can be expressed as:

$$G_{\text{on-body}}(\phi) = \int_0^\pi G_\theta(\theta, \phi) e^{j\angle E_\theta(\theta, \phi)} \sin\theta d\theta, \quad (1)$$

where $G_\theta(\theta, \phi)$ is the θ -component of the gain for the antenna mounted on the head, and $E_\theta(\theta, \phi)$ is the θ -component of the electric field for the antenna when it is mounted on the head. It is noted that it is only the θ -component that is included in the equation. This is due to the fact that the ϕ -component is attenuated much faster than the θ -component [9].

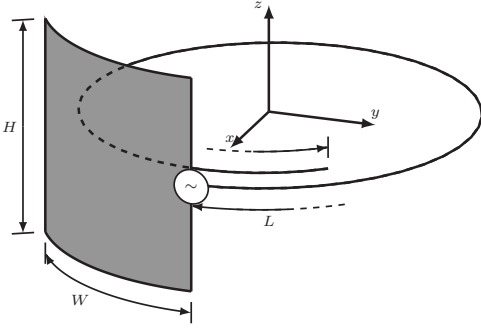


Fig. 2. The spiral monopole antenna.

 TABLE I
 OPTIMIZED ANTENNA DESIGN PARAMETERS

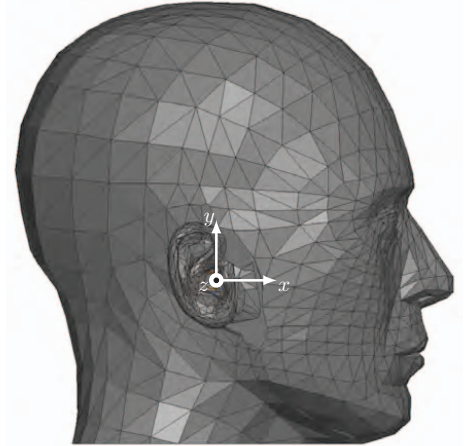
Parameter	Value (mm)
L	31
r	0.10
W	6.0
H	5.0
R	5.0
d	1.0

III. EXPERIMENTAL SETUP

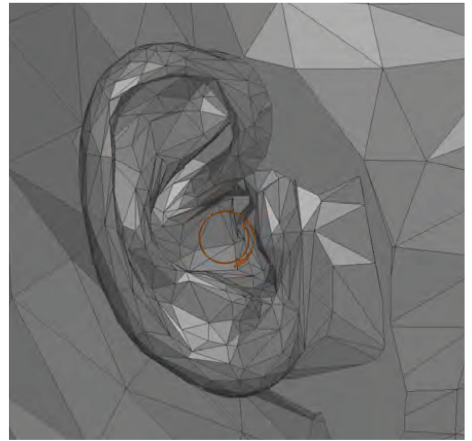
The antenna consists of a ground plane connected to a monopole with radius r . The antenna can be seen in Fig. 2. An advantage of this design is that the electronics for the HI could be placed on the ground plane. To reduce the size the monopole is spiraled with a spiral radius R that is reduced by d for each turn. The parameters used can be seen in Table I. The antenna is self resonant since the length of the monopole corresponds to approximately a quarter wavelength at 2.45 GHz. The antenna was matched for 50Ω . The antenna was placed in the ear so the plane of the spiral monopole (XY-plane in Fig. 2) coincides with the surface of the head. This means that seen from the front of the head, the antenna is completely hidden by the tragus, i.e., the cartilaginous fleshy projection that partially covers the entrance to the external ear.

Simulations were done in ANSYS HFSS 2014. The Specific Anthropomorphic Mannequin (SAM) fitted with realistic ear was used. The head and ears were given homogeneous electrical parameters of $\epsilon_r = 50$ and $\tan\delta = 0.5$. The antenna was modeled as copper. The simulation setup can be seen in Fig. 3. It is noted that the coordinate systems indicated in Fig. 3a and Fig. 2 are the same.

The prototype used for the measurements can be seen in Fig. 1. ROHACEL[®] HF ($\epsilon_r = 1.05$ and $\tan\delta < 0.0002$) was used to support the antenna. The antenna was fed from a coaxial cable connected to a Vector Network Analyzer. The cable was fitted with a balun to reduce the currents on the cable. The measurements were done in a radio anechoic chamber.



(a)



(b)

Fig. 3. The SAM phantom head (a) with the coordinate system used and the realistic ear (b) where the antenna can be seen (orange)

IV. RESULTS AND DISCUSSION

The simulated and measure E2E path gain can be seen in Fig. 4. In the entire ISM band the simulated and measured path gain is better than -86.7 dB and -83.5 dB, respectively. It is noted that this is within the dynamic range of many standard Bluetooth ICs. Since the antenna is completely ϕ -polarized in free space it might be possible to obtain a better path gain with a θ -polarized antenna as shown for BTE antennas [10]. The simulated and measured reflection coefficient plotted in a Smith chart can be seen in Fig. 5. As seen the antenna is matched for the entire ISM band. The measurement and simulation results correspond well. It is seen that the measurements are more broadband than the simulations. One of the possible causes are higher loss in the

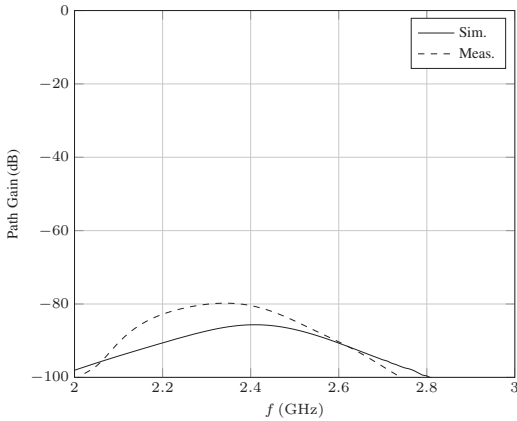


Fig. 4. Simulated (solid line) and measured (dashed line) E2E path gain.

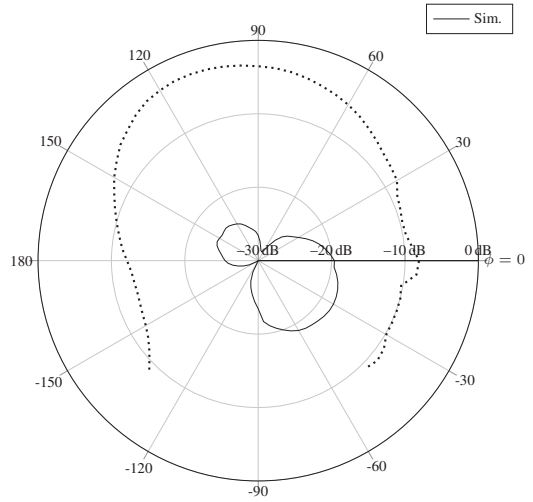


Fig. 6. Magnitude of the simulated on-body radiation pattern at 2.45 GHz (solid line) on top of the head contour (dashed line).

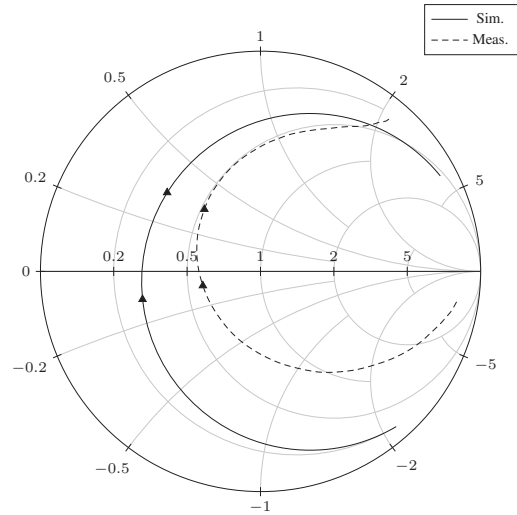


Fig. 5. Smith chart that shows the simulated (solid line) and measured (dashed line) reflection coefficient. The lower and upper frequency in the ISM band are marked by triangles.

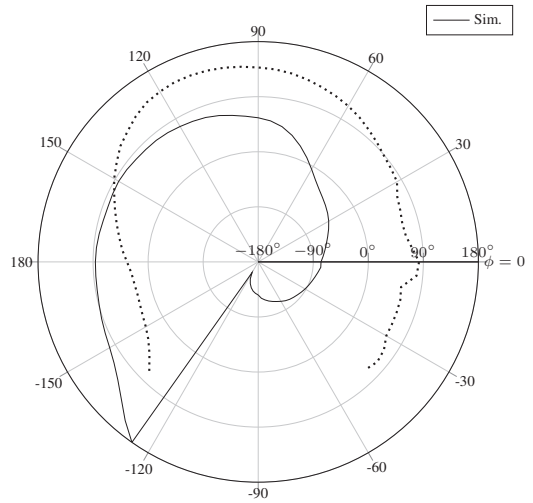


Fig. 7. Phase of the simulated on-body radiation pattern at 2.45 GHz (solid line) on top of the head contour (dashed line).

measurements resulting in the higher real part of the input impedance which appears in Fig. 5. Furthermore, the effect of the cables can have had an impact. Especially outside the ISM band that the balun is designed for. The lower and more broadband reflection coefficient also account for the higher path gain in the measurements. Finally, it is noted that the head and ears used for the measurements is not the same as for the simulations.

The magnitude and phase of the simulated on-body gain calculated from Eq. 1 can be seen in Fig. 6 and Fig. 7, respectively. From Fig. 6 it is seen that the radiation pattern

has two lobes that are in opposite directions. The radiation patterns for other ITE antennas found in [7], [11] exhibit the same characteristic, which might indicate that this is a general trend for ITE antennas caused by the ear. Furthermore, it is seen that the lobe in the forward direction has the highest gain. The BTE antennas presented in the literature have had their main lobe in the backward direction, see for example [8]. Therefore, contrary to BTE antennas it is important to understand how the creeping wave propagates across the face.

The previously mentioned E2E on-body path gain models [7], [8], which model the head with elliptic curves have been tested with antennas where the main path is behind the head. Since the face is not as well modeled with elliptic curves as the back of the head it is suggested that these models are tested with the main path around the front of the head. The phase of the on-body gain seen in Fig. 7 is seen to have a spiral characteristic corresponding to the shape of the antenna. This is different from the phase pattern in [11] which indicates that the phase is not only determined by the presence of the ear. Furthermore, it is noted that the two lobes are out-of-phase.

V. CONCLUSION

A novel ITE antenna has been designed, simulated, prototyped, and measured. It is the first ITE antenna, which is feasible to implement and yields a high enough path gain to be used with standard Bluetooth ICs. The measured and simulated E2E path gain at 2.45 GHz was -82.1 dB and -85.9 dB, respectively. The antenna was well matched in the entire ISM band. The on-body radiation pattern was presented and discussed. The radiation pattern showed two lobes. The main lobe was towards the front of the head opposite to what has been observed for BTE antennas. Therefore, it is suggested that it is investigated whether the existing models of the E2E path gain can be improved. Furthermore, it was found that it is possible to modify the phase of the on-body gain for ITE antennas through the antenna design.

REFERENCES

- [1] S. H. Kvist, S. Özden, J. Thaysen, and K. B. Jakobsen, "Improvement of the ear-to-ear path gain at 2.45 GHz using parasitic antenna element," in *Proceedings of 6th European Conference on Antennas and Propagation, EuCAP 2012*, Prague, Czech Republic, 2012, pp. 944 – 947.
- [2] R. Chandra and A. J. Johansson, "Miniaturized antennas for link between binaural hearing aids," in *2010 Annual International Conference of the IEEE Engineering in Medicine and Biology Society, EMBC'10*, Buenos Aires, Argentina, 2010, pp. 688–691.
- [3] L. Huitema, S. Sufyar, C. Delaveaud, and R. D'Errico, "Miniature antenna effect on the ear-to-ear radio channel characteristics," in *Proceedings of 6th European Conference on Antennas and Propagation, EuCAP 2012*, Prague, Czech Republic, 2012, pp. 3402–3406.
- [4] N. P. I. Kammergaard, S. H. Kvist, J. Thaysen, and K. B. Jakobsen, "In-the-ear spiral monopole antenna for hearing instruments," *Electronics Letters*, vol. 50, no. 21, pp. 1509–1511, 2014.
- [5] S. Gabriel, R. W. Lau, and C. Gabriel, "The dielectric properties of biological tissues: III. Parametric models for the dielectric spectrum of tissues," *Physics in medicine and biology*, vol. 41, pp. 2271–2293, 1996.
- [6] J. Ryckaert, P. De Doncker, R. Meys, A. de Le Hoye, and S. Donnay, "Channel model for wireless communication around human body," *Electronics Letters*, vol. 40, no. 9, pp. 543–544, 2004.
- [7] R. Chandra and A. J. Johansson, "A link loss model for the on-body propagation channel for binaural hearing aids," *IEEE Transactions on Antennas and Propagation*, vol. 61, pp. 6180–6190, 2013.
- [8] S. H. Kvist, J. Thaysen, and K. B. Jakobsen, "Ear-to-Ear On-Body Channel Model for Hearing Aid Applications," *Accepted to IEEE Trans. Antennas Propagat.*, 2014.
- [9] P. S. Hall, Y. Hao, Y. I. Nechayev, A. Alomalny, C. C. Constantinou, C. Parini, M. R. Kamarudin, T. Z. Salim, D. T. M. Hee, R. Dubrovka, A. S. Owadally, W. Song, A. Serra, P. Nepa, M. Gallo, and M. Bozzetti, "Antennas and propagation for on-body communication systems," *IEEE Antennas and Propagation Magazine*, vol. 49, pp. 41–58, 2007.
- [10] S. H. Kvist, J. Thaysen, and K. B. Jakobsen, "Polarization of unbalanced antennas for ear-to-ear on-body communications at 2.45 GHz," in *LAPC 2011 - 2011 Loughborough Antennas and Propagation Conference*, Loughborough, UK, 2011.
- [11] N. P. I. Kammergaard, S. H. Kvist, J. Thaysen, and K. B. Jakobsen, "Pinna Model for Hearing Instrument Applications," *Accepted for 2014 Loughborough Antennas & Propagation Conference*, 2014.

PAPER 9

“IMPACT OF PLACEMENT OF IN-THE-EAR ANTENNA ON EAR-TO-EAR PATH GAIN”

N. P. B. Kammersgaard, S. H. Kvist, J. Thaysen, and K. B. Jakobsen

Published: 2015

[P9] N. P. B. Kammersgaard, S. H. Kvist, J. Thaysen, and K. B. Jakobsen, “Impact of placement of in-the-ear antenna on ear-to-ear path gain”, in *Proceedings of 2015 Loughborough Antennas & Propagation Conference*, IEEE, 2015.

Impact of Placement of In-the-Ear Antenna on Ear-to-Ear Path Gain

Nikolaj P. B. Kammersgaard^{*†}, Søren H. Kvist[†], Jesper Thaysen[†] and Kaj B. Jakobsen^{*}

npivka@elektro.dtu.dk, skvist@gnresound.com, jthaysen@gnresound.com, kbj@elektro.dtu.dk

^{*}Department of Electrical Engineering, Electromagnetic Systems, Technical University of Denmark, Ørstedes Plads, Building 348, DK-2800 Kgs. Lyngby, Denmark

[†]GN ReSound A/S, Lautrupbjerg 7, DK-2750 Ballerup, Denmark

Abstract—An in-the-ear antenna is rotated in the concha. For the different placements the ear-to-ear path gain is simulated and measured. The simulations and measurements show that the ear-to-ear path gain varies with more than 15 dB even though it is the same antenna that occupies the same volume, which has only been rotated. This illustrates the importance of the correct placement of the antenna. The variation of the ear-to-ear path gain is compared with the far-field efficiency in order to explain part of the variation. The best and worst placements' radiation patterns are analyzed.

I. INTRODUCTION

Body-centric wireless communication has been researched extensively in the past years. Wireless Body Area Networks (WBAN) are now used in many different applications for communicating between devices in the proximity of the human body. There are off-body communication between a smart phone and the base station, on-body communication between a smart watch and a smart phone and in-body communication between an implant and a receiver on the surface of the body. Within the Hearing Instrument (HI) industry the technology is also used. To enable off-body communication with all kinds of accessories the Industrial, Scientific and Medical (ISM) band at 2.45 GHz is of special interest. At the same time there is a desire for ear-to-ear (E2E) communication to improve usability and acoustic performance. Since E2E communication is harder to achieve, it is the main focus.

The different kinds of HIs can be categorized into Behind-the-Ear (BTE) and In-the-Ear (ITE) devices. For the BTE, the devices are located behind the ear and the antenna can be located relatively far away from the human tissue. On the other hand the ITE devices are located in the concha, i.e., the hollow space right outside the ear canal. Therefore, the antenna is in a kind of quasi in-body environment. Even small movements of the antenna can change the antenna performance drastically as seen in [1]. Therefore, the placement of the antenna is of paramount importance.

The purpose of the work is to investigate the impact of rotation of an ITE antenna on the antenna performance. Furthermore, to explain the effects that cause the changes.

The investigation will consist of measurements and simulations on an ITE antenna that is rotated inside the concha. The measured and simulated path gains will be compared.

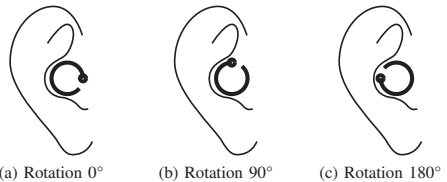


Fig. 1. The antenna in the concha is rotated counter clockwise in steps of 10° and 30° in the simulation and measurement, respectively.

The impact from the efficiency and the radiation pattern will be investigated.

II. THEORY

The body is very lossy at 2.45 GHz as shown in [2]. Therefore, the electromagnetic energy can not propagate through the head, but instead it propagates around the head as creeping waves [3]. In [4], [5] the head was modeled as a number of elliptic cylinders to estimate the path gain between the HIs. In [5] the so-called on-body gain is used to approximate the strength of the creeping waves launched. Here following the same definition, but including a phase component the on-body directivity is used to compare the different positions. This means that the on-body directivity is an untraditional directivity that has both a magnitude and a phase, which can be expressed as shown in Eq. 1.

$$D_{\text{on-body}}(\phi) = \int_0^\pi D_\theta(\theta, \phi) e^{j\angle E_\theta(\theta, \phi)} \sin\theta d\theta, \quad (1)$$

where $D_\theta(\theta, \phi)$ is the θ -component of the directivity for the antenna mounted on the head, and $E_\theta(\theta, \phi)$ is the θ -component of the electric field for the antenna when it is mounted on the head. It is noted that it is only the θ -component that is included in the equation. This is due to the fact that the ϕ -component is attenuated much faster than the θ -component [6].

To compare the performance of the antenna in different positions without the impact of the impedance matching the maximum achievable path gain $|S_{21}^{\text{max}}|$ is used. This is the path gain $|S_{21}|$ obtained when both antennas are perfectly matched. It can be calculated using [7]. In this case when the path gain

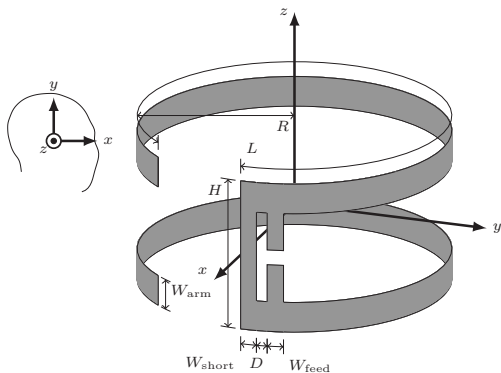


Fig. 2. The circular-shaped balanced inverted-A antenna.

TABLE I
ANTENNA DESIGN PARAMETERS

Parameter	Value (mm)
L	29
H	5.0
W_{arm}	1.0
W_{short}	0.60
W_{feed}	0.60
D	0.30
R	5.0

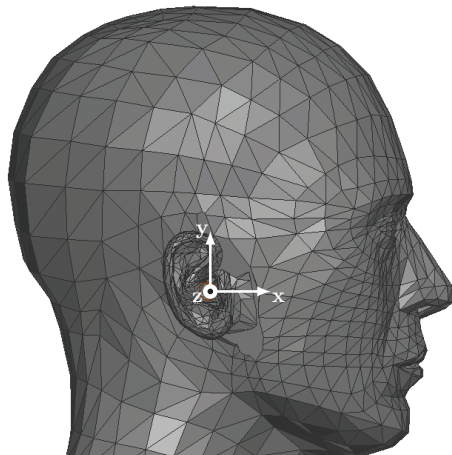
$|S_{21}|$ is very low the maximum achievable path gain $|S_{21}^{\text{max}}|$ can be approximated by Eq. 2, i.e.,

$$|S_{21}^{\text{max}}| \approx \frac{|S_{21}|^2}{(1 - |S_{11}|^2)(1 - |S_{22}|^2)}. \quad (2)$$

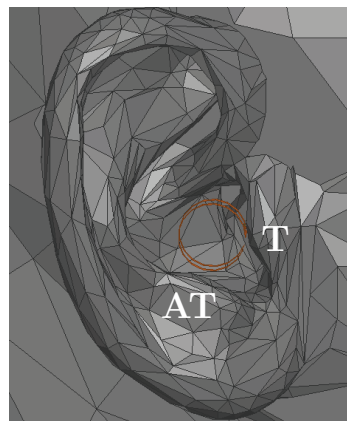
III. EXPERIMENTAL SETUP

The antenna used for the investigation is an ITE circular-shaped balanced inverted-A antenna. The antenna and the antenna design parameters are shown in Fig. 2 and Table I, respectively. The antenna is presented in depth in [8]. The antenna was placed in the concha such that the XY-plane of the coordinate system in Fig. 2 coincides with the surface of the head. The antenna in the right ear was rotated counter clockwise in steps of 10° and 30° in the simulation and measurement, respectively. This is illustrated in Fig. 1. For the left ear the rotation and the antenna is mirrored and therefore it is in a clockwise direction where 0° is where the short circuit of the antenna points towards the front of the head. The simulations and measurements were made at 2.45 GHz.

The simulations were done in ANSYS HFSS 2014. The Specific Anthropomorphic Mannequin (SAM) fitted with realistic ear was used. The head and ears have homogeneous electrical parameters of $\epsilon_r = 50$ and $\tan\delta = 0.5$. The antennas were modeled as copper. The simulation setup can be seen in



(a)



(b)

Fig. 3. The SAM phantom head (a) with the coordinate system used and a close up of the realistic ear (b) where the antenna can be seen (orange). The tragus and anti-tragus are marked T and AT, respectively.

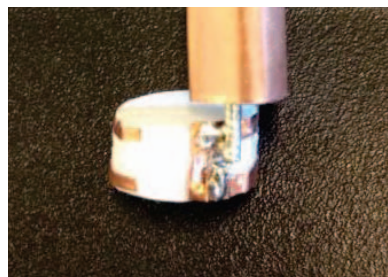


Fig. 4. The fabricated prototype of the circular-shaped balanced inverted-A antenna. The connected coaxial cable and balun are seen at the top.

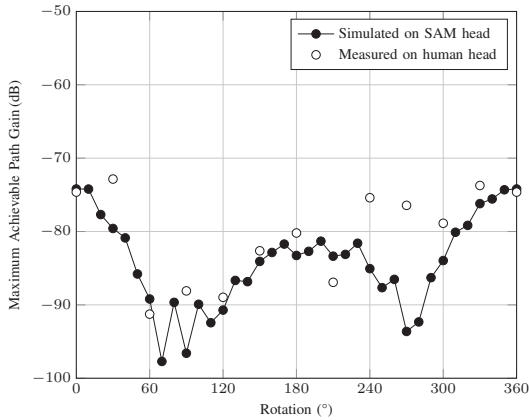


Fig. 5. Simulated (solid line) and measured (circles) E2E path gain.

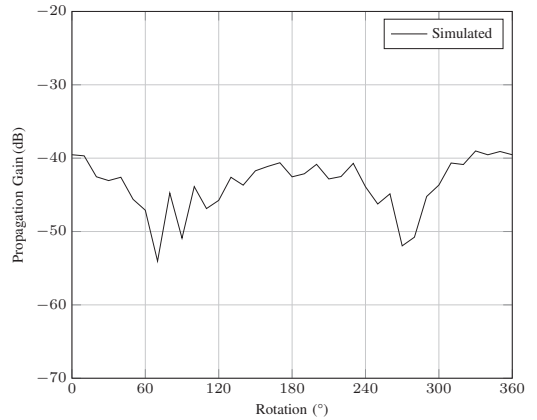


Fig. 7. Simulated propagation gain.

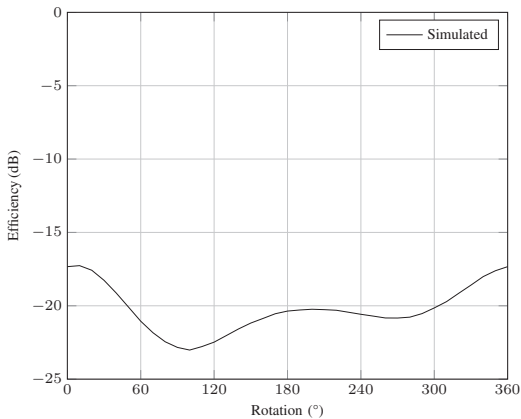


Fig. 6. Simulated efficiency.

Fig. 3. The coordinate systems in Fig. 2 and Fig. 3 coincide. As mentioned the antennas were turned 10° and simulated for each position. The convergence criteria for S_{21}^{\max} was set to 10^{-5} , which corresponds to 1 dB at -80 dB.

One of the prototypes used for the measurements can be seen in Fig. 4. The other is a mirrored version of this one. ROHACELL[®] HF ($\epsilon_r = 1.05$ and $\tan\delta < 0.0002$) was used to support the antennas. The antennas were fed from coaxial cables. The cables were fitted with baluns to reduce the currents on the cables. The coaxial cables were connected to a Vector Network Analyzer (VNA) to measure the path gain. The antennas were turned in step of 30° and the path gain was measured at each point. The measurements were done in a radio anechoic chamber.

IV. RESULTS AND DISCUSSION

The simulated and measured maximum achievable path gains are seen in Fig. 5. It is seen that simulation and measurements show a variation of more than 15 dB for the different positions. For most of the positions the simulation and measurement are in good correspondence, especially considering that the antenna is mounted on two different heads. Furthermore, the parasitic currents on the cable may have impacted the measurements. The simulation convergence criteria is also not strict enough at the very low path gains, but was chosen because of memory considerations. The characteristics of the curve is believe to be caused primarily by the near-field losses. The electric field is largest at the end of the two antenna arms. At the two minima on the simulated curve the ends of the antenna arms are placed in front of the tragus (at 60° – 120°) and anti-tragus (250° – 290°), which could explain the higher losses. The major differences between the simulation and measurement is when the antenna arms are in front of the anti-tragus. When the ears of the SAM head and the test person's head were compared it was seen that the test person is almost completely without an anti-tragus, which could further explain the difference.

The simulated efficiency is seen in Fig. 6. It is noted that it exhibits an similar characteristic as the path gain. This also corresponds to the explanation that the main cause of the changes are the near-field losses. The maximum achievable path gain was divided by the efficiency twice to give the propagation gain. This is shown in Fig. 7. As seen the variation is much smaller than for the path gain. Still, there is a 10 dB variation. To understand this the simulated on-body directivity is calculated for 0° and 270° . The magnitude is shown in Fig. 8 and the phase in Fig. 9. As seen the radiation pattern seems to have turned around by -50° for the 270° position. At the same time the lobe towards the front is around 3 dB lower in magnitude and smaller in beam width for the 270° position,

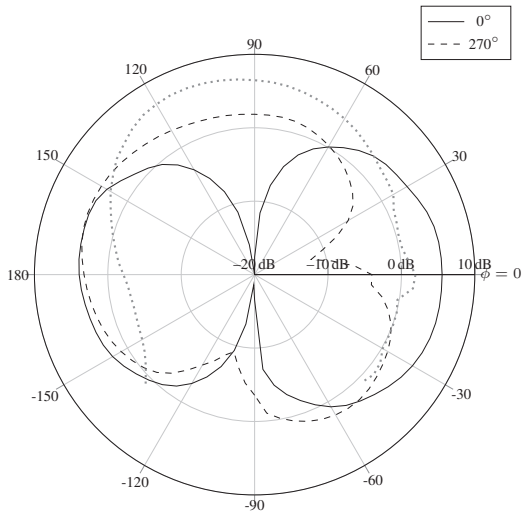


Fig. 8. Magnitude of the simulated on-body directivity at 2.45 GHz for the position 0° (solid) and 270° (dashed). The dotted line shows the contour of the head.

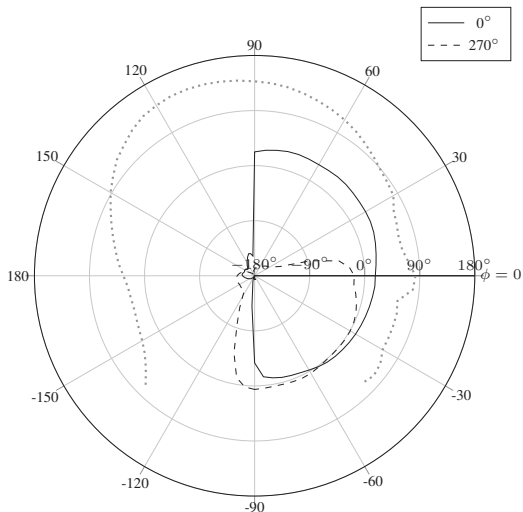


Fig. 9. Phase of the simulated on-body directivity at 2.45 GHz for the position 0° (solid) and 270° (dashed). The dotted line shows the contour of the head.

whereas the lobe towards the back is of similar magnitude, but larger beam width. This implies that the directivity towards the front might be more important than the directivity towards the back when the antenna is placed in the concha.

V. CONCLUSION

The impact of the placement of an ITE antenna on the ear-to-ear path gain has been investigated. It was found that rotation of the antenna, while it is kept in the same volume, can change the maximum achievable path gain with more than 15 dB. Furthermore, it was found that part of the variation could be explained by the efficiency of the antenna at the different placements. The efficiency change was explained by the near-field losses. The rest of the variation was investigated by the use of the on-body directivity. It was found that a high directivity towards the front of the head is desirable. The investigation clearly shows that it is important to place the antenna in an optimal way in the concha.

REFERENCES

- [1] N. P. I. Kammersgaard, S. H. Kvist, J. Thaysen, and K. B. Jakobsen, "Pinna Model for Hearing Instrument Applications," *Proceedings of 2014 Loughborough Antennas and Propagation Conference*, pp. 141 – 143, 2014.
- [2] S. Gabriel, R. W. Lau, and C. Gabriel, "The dielectric properties of biological tissues: III. Parametric models for the dielectric spectrum of tissues." *Physics in medicine and biology*, vol. 41, pp. 2271–2293, 1996.
- [3] J. Ryckaert, P. De Doncker, R. Meys, A. de Le Hoye, and S. Donnay, "Channel Model for Wireless Communication Around Human Body," *Electronics Letters*, vol. 40, no. 9, pp. 543–544, Apr. 2004.
- [4] R. Chandra and A. J. Johansson, "A link loss model for the on-body propagation channel for binaural hearing aids," *IEEE Transactions on Antennas and Propagation*, vol. 61, pp. 6180–6190, 2013.
- [5] S. H. Kvist, J. Thaysen, and K. B. Jakobsen, "Ear-to-Ear On-Body Channel Model for Hearing Aid Applications," *IEEE Transactions on Antennas and Propagation*, vol. 63, no. 1, pp. 344–352, Jan. 2015.
- [6] P. S. Hall, Y. Hao, Y. I. Nechayev, A. Alomainy, C. C. Constantinou, C. G. Parini, M. R. Kamarudin, T. Salim, D. Hee, R. F. Dubrovka, A. Owadally, W. Song, A. A. Serra, P. Nepa, M. Gallo, and M. Bozzetti, "Antennas and Propagation for On-Body Communication Systems," *IEEE Antennas Propag. Mag.*, vol. 49, no. 3, pp. 41–58, 2007.
- [7] J. Vidkjaer, "Linear Active Two-Ports," in *Class Notes, 31415 RF-Communication Circuits*, 2013, ch. 3. [Online]. Available: <http://rftoolbox.dtu.dk/book/Ch3.pdf>
- [8] N. P. I. Kammersgaard, S. H. Kvist, J. Thaysen, and K. B. Jakobsen, "In-the-Ear Circular-Shaped Balanced Inverted-A Antenna for Hearing Instruments," *Submitted to IEEE Antennas and Wireless Propagation Letters*, 2015.

PAPER 10

“VERTICALLY POLARIZED OMNIDIRECTIONAL PRINTED SLOT LOOP ANTENNA”

N. P. I. Kammersgaard, S. H. Kvist, J. Thaysen, and K. B. Jakobsen

Published: 2015

[P10] N. P. I. Kammersgaard, S. H. Kvist, J. Thaysen, and K. B. Jakobsen, “Vertically polarized omnidirectional printed slot loop antenna”, in *Proceedings of Eucap 2015*, EurAAP, 2015.

Vertically Polarized Omnidirectional Printed Slot Loop Antenna

Nikolaj P. I. Kammersgaard^{1,2}, Søren H. Kvist², Jesper Thaysen² and Kaj B. Jakobsen¹

npivka@elektro.dtu.dk, skvist@gnresound.com, jthaysen@gnresound.com, kbj@elektro.dtu.dk

¹Department of Electrical Engineering, Electromagnetic Systems, Technical University of Denmark, Ørstedes Plads, Building 348, DK-2800 Kgs. Lyngby, Denmark

²GN ReSound A/S, Lautrupbjerg 7, DK-2750 Ballerup, Denmark

Abstract—A novel vertically polarized omnidirectional printed slot loop antenna has been designed, simulated, fabricated and measured. The slot loop works as a magnetic loop. The loop is loaded with inductors to insure uniform and in-phase fields in the slot in order to obtain an omnidirectional radiation pattern. The antenna is designed for the 2.45 GHz Industrial, Scientific and Medical band. Applications of the antenna are many. One is for on-body applications since it is ideal for launching a creeping waves due to the polarization.

I. INTRODUCTION

The number of applications for Wireless Body Area Networks (WBAN) has increased rapidly in recent years. The ever smaller electronics enable these applications, which at the same time call for improved antennas. Many of the applications are designed for the worldwide and license free Industrial, Scientific, and Medical (ISM) band at 2.45 GHz. Propagation at 2.45 GHz through the human body is very lossy [1]. Instead, the electromagnetic energy creeps around the human body [2]. It has been shown that when the polarization of the electrical field is perpendicular to the surface of the human body, it is far more efficient in launching creeping waves [3]. The inspiration for the antenna originates from the antenna found in [4], which is an electric loop antenna. The antenna in [4] is horizontally polarized and thus gives a parallel polarization if placed flat on a human body. By the use of Babinet's principle with Booker's extension as found in [5] it is seen that by interchanging the areas covered with copper with those not covered by copper, the polarization can be change to vertical. The impedance of the complimentary antenna is [5]:

$$Z_{\text{magnetic}} = \frac{\eta^2}{Z_{\text{electric}}}, \quad (1)$$

where Z_{electric} is the impedance of the original antenna and η is the intrinsic impedance of the media in which the antenna is placed. Since this results in a too large impedance for the complimentary antenna and the theory is based on the use of Perfect Electric Conductors (PEC) and not copper, the antenna design in [4] has been modified. Furthermore, the ground plane of the antenna has been truncated since the theoretical antenna should have an infinite ground plane.

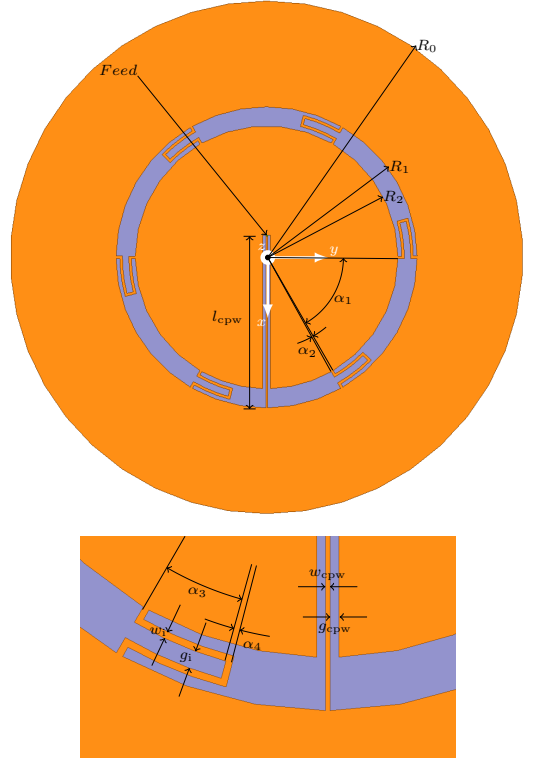


Fig. 1. Antenna layout.

II. ANTENNA DESIGN

The layout of the antenna can be seen in Fig. 1. The design parameters can be found in Table I. The copper layout is placed on a Rogers 6002 substrate ($\epsilon_r = 2.94$ and $\tan\delta = 0.0012$) with a height of $h = 0.8$ mm. The antenna is fed at the end of the coplanar waveguide (CPW) that serves as an impedance transformer. The CPW has a characteristic impedance of 118Ω and an electric length of 0.31λ at 2.45 GHz. The circular slot

TABLE I
OPTIMIZED ANTENNA DESIGN PARAMETERS

Parameter	Value
g_{cpw}	0.50 mm
g_i	1.0 mm
l_{cpw}	27 mm
N	6
R_0	40 mm
R_1	23.5 mm
R_2	20.5 mm
w_i	0.40 mm
w_{cpw}	0.25 mm
α_1	59°
α_2	1.0°
α_3	14.5°
α_4	1.0°

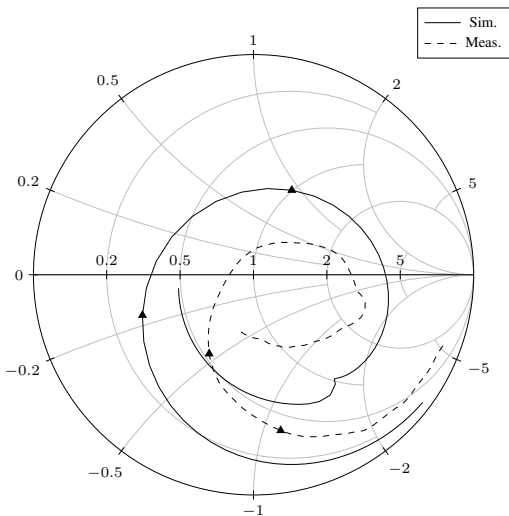


Fig. 2. Smith chart that shows the simulated reflection coefficient for a frequency between 2 GHz and 3 GHz. The lower and upper frequency in the ISM band are marked by triangles.

is loaded with $N = 6$ inductors to insure uniform magnitude and phase of the field in the slot. In the same way as an inductor in series is used to make a monopole antenna appear electrically longer — capacitors in series can be used to make an electric loop appear electrically shorter. In the dual this corresponds to inductors in parallel. Thus, the inductors make the loop, which is significantly longer than a wavelength, work like a small loop. The exact parameters used have been found through optimization using simulation results. A larger R_0 gives a more narrow null in the XY-plane, while a smaller R_0 gives a wider null. The a small difference between R_1 and R_2 gives a lower resonance frequency as well as a longer slot. A lower N gives a lower resonance frequency as well as a larger α_3 . These effects can also be seen by viewing the slot

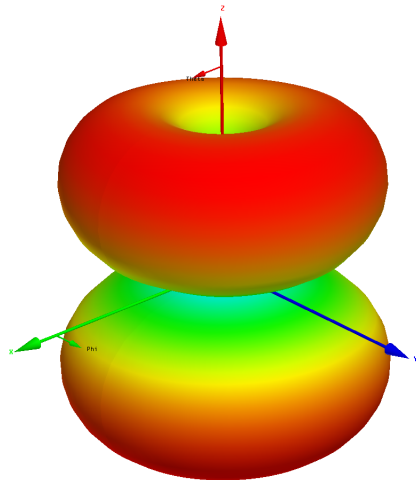


Fig. 3. Radiation pattern of the printed slot loop antenna. The logarithmic color scale range from -18 dB (blue) to 2 dB (red).

as a parallel LC-circuit.

The coordinate system used is seen in white in Fig. 1 with the layout place in the XY-plane. The layout was simulated in ANSYS HFSS 2014 where the CPW was fed through a lumped port. A prototype was fabricated and measured. The prototype measurements were done with a coaxial cable mounted at the feed point. The outer conductor was soldered to the ground and the inner conductor to the CPW line. The coaxial cable was fitted with ferrite beads to reduce the currents on the outside of the cable. For both simulations and measurements a characteristic impedance of 50Ω was used.

III. SIMULATION AND MEASUREMENT RESULTS

The simulated and measured reflection coefficient between 2 GHz and 3 GHz can be seen in the Smith chart in Fig. 2. At 2.45 GHz the magnitude of the simulated and measured reflection coefficient is -8.54 dB and -5.15 dB, respectively. The simulated and measured 6 dB bandwidth is 100 MHz and 285 MHz, respectively. As seen from Fig. 2 the simulated antenna is well matched for the 2.45 GHz ISM band as intended where as the measured antenna is shifted to a center frequency at 2.54 GHz instead. Furthermore, the measured reflection coefficient is more broadband and has a better match. At around 2.73 GHz the simulation and measurement show a resonance. From the simulation it is seen that this is a dead resonance with a very low efficiency. The difference between the simulation and measurement is most likely due to the imprecise manufacturing of especially the CPW and by possible currents on the outside of the coaxial cable used to feed the antenna for measurements.

The simulated radiation pattern at 2.45 GHz can be seen in Fig. 3. The peak gain is 1.9 dBi and the radiation efficiency

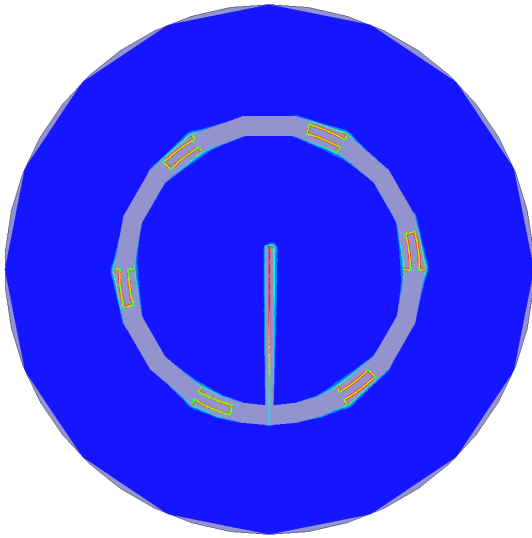


Fig. 4. Simulated complex magnitude of surface current distribution with an incident power of 1 mW. The linear color scale range from 0 A/m (blue) to 20 A/m (red).

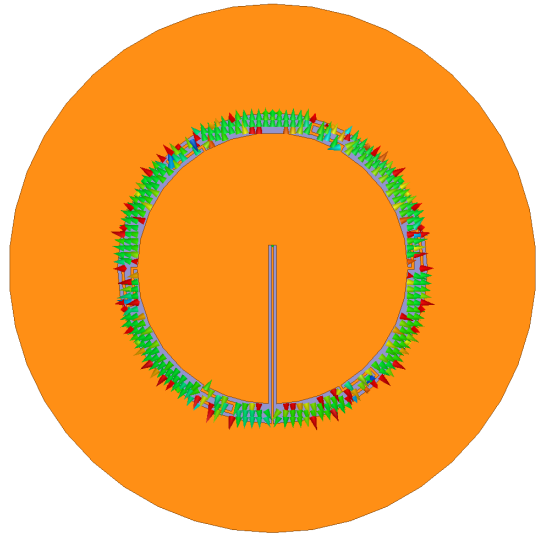


Fig. 5. Simulated electric field in the slot plotted with vectors with an incident power of 1 mW. The linear color scale range from 0 V/m (blue) to 500 V/m (red).

is 71.0 %. It is seen that the radiation pattern is not that of a small magnetic loop antenna. The difference is the null in the XY-plane. This is caused by the truncation of the copper plane. To make the exact complimentary of the electric loop, the plane should be infinite in extend. The antenna is almost completely θ -polarized with a peak gain for the θ -component and the ϕ -component of 1.9 dBi and -10.9 dBi, respectively. Furthermore, it is seen that the antenna is almost perfectly omnidirectional.

The simulated complex magnitude of the surface currents on the antenna can be seen in Fig. 4. It is seen that each of the inductors carry approximately the same current on them. It is also noted that the current on the CPW are low at the slot and high at the feed, which shows the impedance transformation from a high to a lower impedance. The simulated electric field in the slot is shown in Fig. 5. The field is plotted as vectors at the phase where it is at a maximum. As seen, the electric field is uniform in both magnitude and direction exactly like that of a small slot loop.

IV. CONCLUSION

A novel vertically polarized omnidirectional printed slot loop antenna has been successfully designed, simulated, fabricated and measured. The antenna is designed for the ISM band at 2.45 GHz. The polarization of the antenna and omnidirectional radiation pattern is made by loading the slot

with inductors to insure a uniform electric field in the slot. This makes the antenna behave like a small slot loop. Due to the polarization it is suitable for on-body applications. The antenna is well matched in the entire ISM band. The antenna is almost completely θ -polarized. The peak gain is 1.9 dBi and the efficiency 71.0 %. If needed, it is possible to further reduce the size of the antenna, e.g., for smaller applications. One way to do this is to reduce the size of the loop, while the inductance of the shunt inductors are increased.

REFERENCES

- [1] S. Gabriel, R. W. Lau, and C. Gabriel, "The dielectric properties of biological tissues: III. Parametric models for the dielectric spectrum of tissues." *Physics in medicine and biology*, vol. 41, pp. 2271–2293, 1996.
- [2] J. Ryckaert, P. De Doncker, R. Meys, A. de Le Hoye, and S. Donnay, "Channel model for wireless communication around human body." *Electronics Letters*, vol. 40, no. 9, pp. 543–544, 2004.
- [3] P. S. Hall, Y. Hao, Y. I. Nechayev, A. Alomainy, C. C. Constantinou, C. G. Parini, M. R. Kamarudin, T. Salim, D. Hee, R. F. Dubrovka, A. Owadally, W. Song, A. A. Serra, P. Nepa, M. Gallo, and M. Bozzetti, "Antennas and Propagation for On-Body Communication Systems." *IEEE Antennas Propag. Mag.*, vol. 49, no. 3, pp. 41–58, 2007.
- [4] K. Wei, Z. Zhang, and Z. Feng, "Design of a Wideband Horizontally Polarized Omnidirectional Printed Loop Antenna." *IEEE Antennas Wirel. Propag. Lett.*, vol. 11, pp. 49–52, 2012.
- [5] H. G. Booker, "Slot Aerials and Their Relation to Complementary Wire Aerials (Babinet's Principle)." *Journal of the Institution of Electrical Engineers*, vol. 93, no. 4, pp. 620–626, 1946.

